

FINAL PROJECT - CM224835

**APPLICATION OF SMALL BASELINE SUBSET (SBAS)-
INSAR TECHNIQUE TO STUDY SURFACE
DEFORMATION DUE TO THE GRINDULU FAULT
ACTIVITIES USING SENTINEL-1 DATA**

ANNISA RAHMAWATI TIMUR

NRP 03311942000009

Advisor

Ira Mutiara Anjasmara, S.T., M.Phil., Ph.D.

NIP 197812312002122001

Fitriani Agustin, S.T., M.Sc.

NIP 198008122002122002

Study Program Bachelor of Geomatics Engineering

Department of Geomatics Engineering

Faculty of Civil, Planning, and Geo Engineering

Institut Teknologi Sepuluh Nopember

Surabaya

2023

"This page was deliberately blanked."



FINAL PROJECT - CM224835

**APPLICATION OF SMALL BASELINE SUBSET (SBAS)-
INSAR TECHNIQUE TO STUDY SURFACE
DEFORMATION DUE TO THE GRINDULU FAULT
ACTIVITIES USING SENTINEL-1 DATA**

ANNISA RAHMAWATI TIMUR

NRP 03311942000009

Advisor

Ira Mutiara Anjasmara, S.T., M.Phil., Ph.D.

NIP 197812312002122001

Fitriani Agustin, S.T., M.Sc.

NIP 198008122002122002

Study Program Bachelor of Geomatics Engineering

Department of Geomatics Engineering

Faculty of Civil, Planning, and Geo Engineering

Institut Teknologi Sepuluh Nopember

Surabaya

2023

"This page was deliberately blanked."



TUGAS AKHIR - CM224835

**APLIKASI TEKNIK SMALL BASELINE SUBSET (SBAS)-
INSAR UNTUK MEMPELAJARI DEFORMASI PERMUKAAN
AKIBAT KEGIATAN SESAR GRINDULU MENGGUNAKAN
DATA SENTINEL-1**

ANNISA RAHMAWATI TIMUR

NRP 03311942000009

Dosen Pembimbing

Ira Mutiara Anjasmara, S.T., M.Phil., Ph.D.

NIP 197812312002122001

Fitriani Agustin, S.T., M.Sc.

NIP 198008122002122002

Program Studi S-1 Teknik Geomatika

Departemen Teknik Geomatika

Fakultas Teknik Sipil, Perencanaan, dan Kebumihan

Institut Teknologi Sepuluh Nopember

Surabaya

2023

"This page was deliberately blanked."

APPROVAL SHEET

APPLICATION OF SMALL BASELINE SUBSET (SBAS)-INSAR TECHNIQUE TO STUDY SURFACE DEFORMATION DUE TO THE GRINDULU FAULT ACTIVITIES USING SENTINEL-1 DATA

FINAL PROJECT

Submitted to fulfill one of the requirements
To obtain a bachelor's degree in engineering at
The undergraduate study program of Geomatics Engineering
Department of Geomatics Engineering
Faculty of Civil, Planning, and Geo-Engineering
Institut Teknologi Sepuluh Nopember

By: ANNISA RAHMAWATI TIMUR

NRP. 03311942000009

Approved by Final Project Examiner Team:

1. Ira Mutiara Anjasmara, S.T., M.Phil., Ph.D.
NIP. 19781231 200212 2 001

Advisor

2. Fitriani Agustin, S.T., M.Sc
NIP. 19800812 200212 2 002

Co-Advisor

3. Dr. Eko Yuli Handoko, S.T., M.T
NIP. 19740727 200003 1 001

Examiner

4. Akbar Kurniawan, S.T, MT
NIP. 19860518 201212 1 002

Examiner

5. Putra Maulida, ST, MT.,Ph.D.
NIP. 19910920 201903 1 015

Examiner



"This page was deliberately blanked."

LEMBAR PENGESAHAN

APLIKASI TEKNIK SMALL BASELINE SUBSET (SBAS)-INSAR UNTUK MEMPELAJARI DEFORMASI PERMUKAAN AKIBAT KEGIATAN SESAR GRINDULU MENGGUNAKAN DATA SENTINEL-1

TUGAS AKHIR

Diajukan untuk memenuhi salah satu syarat
memperoleh gelar Sarjana pada
Program Studi S-I Teknik Geomatika
Departemen Teknik Geomatika
Fakultas Teknik Sipil, Perencanaan, dan Kebumihan
Institut Teknologi Sepuluh Nopember

Oleh: ANNISA RAHMAWATI TIMUR

NRP. 03311942000009

Disetujui oleh Tim Penguji Tugas Akhir :

1. Ira Mutiara Anjasmara, S.T., M.Phil., Ph.D.
NIP. 19781231 200212 2 001

Pembimbing

2. Fitriani Agustin, S.T., M.Sc
NIP. 19800812 200212 2 002

Ko-Pembimbing

3. Dr. Eko Yuli Handoko, S.T., M.T
NIP. 19740727 200003 1 001

Penguji

4. Akbar Kurniawan, S.T, M.T
NIP. 19860518 201212 1 002

Penguji

5. Putra Maulida, ST, MT., Ph.D
NIP. 19910920 201903 1 015

Penguji



"This page was deliberately blanked."

STATEMENT OF ORIGINALITY

The undersigned below:

Name of student / NRP : Annisa Rahmawati Timur / 03311942000009
Department : Geomatics Engineering
Advisor/ NIP : 1. Ira Mutiara Anjasmara, S.T., M.Phil, Ph.D/
197812312002122001
2. Fitriani Agustin, S.T., M.Sc. / 199109202019031015

Hereby declare that the Final Project with the title of "APPLICATION OF SMALL BASELINE SUBSET (SBAS)-INSAR TECHNIQUE TO STUDY SURFACE DEFORMATION DUE TO THE GRINDULU FAULT ACTIVITIES USING SENTINEL-1 DATA" is the result of my own work, is original, and is written by following the rules of scientific writing.

If in the future there is a discrepancy with this statement, then I am willing to accept sanctions in accordance with the provisions that apply at Institut Teknologi Sepuluh Nopember.

Surabaya, 28 July, 2023

Acknowledged
Advisor



Ira Mutiara Anjasmara, S.T., M.Phil., Ph.D
NIP. 19781231 200212 2 001

Co-Advisor



Fitriani Agustin, S.T., M.Sc.
NRP. 19800812 200212 2 002

Student



Annisa Rahmawati Timur
NRP. 03311942000009

"This page was deliberately blanked."

PERNYATAAN ORISINALITAS

Yang bertanda tangan di bawah ini:

Nama mahasiswa/ NRP : Annisa Rahmawati Timur / 03311942000009
Program Studi : Teknik Geomatika
Dosen Pembimbing/ : 1. Ira Mutiara Anjasmara, S.T., M.Phil, Ph.D/
NIP 197812312002122001
2. Fitriani Agustin, S.T., M.Sc. / 199109202019031015

Dengan ini menyatakan bahwa Tugas Akhir dengan judul “APLIKASI TEKNIK SMALL BASELINE SUBSET (SBAS)-INSAR UNTUK MEMPELAJARI DEFORMASI PERMUKAAN AKIBAT KEGIATAN SESAR GRINDULU MENGGUNAKAN DATA SENTINEL-1” adalah hasil karya sendiri, bersifat orisinal, dan ditulis dengan mengikuti kaidah penulisan ilmiah.

Bilamana di kemudian hari ditemukan ketidaksesuaian dengan pernyataan ini, maka saya bersedia menerima sanksi sesuai dengan ketentuan yang berlaku di Institut Teknologi Sepuluh Nopember.

Surabaya, 28 Juli, 2023

Mengetahui,
Dosen Pembimbing

Dosen Pembimbing



Ira Mutiara Anjasmara, S.T., M.Phil., Ph.D
NIP. 19781231 200212 2 001



Fitriani Agustin, S.T., M.Sc.
NRP. 19800812 200212 2 002

Mahasiswa



Annisa Rahmawati Timur
NRP. 03311942000009

"This page was deliberately blanked."

ABSTRACT

APPLICATION OF SMALL BASELINE SUBSET (SBAS)-INSAR TECHNIQUE TO STUDY SURFACE DEFORMATION DUE TO THE GRINDULU FAULT ACTIVITIES USING SENTINEL-1 DATA

Student Name / NRP : Annisa Rahmawati Timur / 03311942000009
Department : Geomatics Engineering FTSPK - ITS
Advisor : Ira Mutiara Anjasmara, S.T., M.Phil., Ph.D.
Fitriani Agustin, S.T., M.Sc.

Abstract

Numerous variables contribute to the deformation; for instance, local thrust movements, human-made activities, and seismic activity along the Grindulu Fault. The Meteorological, Climatological, and Geophysical Agency of Indonesia (BMKG) reported seismic activities in Pacitan were delivered following November 7, 2019, earthquake, which could indicate the existence of the Grindulu Fault. The location of Grindulu Fault is in the Pacitan Regency on the Southern Coast of Java which directly faces the South Java Subduction zone. In this research, we identify fault activities through the detection around the Grindulu Fault to reduce the disaster risk in Pacitan Regency. Twenty-three ascending Sentinel-1B images and Small Baseline Subset InSAR technique were used to monitor ground deformation in Pacitan Regency between 2019 and 2021. SBAS-InSAR is one of the approaches for analysis techniques that can provide techniques continuous measurements of the ground deformation; it produces mean LOS velocity throughout the Line of Sight (LOS) around the Grindulu Fault segment. The processing was carried out using the GMTSAR software and compared the result using SBAS generated by open-source LiCSBAS of open-source SAR processing result showed deformation in the form of land subsidence in almost all of the Pacitan, with the mean velocity ranging from -2.1 to -43.1 mm/yr. The cause of deformation is the same thing, the existing Grindulu fault. The SBAS result confirmed with geological and geomorphological conditions such Triangular facets, braided rivers, and depression zone near Grindulu fault. Furthermore, the comparison results with the mean LOS velocity from LiCSBAS show that the area around Grindulu Fault also experiences land subsidence. Even though the RMSE value obtained is 13.7 mm/yr, it is demonstrating that the SBASInSAR velocity generated by GMTSAR processing not enough corresponds to the LiCSBAS.

Keywords: *Grindulu Fault, Ground Deformation, Small Baseline Subset (SBAS)-InSAR, Sentinel-1, Active Fault.*

"This page was deliberately blanked."

ABSTRAK

APLIKASI TEKNIK SMALL BASELINE SUBSET (SBAS)-INSAR UNTUK MEMPELAJARI DEFORMASI PERMUKAAN AKIBAT KEGIATAN SESAR GRINDULU MENGGUNAKAN DATA SENTINEL-1

Nama Mahasiswa / NRP : Annisa Rahmawati Timur / 03311942000009
Departemen : Departemen Teknik Geomatika FTSPK - ITS
Dosen Pembimbing : Ira Mutiara Anjasmara, S.T., M.Phil., Ph.D.
Fitriani Agustin, S.T., M.Sc.

Abstrak

Banyak variabel berkontribusi pada deformasi; misalnya, gerakan tektonik lokal, atau bahkan aktivitas manusia maupun seismik di sepanjang Sesar Grindulu. Badan Meteorologi, Klimatologi, dan Geofisika Indonesia (BMKG) melaporkan aktivitas seismik di Pacitan terdeteksi yakni berupa gempa bumi pada 7 November 2019, yang dapat menjadi indikasi keberadaan Sesar Grindulu. Letak Sesar Grindulu berada di Kabupaten Pacitan dekat dengan Pesisir Selatan Jawa dan berhadapan langsung dengan zona Subduksi Selatan Jawa. Pada penelitian dilakukan identifikasi aktivitas sesar melalui deformasi yang terjadi di sekitar Sesar Grindulu, sehingga dapat mengurangi risiko bencana di Kabupaten Pacitan. Dua puluh tiga citra ascending Sentinel-1B dan teknik Small Baseline Subset InSAR digunakan untuk memantau deformasi tanah di Kabupaten Pacitan antara tahun 2019 dan 2021. SBAS-InSAR adalah salah satu pendekatan untuk memberikan pengukuran deformasi tanah secara kontinu dalam bentuk rata-rata kecepatan deformasi disepanjang *Line of Sight* (LOS). Pemrosesan dilakukan dengan menggunakan perangkat lunak GMTSAR yang kemudian dibandingkan dengan menggunakan SBAS yang dihasilkan oleh perangkat lunak *open source*, LiCSBAS. Hasil pengolahan GMTSAR menunjukkan deformasi berupa penurunan muka tanah di hampir seluruh wilayah Pacitan, dengan kecepatan rata-rata berkisar antara $-2,1$ hingga $-43,1$ mm/tahun. Penyebab deformasi adalah hal yang sama, yaitu keberadaan sesar Grindulu. Hasil SBAS terkonfirmasi dengan kondisi geologi dan geomorfologi berupa triangular facets, bentuk aliran sungai, dan zona depresi di dekat sesar Grindulu. Selain itu, hasil perbandingan nilai rata-rata kecepatan LOS LiCSBAS menunjukkan bahwa di sekitar Sesar Grindulu juga mengalami penurunan muka tanah. Meskipun nilai RMSE yang diperoleh adalah 13,7 mm/tahun, hal ini menunjukkan bahwa nilai SBASInSAR yang dihasilkan oleh pengolahan GMTSAR belum cukup sesuai dengan hasil LiCSBAS.

Kata kunci: Sesar Grindulu, Deformasi, Small Baseline Subset (SBAS)-InSAR, Sentinel-1, Sesar Aktif.

"This page was deliberately blanked."

PREFACE

All the praise and gratitude to Almighty God for the abundance of grace so that the creation of a final project report entitled “**Application Of Small Baseline Subset (Sbas)-InSAR Technique To Study Surface Deformation Due To The Grindulu Fault Activities Using Sentinel-1 Data**” can be completed properly. This final project can be carried out well thanks to the support and cooperation of various parties involved. During the final project, many parties helped the author so that it could run well. Therefore, the author would like to express his deepest gratitude to the following:

1. For Sutarman, my father, and Eni Suryani, my mother, who are the author's parents, as well as Adilio Muharom, my beloved Brother siblings, who always provide prayers and support.
2. Ira Mutiara Anjasmara, S.T, M.Phil., Ph.D., as the first supervising lecturer, who always provides support, guidance, and assistance in completing this Final Project
3. Fitriani Agustin, S.T., M.Sc., as the second supervising lecturer, who always provides support, guidance, and assistance in completing this Final Project.
4. Danar Guruh Pratomo, S.T., M.T., Ph.D. as the Head of the ITS Geomatics Engineering Department.
5. All of my Geomatics engineering friends and to those parties that cannot be mentioned who have helped and facilitated the author during final project.

The author realizes that in this report there are still many shortcomings and therefore criticisms and suggestions are indispensable for improving this report. The author also apologizes if there was a mistake to all parties involved in writing this report. The author hopes that this report can provide the best possible benefit.

Surabaya, July 28th, 2023

Author

"This page was deliberately blanked."

TABLE OF CONTENTS

COVER PAGE.....	i
APPROVAL SHEET	vii
LEMBAR PENGESAHAN.....	ix
STATEMENT OF ORIGINALITY	xi
PERNYATAAN ORISINALITAS	xiii
ABSTRACT.....	xv
ABSTRAK.....	xvii
PREFACE.....	xviii
TABLE OF CONTENTS.....	xxi
LIST OF FIGURES	xxiii
LIST OF TABLES.....	xxv
LIST OF ABBREVIATIONS AND ACRONYMS	xxvii
LIST OF SYMBOLS	xxix
CHAPTER 1 INTRODUCTION.....	1
1.1 Background.....	1
1.2 Research Problems.....	2
1.3 Research Limitations	2
1.4 Research Objectives.....	2
1.5 Research Benefits	2
CHAPTER 2 LITERATURE REVIEW.....	3
2.1 Results of Previous Research.....	3
2.2 Faults.....	5
2.2.1 Fault Type.....	5
2.2.2 Active Fault	6
2.2.3 Grindulu Fault Characteristics.....	7
2.3 Geomorphology and Geology.....	8
2.3.1 Geomorphology in Pacitan.....	8
2.3.2 Geology in Pacitan	9
2.4 Earthquake	10
2.5 Deformation.....	11
2.5.1 Tectonic Deformation.....	11
2.5.2 Deformation Detection	12
2.6 Interferometric Synthetic Aperture Radar (InSAR).....	13

2.6.1	InSAR Data.....	14
2.7	Time Series InSAR (TS-InSAR).....	16
2.7.1	SBAS-InSAR Technique.....	17
2.7.2	SBAS-InSAR Algorithm.....	18
2.7.3	Coherence.....	19
2.7.4	Phase Unwrapping.....	19
2.8	SAR Image Processing Software.....	20
2.8.1	GMTSAR.....	20
2.8.2	LiCSBAS.....	20
2.9	Validation.....	21
CHAPTER 3	METHODOLOGY.....	23
3.1	The Method.....	23
3.2	Data and Tools.....	24
3.2.1	Data.....	24
3.2.2	Tools.....	26
3.3	Research Methodology.....	26
3.3.1	Research Stages.....	26
3.3.2	SAR Data Processing Stages Using GMTSAR.....	28
3.3.3	SAR Data Processing Stages Using LiCSBAS.....	31
CHAPTER 4	RESULT AND DISCUSSION.....	33
4.1	Small Baseline Interferometric SAR.....	33
4.1.1	Baseline Configuration.....	33
4.1.2	Interferometric Phase.....	34
4.1.3	Interferogram Coherence.....	36
4.1.4	Phase Unwrapping.....	37
4.1.5	LOS Displacement.....	38
4.2	Results and Analysis of SBAS InSAR.....	39
4.3	Validation of SBAS-InSAR between GMTSAR and LiCSBAS.....	44
4.4	Analysis of Geological and Geomorphology around the Grindulu Fault.....	46
CHAPTER 5	CONCLUSION AND SUGGESTION.....	51
5.1	Conclusion.....	51
5.2	Suggestion.....	51
REFERENCES.....		53
APPENDIX.....		57
AUTHOR'S BIOGRAPHY.....		75

LIST OF FIGURES

Figure 2.1 Types of faults and their focal mechanism diagrams	6
Figure 2.2 Interpretation of Grindulu fault	7
Figure 2.3 Interpreted Grindulu fault and Modification of the geological map in the study area based on the Pacitan Sheet Regional Geological Map at a scale of 1:250,000	10
Figure 2.4 (a) Observation geometry of a SLAR image, (b) DInSAR geometry for surface deformation detection, (c) geometry at baseline InSAR, and (d) geometry of deformation on the surface deformation	13
Figure 2.5 Sentinel-1 Product Mode	15
Figure 2.6 Illustration of baseline formation using the SBAS method.	18
Figure 3.1 Research Location	23
Figure 3.2 Research Flowchart	26
Figure 4.1 The Combination of 50 Interferogram Pairs base on Temporal and perpendicular baseline.	34
Figure 4.2 Interferogram Phase (a) and Filtered Phase (b).....	35
Figure 4.3 Coherence Image (a); Histogram of Coherence (b).....	36
Figure 4.4 Unwrapped Phase	37
Figure 4.5 LOS Displacement.....	38
Figure 4.6 Displacement Time-Series between April 2019 and February 2021.....	39
Figure 4.7 Distribution of 6 Sample Points	41
Figure 4.8 Graph LOS displacement.....	42
Figure 4.9 Result of SBAS InSAR using GMTSAR	44
Figure 4.10 Result of SBAS InSAR using LiCSBAS.....	44
Figure 4.11 Comparison between SBAS InSAR using GMTSAR and LiCSBAS.....	45
Figure 4.12 Seismicity Map in the research area	46
Figure 4.13 The results of the cross-sectional visualization bby detectinon value, (red line is Grindulu fault).....	47
Figure 4.14 Modification of the regional geomorphology and geological map in the study area based on the Pacitan Sheet Regional Geological Map at a scale of 1:250,000	48

"This page was deliberately blanked."

LIST OF TABLES

Table 2.1 Previous Research Related to The Research Location	3
Table 2.2 Previous Research Related to The INSAR Method	4
Table 2.3 Seismic Activities Around The Grindulu Fault.....	11
Table 3.1 Sentinel 1B Data.....	24
Table 4.1 LOS Displacement in point sample	43

"This page was deliberately blanked."

LIST OF ABBREVIATIONS AND ACRONYMS

ALOS	: Advanced Land Observing Satellite
BMKG	: Meteorological, Climatological, and Geophysical Agency
DEM	: Digital Elevation Model
DInSAR	: Differential Interferometry Synthetic Aperture Radar
DN	: Digital Number
EGM	: Earth Gravitational the Model
ERS	: European Remote Sensing
ESA	: European Space Agency
ESDM	: Ministry of Energy and Mineral Resource
GeoTIFF	: Geographic Tagged Image File Format
GMT	: Generic Mapping Tools
GMTSAR	: Generic Mapping Tools Synthetic Aperture Radar
GPS	: Global Positioning System
GNSS	: Global Navigation Satellite System
InSAR	: experiencesmetric Synthetic Aperture Radar
IW	: Interferometric Wide
KML	: Keyhole Markup Language
LiCSAR	: Looking into Continents from Space with Synthetic Aperture Radar
LOS	: Line of Sight
MSL	: Mean Sea Level
NASA	: National Aeronautics and Space Administration
NE	: Northeast
POE	: Precise Orbit Ephemeris
PS	: Persistent Scatters
RBI	: Indonesian Topographic Map
RMSE	: Root Mean Square Error
SAR	: Synthetic Aperture Radar

SBAS : Small Baseline Subset
SLC : Single Look Complex
SNAPHU : Statistical-Cost, Network Flow Algorithm for Phase Unwrapping
SRTM : Shuttle Radar Topography Mission
SW : Southwest
TS-InSAR : Time Series Interferometric Synthetic Aperture Radar
VV : Vertical vertical
WGS84 : World Geodetic System 1984

LIST OF SYMBOLS

B	: Look direction
$B \perp$: Perpendicular Baseline
d	: Value of displacement
N	: Number of SAR imagery datasets
n	: Lots of sample data
θ_{inc}	: Incident angle
$\delta\phi$: Phase difference between images
Δd	: Earth deformation value pointing to the satellite (LOS)
v	: Mean phase velocity between time adjacent acquisitions t
λ	: Radar wavelength
γ	: Coherence
α	: Off-nadir angle
σ	: Standard deviation
(x, r)	: Position azimuth and range in the image

"This page was deliberately blanked."

CHAPTER 1

INTRODUCTION

Chapter 1 contains an introduction to the research background, research problems, research limitations, research objectives and benefits of the research.

1.1 Background

Understanding the spatial and temporal variations of fault activities and behavior, especially the seismicity due to fault, is important for a better understanding in deformation and disaster risk assessment because it directly impacts the seismogenic potential of the fault (Champenois et al., 2012). In addition, deformation might occur gradually after an event that happened years and years ago because of fault activities. It can also occur suddenly, usually followed by fundamental physical changes because of earthquakes, and is evident in the magnitude and average movement velocity. Numerous variables contribute to the deformation; for instance, seismicity along the Grindulu Fault was detected following the November 7, 2019 earthquake. The Meteorological, Climatological, and Geophysical Agency of Indonesia (BMKG) reported a magnitude 3.1 earthquake with a depth of 10 kilometers with an on-land epicenter located at 8.170° South Latitude and 111.136° East Longitude (BMKG, 2023) that can indicate there is activity of the Grindulu fault. The existence of the Grindulu Fault was one of the biggest causes of the potential seismicity in Pacitan. Therefore, it is necessary to understand and monitor areas vulnerable to deformation and monitor tectonic activities to minimize risks in the future.

The Pacitan population is around 554,394 million people (BPS, 2020) and most of the Pacitan topography is a plateau close to a sloping mountain (Ichsandya et al., 2022). The increase in the number of buildings and tourism in the region by detecting rapid population growth. Considering the population and location of Pacitan, which the Grindulu Fault crosses, the disaster risk triggered by the vulnerability of the Pacitan region to potential seismic disasters must be reduced to a minimum. One of the efforts to reduce disaster risk is to study the Grindulu Fault activity. Better knowledge about the characteristics of the Grindulu Fault can be a reference for prevention and management programs for the impact of seismic disasters in the Pacitan area. In the context of disaster mitigation actions must consider all possible consequences to reduce all potential negative effects.

Monitoring the occurrence of deformation is one of the early mitigation strategies that can be used. The deformation characteristics can be quantified and further explored by looking at the pattern and results velocity of land deformation change around the Grindulu Fault. Geodetic techniques, such as topographic surveys, microgravity surveys, and GNSS surveys, can be used to monitor deformation (Abidin et al., 2009; Hu et al., 2019). These observations are especially concentrated in areas where localized deformation occurs within a short distance around the fault trace. However, the distribution of the deformation due to fault activities can also be elastically distributed across several kilometers. In order to complement microgravity measurement and ground-based data, therefore, it is required to use a different method, such as Remote Sensing. Method of Time-Series InSAR as one of remote sensing application, which has the potential to improve the spatial and temporal deformation measurements significantly (Hu et al., 2019; Lanari et al., 2007; Qiu et al., 2019). Therefore, as a first mitigation effort, this

study discovers and analyzes surface deformation phenomena around the Grindulu Fault Activities using Time-series InSAR especially SBAS-InSAR and sentinel-1 data from April 2019 to February 2021. The GMT-SAR software is used to process the SAR image and investigate deformation using Small Baseline Subset InSAR technique.

1.2 Research Problems

The problems of the research are as follows.

1. What is the mean velocity displacement that occurs throughout the Line of Sight (LOS) and LOS cumulative displacement time series in the area around the segment of the Grindulu Fault based on the SBAS-InSAR method?
2. How to analyze the results of the SBAS-InSAR visualization based on geological conditions and earthquake data records to better understand Grindulu Fault activities in Pacitan?

1.3 Research Limitations

The research limitations of the research are as follows.

1. The study area only considers around Grindulu Fault in Pacitan City which is located at coordinates $07^{\circ}55'00'' - 08^{\circ}17'00''$ South Latitude and $110^{\circ}55'00'' - 111^{\circ}25'00''$ East Longitude.
2. The data used in this research are Sentinel-1B imagery using Ascending type data acquisition between April 2019 and February 2021. The supporting data used for consideration of the analysis of the research results are the geological data around the Grindulu Fault, and earthquake seismicity data which are in accordance with the scope of the research area.
3. The method applied in this study is the Small Baseline Interferometry SAR (SBAS-InSAR).
4. The final results of the study are presented in the map of mean LOS velocity displacement and LOS cumulative displacement time series.

1.4 Research Objectives

The objectives of the research are as follows.

1. Determine the mean velocity and cumulative displacement of ground deformation that occurs throughout the Line of Sight (LOS) in the area around the segment of the Grindulu Fault based on the SBAS-InSAR method.
2. Analyze the results of the SBAS-InSAR visualization based on geological conditions and earthquake data records around the Grindulu Fault, East Java area.

1.5 Research Benefits

The benefit that can be taken from this research is that it can provide information about the Line of Sight (LOS) ground deformation velocity that occurred in the area around the Grindulu Fault activity between April 2019 and February 2021 based on SBAS-InSAR processing. The information can then be used as study material and consideration in the stages of disaster mitigation, especially earthquakes or another related research.

CHAPTER 2

LITERATURE REVIEW

In this chapter, certain fundamental concepts about fault tectonic activity, ground deformation, and InSAR and radar interferometric phase components are explained and discussed in more detail.

2.1 Results of Previous Research

The following is a summary of previous research related to research location which is described in Table 2.1 as follows:

Table 2.1 Previous Research Related to The Research Location

Aspect	Research 1	Research 2
Author	(Cholifah et al., 2020)	(Yusvinda et al., 2021)
Title	Identification of the Grindulu Fault in Pacitan, East Java using Magnetic Method.	Structure Interpretation Using Gravity Spectral Analysis and Derivative Method in Grindulu Fault, Pacitan.
Objective	This research is expected to identify the Grindulu fault zone, which is potentially vulnerable to geohazards using magnetic method.	To study the structure interpretation of the Grindulu Fault using gravity data by performing spectrum analysis and derivative methods.
Data	104-point dataset from measurements of two magnetometers in Pacitan, covering the area Gunungsari and Arjosari	Gravity Data Model GGMPlus reconstructed with satellite data and EGM2008
Time	2020	-
Software	Surfer 11	ETOPO 1, GMT software
Method	Magnetic method, Magnetic anomaly contour plot using Surfer 11, then separation resulting from the magnetic anomaly is processed by a reduction to pole transformation.	Spectrum analysis and derived methods
Result	<ul style="list-style-type: none"> • Magnetic method has been successfully used to delineate the Grindulu faulting zone, a geological sub-surface structure beneath the Pacitan city in the southern part of East Java, which is potentially vulnerable to seismic hazards. • The Grindulu is a normal fault featured by minor faults coming across or parallel with it, increasing the complexity of the tectonic setting in the region of interest. 	<ul style="list-style-type: none"> • Results of spectrum analysis conclude that the depth of the anomaly source from the Grindulu Fault is estimated to be at the upper limit of 160 meters and the lower limit up to 2897 meters. Analysis of the Grindulu fault interpretation is segmented into at least 7 parts. Those segmentations have different types of faults. GRF 1, GRF3, GRF4, and GRF6 are interpreted as reverse fault, while GRF2, GRF5, and GRF7 are interpreted as normal fault

From Table 2.1 some previous studies still use gravity and another method to detect the fault zone area. Several areas in East Java, where the implementation of detection in fault zone areas using InSAR is relatively rare, especially in the Grindulu Fault Zone in Pacitan. Within five years, several studies have focused on the Grindulu Fault research area using various methods Yusvinda et al. (2021) and Cholifah et al. (2020). While the use of the InSAR method to detect fault or deformation has already carried out by several researchers in other cities that are passed by the fault zone as show in Table 2.2

Table 2.2 Previous Research Related to The INSAR Method

Aspect	Research 1	Research 2	Research 3
Author	Dewanto, B. G., Setiawan. M. G, Nusantara., C.H. (2020)	Lanari, R., Casu, F., Manzo, M., & Lundgren, P. (2007).	Qiu, J., Liu, L., Wang, C., & Wang, Y. (2019).
Title	Opak Fault Deformation Monitoring Using Sentinel-1 InSAR Data From 2016-2019 In Yogyakarta Indonesia	Application of the SBAS-DInSAR technique to fault creep:A case study of the Hayward fault, California	Present-day tectonic activity along the central section of the Altyn Tagh fault derived from time series InSAR
Objective	to determine the deformation that is currently happening around the Opak Fault	Present a quantitative assessment of the DInSAR referred to as Small Baseline Subset (SBAS) to study fault creep phenomena	To obtain the present-day crust deformation rate field for the central section of the Altyn Tagh fault and inverted for the fault slip rate and the locking depth.
Data	<ul style="list-style-type: none"> • Sentinel 1 SAR from LiCSAR 	<ul style="list-style-type: none"> •45 SAR ascending images by the ERS satellites, • SRTM DEM •GPS data 2006-2010 	<ul style="list-style-type: none"> •14 HH polarimetric SAR images from ALOS PALSAR. •ALOS World 3D 30m (AW3D30) DEM
Time	2016 to 2019	mid-1992 up to the end of 2000	February 2007 until January 2010
Software	LiCBAS	GAMMA software, Hector, GAMIT/GLOBK10.6.	Envi SAR scape 5.4 (evaluation version)
Method	SBAS-InSAR technique	SBAS-DInSAR technique to generate the interferograms, low-pass, and high-pass filtering implemented spatial and temporal domain.	SBAS InSAR method with Atmospheric Correction using Temporal-spatial filtering method based on InSAR data using a small baseline approach.
Result	<ul style="list-style-type: none"> • The deformation occurring in the western area of Opak Fault movement (~30 mm/yr). However, -84 mm/yr to 15 mm/yr are the deformation range detected around Opak Fault with the standard deviation of 0.1 mm/yr. 	<ul style="list-style-type: none"> • the comparison between the DInSAR and the LOS-projected alignment array deformation measurements relevant to the sixteen sites. For example in Gilbert site Std between DInSAR and LOS projected alignment array is 4.8 mm and 4.7 mm. • The Std of the differences between the DInSAR and the in-situ measurements is 2 mm. The estimated mean deformation rates have an accuracy better than 1 mm/year. 	<ul style="list-style-type: none"> • The LOS rate of the central section ATF can effectively improve the quality of rate field. • The inversion results for the strike-slip rate at three selected cross-section locations perpendicular to the Altyn Tagh fault were 6.1 mm/a, 5.3 mm/a and 7.9 mm/a from west to east; the corresponding locking depths were 9.5 km, 6.8 km and 12.3 km from west to east. • The location and trend of the fault obtained by inversion coincide with the Xorkol seismic belt.

To determine the average value of Line of Sight (LOS) surface deformation velocity around the Grindulu Fault in Southeast Java, this research will use the InSAR method, similar to those used in the previous research. In contrast to the research conducted by (Qiu et al., 2019) this research utilizes ESA-provided open-source data of Sentinel 1B. Sentinel-1B satellite image data set of images with type Single Look Complex level 1, ascending direction and VV polarization from April 2019 to February 2021. In addition, this research differs from (Lanari et al., 2007) by utilizing the SBAS-InSAR approach with GMTSAR Software, which is appropriate for application in non-urban areas, like the region surrounding the Grindulu Fault in Pacitan. The use of SBAS-InSAR can also show deformation temporally due to tectonic activities as in the study of Ayani et al., (2021); Syahputri et al., (2023) and Yulita et al., (2018). The number of images in the last three years from the availability of sentinel 1B data with VV polarization is felt able to show early detection of surface deformation as in the study of Hu et al., (2019) and Yulita et al., (2018) . It is hoped that this research will contribute to the provision of new information regarding the detection of surface deformation around the Grindulu Fault in East Java so that it can serve as a resource for future geodynamics research developments and as a resource for the community and related agencies.

2.2 Faults

According to Noor (2009), Faults are areas on the Earth's surface where rock or the Earth's crust breaks or shifts due to tectonic stress. Faults are formed due to forces acting on the Earth's crust, such as the forces of attraction, pressure, or friction between tectonic plates. Therefore, a Fault is a condition where there is movement or shift of rocks due to geology in faults that can occur slowly over millions of years or suddenly over a short period of time, producing earthquakes. The fault itself then divides the area into two blocks, namely the hanging wall and the foot wall. The hanging wall is a plane that is above the fault, while the foot wall is a plane that is below the fault. The footwall is in a more stable position and tends to experience less significant movement relative to the other rock blocks in the vicinity. The hanging wall tends to experience more active movement and has the potential to shift or move close to the footwall.

2.2.1 Fault Type

The fault's movement can be relatively down, relatively up, or relatively flat against other blocks. The sudden movement of a fault or fault can cause an earthquake. Faults are areas of fractures or fracture zones in rocks that have undergone a shift. Faults can be divided into several types depending on the relative direction of the shift. The following are the Types of faults and their focal mechanism (Udías et al., 2014). Some of the terms about fault explained in the book of girty where fault analysis includes strike is the direction of the intersection of the fault plane with the horizontal plane measured from the north, and the fault slope (dip) is the angle formed between the fault line and the horizontal plane. The fault plane with the horizontal plane is measured perpendicular to the strike, the net slip is the relative displacement of the point on the fault plane, and the rake is the angle formed by the net slip with the strike on the fault plane.

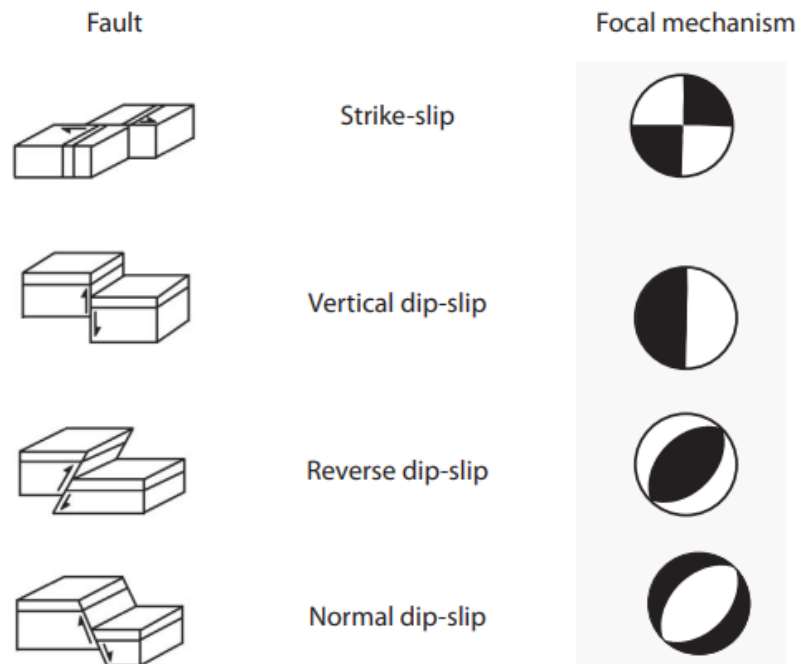


Figure 2.1 Types of faults and their focal mechanism diagrams (Udias et al., 2014)

Analysis of the fault depends on the classification of faults. Faults are categorized into strike-slip faults, where the motion is horizontal and parallel to the strike, and dip-slip faults, where the motion is on a vertical plane in cross-section (see Figure 2.1). Strike-slip faults are classified as right-lateral or left-lateral based on the direction of movement of one side of the fault as seen from the other side. Dip-slip faults are classified as normal faults, in which the hanging wall slides downward concerning the footwall, and reverse faults, in which the hanging wall moves upward concerning the footwall. Normal faults are also known as gravity faults since their motion is caused by a gravity-driven process. In the Figure 2.1 fault mechanism of Thrust faults are reverse faults with a slight dip angle. A horizontal and vertical motion combination causes oblique faults. Horizontal tension causes normal faults, whereas horizontal pressure causes reverse faults. Normal Faults form due to the highest compressive force in the vertical direction, which causes one of the rock planes to slide downward and follow the fault plane (Udías et al., 2014).

2.2.2 Active Fault

According to Girty, (2009) faults are formed at the surface where the Earth's material has lost cohesion due to the significant stresses, resulting in the compression of two blocks on opposite sides of the fault surface. If the fault is active and under pressure, rock vibration will occur as a result. An active fault is one of the displacement events that have accumulated throughout geological time, such as the manifestation of stress on fault blocks and the dynamics of the Earth's mantle so that the potential for surface deformation to occur soon. The accumulation of fault activity can show various forms of movement or changes that are regional and longitudinal to form a lineament, such as creeping fault activity to several places, continuous fault movement and faults that dart by storing enormous energy.

Before 1950, most geologists did not distinguish between inactive faults and those with a potential for renewed displacements and associated earthquake activity. However, this is a critical part of human planning and design. Scientist listed over 30 definitions for “active” or “capable” faults of which only three were made before 1950. No definition for active faults is universally accepted, although two elements are present in most definitions: (1) the potential or probability of future displacements in the present tectonic setting and (2) the time of most recent displacement (e.g., historical, Holocene, Quaternary, or “in the present seismotectonic regime”). The first element, potential, is critical to all assessments for larger earthquakes; the second, recency, relates indirectly to the rate of activity, which provides a more quantitative measure of the degree of fault activity. Fault activity can also be classified by fault slip rate. The general relationship between three factors of active fault: (1) the time since the last event or recurrence interval, (2) the surface wave magnitude, and (3) fault slip rate. So that it can be concluded that active faults are types of tectonic faults where there is significant relative movement on a geological scale at present or geologically recently. Active faults often experience earthquake activity associated with rock movement along them.

2.2.3 Grindulu Fault Characteristics

According to previous research and compared with research on the Cimandiri Fault (Supendi et al., 2018) and the Opak Fault (Dewanto et al., 2020), research on the Grindulu Fault (Cholifah et al., 2020) has not been widely carried out. The Grindulu Fault is most likely in a position in the coordinate range of 111.0° – 111.3° East Longitude and 8.1°– 8.2° South Latitude with orientation along the NE-SW line, which can be seen in Figure 2.2 The northeastern area of the study correlates with the northern region of Pacitan. It is thought to intersect the main line (red line in the figure) of the Grindulu Fault at the Grindulu River crossing. The southwest area is correlated with the southern region of Pacitan, which is heavily influenced by the southern mountain arc of Java Island.

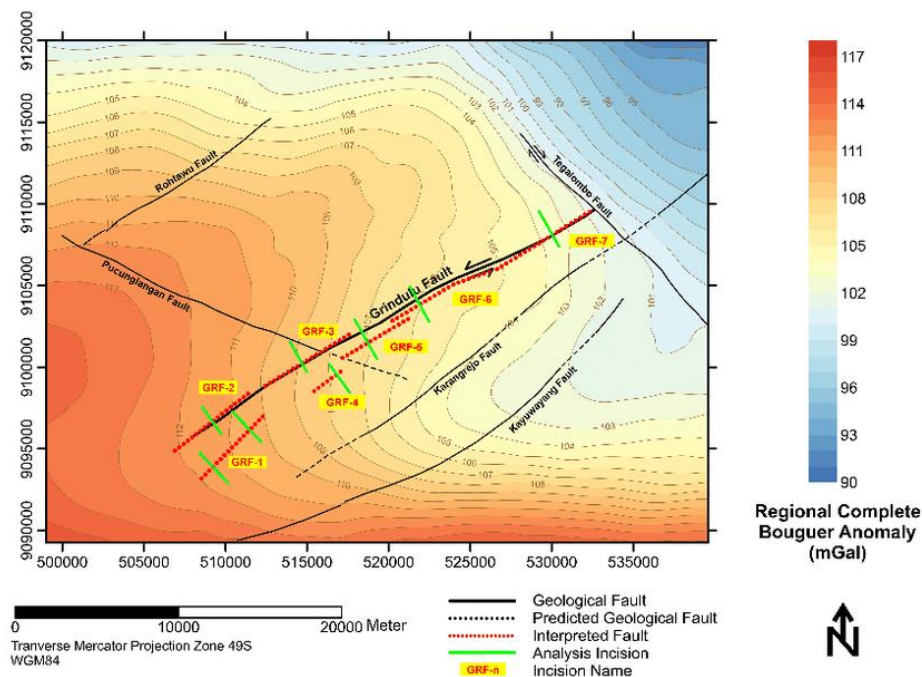


Figure 2.2 Interpretation of Grindulu fault (Yusvinda et al., 2021)

Several researchers have carried out research on the Grindulu Fault using geophysical methods such as derivative analysis method, shear wave estimation using the microtremor method (Caesardi, 2018), and Gravity Anomaly method (Parera et al., 2015). The Grindulu Fault has an orientation from northeast to southwest with information from the reactivation of old faults in bedrock (Gultaf, 2014). Based on Yusvinda (see Figure 2.2), there are 7 Grindulu Fault Segmentations, shown are the dashed red line. The seven fault segmentations show that those segmentations have different types of faults. GRF 1, GRF3, GRF4, and GRF6 are interpreted as reverse faults, while GRF2, GRF5, and GRF7 are interpreted as normal fault (Yusvinda et al., 2021).

2.3 Geomorphology and Geology

The word Geomorphology comes from the Greek language, which consists of “geo” which means earth, “morpho” means form, and “logos” means science. So, geomorphology is the study of the earth's surface's shape and its formation process. In addition to studying the shape or landscape, the process of its formation, but also studying the processes that influence it and its relation to its environment in space and time (Hidartan and Handayan, 1994). Geology has a broader object of study than geomorphology, because it includes the study of the entire earth's crust, while geomorphology is limited to the study of the surface of the earth's crust. Therefore, geomorphology is considered a branch of geology and later in its development, it becomes a separate science, apart from geology. Structural geology and dynamic geology are branches of geology that are very helpful in studying geomorphology. Dynamic geology helps to explain the evolution of the Earth's surface, while structural geology helps explain the types of landscape forms. Many landscape forms are reflected by their geological structure. Therefore, to study geomorphology, knowledge of these sciences is needed.

2.3.1 Geomorphology in Pacitan

Geomorphologists study the forms of the landscape they see, find out why a landscape occurs and find out the history and development of a landscape, as well as predict changes that may occur. The discussion of geomorphology is targeted based on its fundamental principles which are influenced by three factors namely structure, process and stadia. Structure studies the shape of an area's landscape based on geological structure, rock properties, whether there are layers, faults, friability, porosity, and permeability of the rocks to one another. Meanwhile, according to some experts, the geomorphological process means the energy that works on the surface of the earth that comes from outside the earth (exogenous forces) and not from within the earth (endogenous forces). The stage/level of the landscape is stated to find out how far the level of damage has occurred and at what stage/stadia is the current condition of the landscape. To express the level (geomorphic wheel) the terms: (1) Young, (2) Adult and (3) Old (Noor, 2014).

An example of Geomorphology in the surrounding area of a fault is the presence of Triangular facets, which are a result of structural geological processes. The area of Triangular facets shows the presence of water flows on a sloping surface that takes the shape of a triangle (Wallance et al., 1986). The occurrence of such a flow structure is caused by the initial formation of a sloped plane, wherein a shear line grows on the surface of said sloped plane due

to fault processes. The channel formed due to the fault serves as a conduit for water flow. The flow of water triggers erosion, resulting in the formation of a stream that eventually exhibits a triangular morphology. The Active Tectonics book also explains if there are indications of fluvial anomalies, such as the development of meanders or braided patterns, the local widening or narrowing of channels, pond anomalies, swamps or alluvial fill, changes in the width of embankments or intermittent embankments, and any strange curves or bends, which could be an indication of active tectonics. Because different types of alluvial channels react differently to active tectonics, it is impossible to predict channel patterns and changes in a consistent way. Instead, the alluvial channel's characteristics should be studied first so that possible responses can be evaluated. Based on the type of sediment load, alluvial channels can be categorized into three easy groups: bed load, mixed load, and suspension load. Braided channels are formed when a lot of sediment is deposited or when a lot of bed load is moved on steep slopes. So, a braided channel can either be stable or not stable. The pattern is like the unstable braided channel that forms in a valley when overbank flow splits a river into more than one channel.

2.3.2 Geology in Pacitan

Based on the geological formation, Pacitan City is in the Alluvium Formation (Qa), dominated by sedimentary layers. The thickest sediment layer is in the Alluvium Formation (Qa), with a thickness of 94.37 m, and the thinnest sediment layer is in the Jaten Formation (Tmj), with a thickness of 2.59 m. Sediment layers with a thickness of more than 50 m are in the Pacitan City area, Pacitan Bay, and the Grindulu River (Caesardi, 2018). The soft sediment layer will increase the ground shaking and cause more damage than the hard soil area. Earthquake damage is more severe in soft soil areas than in hard soil areas. This event is known as the amplification factor. This amplification factor is higher in the low S-wave velocity area (Rusydy et al., 2020).

Pacitan Regency is composed of 13 rock formations with four types based on the formation process: surface sedimentary rock, sedimentary rock, and volcanic rock (Samodra et al., 1992). The formations that makeup Pacitan Regency can be seen in Figure 2.3 which can be described as follows (Samodra et al., 1992) :

- Alluvium: Coral, gravel, sand, silt, clay, and silt
- Kalipucang Formation: Conglomerates and clays
- Wonosari Formation: Reef and layered limestone, flake and sandy limestone, and marl
- Oyo Formation: Limestone sandstone, tuffaceous sandstone, siltstone, tuffaceous limestone, sandy marl, and tuffaceous marl
- Nampol Formation: Tuffaceous sandstone, siltstone, tuffaceous limestone, claystone, and lignite, interspersed with conglomerate and breccia
- Wuni Formation: Volcanic breccia, tuffaceous sandstone, intervening sandstone, and siltstone, interspersed with lignite and limestone, locally containing irritable wood
- Jaten Formation: Conglomerate, conglomerate sandstone, tuffaceous sandstone, mudstone, siltstone, lignite, carbon shale, and tuff, local sulfur
- Campurdarat Formation: Crystal limestone and tuffaceous clay inserts
- Semilir Formations: Tuff, pumice breccia, tuffaceous sandstone, and claystone
- Arjosari Formation: Sandstone, siltstone, limestone, claystone, sandy marl, sandstone

pumice, interspersed with volcanic breccia, lava, and tuff

- Watupatok Formation: Lava, sandstone inserts, claystone, and chert
- Mandalika Formation: Alternations of volcanic breccia, lava, and tuff, interspersed with tuffaceous sandstone, siltstone, and claystone.

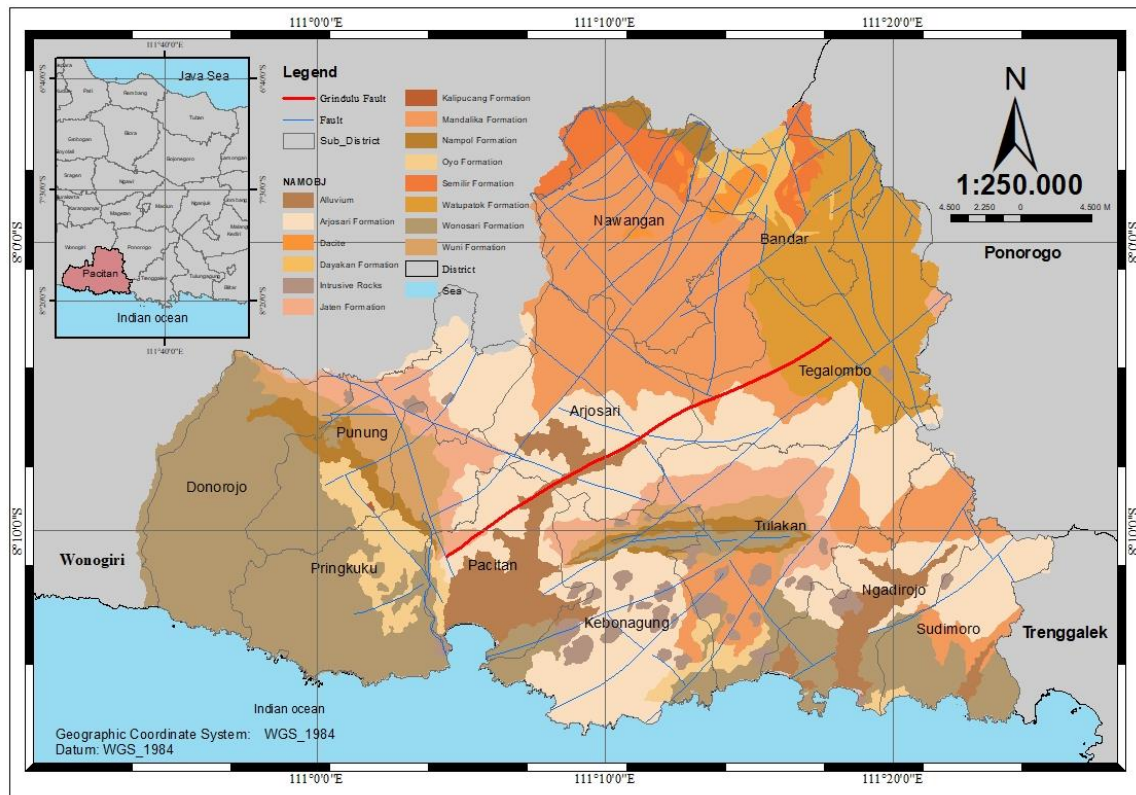


Figure 2.3 Interpreted Grindulu fault and Modification of the geological map in the study area based on the Pacitan Sheet Regional Geological Map at a scale of 1:250,000 (Yusvinda et al., 2021 and ESDM, 2023)

2.4 Earthquake

An earthquake is a movement of the masses of the earth that can be generated by interactions between the planet's tectonic plates, active faults, volcanic activity, or rock debris (ESDM, 2023). Seismicity data can be used as validation data that an area is a tectonically active area, where earthquake records and geomorphological evidence are used as reference material for mechanisms activated during seismic events. The Grindulu Fault and the Pucak Fault are active fault groups in Pacitan Regency (Caesardi, 2018). Those fault lines are estimated to stretch from Pacitan to Trenggalek. Historically, these two faults have caused earthquakes. Pacitan was rocked by a magnitude seven earthquake on October 20, 1859, an earthquake occurred with the epicenter located on the Grindulu Fault route (Hidayat et al., 2012). Apart from that, in November 2019, there was also an earthquake with a magnitude of 3.61 to the south of the grindulu fault Table 2.3 Seismic Activities Around The Grindulu Fault. The other earthquake event occurs in Pacitan, East Java, where the Grindulu Fault ruptured a magnitude of Mw 3.1 at a depth of 11 km on November 7, 2019. BMKG announced that the source mechanism of this earthquake is a strike-slip movement with a NE-SW direction, indicating the activity of the Grindulu Fault.

Table 2.3 Seismic Activities Around The Grindulu Fault
(BMKG, 2023)

Date/Time	Latitude (°)	Longitude (°)	Depth (km)	Magnitude (M)	Event ID
2023-02-06T20:24:24.157444Z	-7.783	111.395	11	3.61	bmg2023cpin
2022-09-22T08:49:08.200556Z	-7.81	111.633	13	3.45	bmg2022spag
2022-05-26T08:38:27.449049Z	-7.849	111.570	13	3.01	bmg2022kfpb
2022-04-16T21:59:20.130944Z	-8.11	111.595	10	2.63	bmg2022hlmi
2019-11-07T14:27:14.652265Z	-8.170	111.136	10	3.1	bmg2019vvmo
2019-07-10T14:25:41.620749Z	-8.277	111.485	10	2.94	bmg2019nkgd

Subduction zones have a wide variety of earthquakes with different mechanisms and depths. There are shallow (less than 70 km deep), intermediate (70–300 km deep), and deep (more than 300 km deep) focus earthquakes (Udías et al., 2014). Shallow earthquakes are one of the characteristics of earthquakes originating from active fault movement activities on land. Active faults are classified as a source of shallow crustal earthquakes. If an active fault runs along dense settlements, the number of casualties and material losses will be enormous.

2.5 Deformation

Deformation can be interpreted as an event of a change in shape or a shift in position, a change in position without a change in shape (translation), changes that affect the distance between objects (strain) and the dimensions of an object in absolute and relative terms in the scale of space and time (Hamad & Fadlil, 2021). Based on the geological structure, secondary rock structures are formed due to stress (such as compression or stretching) or deformation experienced by rocks after their original formation. Several secondary structures exist, such as faults, folds, domes, and basins (Zikri, 2018). The most significant positional displacements from the Earth's surface lie directly on the fault trail (assuming the fault occurs at the surface), and displacement generally decreases with increasing distance from the fault. Tectonic activity along the fault slope (dip-slip) is characterized by vertical changes, namely uplift or upward displacement of the Earth's surface concerning the geoid. In contrast, subsidence is the opposite (Zikri, 2018). In observing deformation using satellite imagery, deformation can be said to be uplifted if approaching the satellite and subsidence if away from the satellite. Monitoring of deformation areas is another example where SAR has been used successfully. SAR provides deformation values with a precision level of up to several mm, with high consistency both spatially and temporally (Hu et al., 2019).

2.5.1 Tectonic Deformation

According to the book of Active Tectonics: Impact on Society, displacement or offset at the foundation of a structure is one of the most direct risks (effects) of active faulting. Primary, secondary, and sympathetic movements are the three principal categories of fault movements associated with a faulting event. A primary rupture along the main fault responsible for the earthquake can cause maximal displacement. While secondary ruptures are those that take place

along branch faults and other subordinate faults. Locally accommodating deformation from the primary fault, these faults typically have smaller displacements. Therefore, secondary rupture displacements diminish with increasing fault distance. And for the last, strain release along the main fault or vibratory ground motion disturbs the stress state of another fault, causing displacement, sympathetic offsets occur. Three faults experienced sympathetic displacement during the 1968 Borrego Mountain earthquake: the Imperial, Superstition Hills, and San Andreas.

Tectonic deformation relates to the spatial or regional deformation that may or may not be linked to seismic events of significant magnitude. The observation of vertical displacement and tilting of shorelines during the 1964 Alaskan earthquake has provided significant evidence of tectonic deformation and its dramatic effects. These observations clearly demonstrate the movement of land in relation to sea level. A region of Montague Island demonstrated a peak vertical displacement of 37.8 feet, as observed from the comparison of pre-earthquake and post-earthquake shorelines in 1972. Geodetic measurements were utilized to document the Earth movements that occurred subsequent to the 1971 earthquake in San Fernando, California, which had a magnitude of 6.5. The measurements conducted by Savage et al. (1975) indicated that the mountains located to the northeast of the causative fault experienced vertical displacement of up to 2 m and horizontal displacement of up to 2 m.

2.5.2 Deformation Detection

Surface deformation detection can use Geodetic measurement, such as GPS survey method, usually in the form of deformation vector values in three dimensions with a precision level of up to several mm. Therefore, GPS has been used to observe the stability of structures that require high precision accuracies, such as monitoring the deformation of dams, bridges and towers. However, geodetic measurements such as GPS measurements take longer and require more human resources for data acquisition. Field conditions with high vegetation and hard-to-reach topography often become obstacles in GPS measurements. Therefore, it usually affects the results of measurements and takes a long time to cover a large area. While the gravity anomaly method and the magnetic method cannot determine the value of the magnitude of the movement of the deformation, the two methods are more often used to represent geological conditions, the type of fault and its depth based on the gravity anomaly. Therefore, the use of remote sensing technology such as InSAR can be used for deformation values.

The use of INSAR in deformation measurements is relatively more cost-effective because data acquisition using satellites does not require much human effort and is faster than geodetic measurements using GPS. InSAR can also monitor inaccessible areas due to challenging or unexplored topographical conditions. The availability of open-source InSAR data, such as Sentinel 1B from 2016, allows for temporal deformation monitoring over comprehensive area coverage. Compared with GPS deformation measurements, the results of InSAR processing are relevant. They can see deformations, such as Lanari's research showing a standard deviation between GPS and InSAR measurements of 1 mm/year. Likewise, other studies on opak faults showed a standard deviation of measurements using an InSAR compared to previous GPS studies showing a value of 0.1 mm/year.

consist of constituents and topographical displacements (components that must be extracted (Ferretti et al., 2007)). The measured phase difference between the two corresponding pixels is expressed by the phase interference equation on the interferogram 2.1 after proper co-registration of the two images (Ferretti et al., 2007) as follows:

$$\delta\phi = \delta\phi_{topo} + \delta\phi_{flat} + \delta\phi_{disp} + \delta\phi_{orbit} + \delta\phi_{atm} + \delta\phi_{noise} \quad 2.1$$

- $\delta\phi_{topo}$ is the topographic phase considering look direction, incident angle, and off-nadir angle.
- $\delta\phi_{flat}$ is the flat earth phase caused by geometry imaging, where q is the difference in altitude and $B\perp$ is the perpendicular baseline.
- $\delta\phi_{disp}$ is the differential displacement pattern(d) at position (x, r) between the acquisition times.
- $\delta\phi_{orbit}$ is a phase error due to inaccurate orbit parameters.
- $\delta\phi_{atm}$ is an atmospheric artifact due to atmospheric propagation delay.
- $\delta\phi_{noise}$ is the noise contribution due to differences in image look angle, temporal changes, and scatterer volume.

Multiplication of two SAR data consisting of the master (usually the data observed first or the time of the first observation) and slave (the second observation data) produces an interferogram (Hu et al., 2019). Interferogram stacking is done to compare the phase difference in each interferogram. The phase difference will produce fringes on the interferogram, called elevation displacement fringes. Two primary fringes on the interferogram are displacement fringes caused by surface topography shifts and topography fringes caused by topography (Rasimeng et al., 2020). One way to measure changes in the earth's surface is to perform a differential on the interferogram and eliminate the effects of topography and noise, known as SBAS InSAR (Burgmann et al., 2000).

2.6.1 InSAR Data

Sentinel-1 as the main product of ESA is one of the SAR satellites that operate with the polar orbit system with the C band ($\lambda = \sim 5.6$ cm). Sentinel 1 SAR data has been widely, consistently, and free of charge since the European Space Agency (ESA) launch and open data policy in 2014. Sentinel-1 SAR is divided into sections based on the results of satellite data recording or processing level. Accordance to the Sar Handbook, Level-1 SLC (Single Look Complex) products contain complex images that store phase information and amplitude. The SLC product is already georeferenced and shown in the geometry slant range, which is the natural geometry coordinates of radar observations along the path from the radar source to the object. Interferometric Wide (IW) is a standard type of ground surface observation belonging to Sentinel-1 at data level 1 of the Single Look Complex (SLC) category.

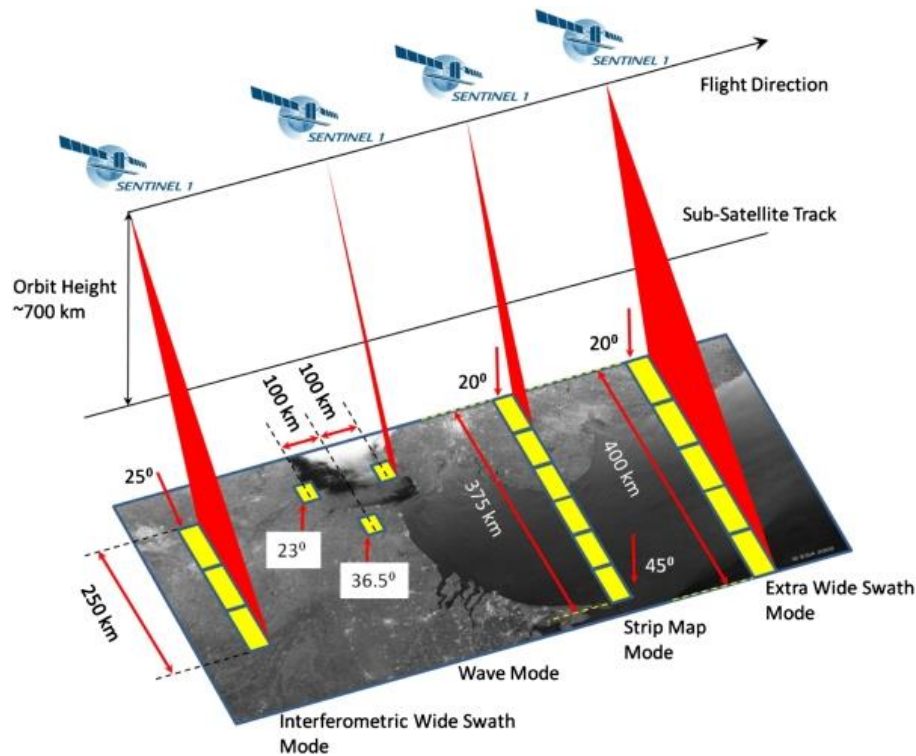


Figure 2.5 Sentinel-1 Product Mode (Gümgümcü et al., 2018).

Figure 2.5 shows that Sentinel-1 has four standard operating modes designed for interoperability with other systems:

- Strip Map mode, 80 km swath width and 5x5 m spatial resolution.
- Interferometric Wide Swath Mode, 250 km swath width, 5 x 20 m spatial resolution, is the mainland region's default mode.
- Extra-wide Swath Mode, 400 km swath width with a spatial resolution of 20 x 40 m;
- Wave Mode, low data rate and 5 x 20 m spatial resolution. Example image at 20 x 20 km at 100 km intervals along the orbit.

Polarization describes the orientation of the oscillation plane of a signal's propagation. The polarization of satellite signals relates to the orientation of radio waves utilized to deliver the signal. Polarization can be utilized to determine landscape structures and signal strength (Flores-Anderson et al., 2018). The majority of SAR sensors today are linearly polarized and transmit horizontally and/or vertically polarized wave patterns. Numerous SAR satellites are equipped with single-polarized sensors, which send one linear polarization and receive (e.g VV-polarization which is vertical transmit; vertical receive). VV polarization is vertical vertical polarization (VV) in which the axis of polarization is vertical, and the oscillation travels downward in the direction of gravity. This indicates that the antenna's transmitted wave goes in the direction of gravity.

2.7 Time Series InSAR (TS-InSAR)

The TS-InSAR method is extensively used to calculate and detect surface deformation resulting from fault activity (Hu et al., 2019) and tectonic activity (Qiu et al., 2019). Using tens or hundreds of SAR data acquired over a lengthy period of time; the TS-InSAR method was designed to overcome phase decorrelation and signal propagation delays in the atmosphere (weaknesses of the conventional DInSAR method) (long series). In general, the objective of developing the TS-InSAR approach is to detect pixel coherence based on the Signal-to-Noise Ratio (SNR) and to estimate and eliminate undesirable phase errors in the interferogram so that the mean LOS velocity may be determined (Berardino et al., 2002 ; Ferretti et al., 2007). According to Berardino, the Small Baseline Subset (SBAS) approach is one of the interferogram creation methodologies that can be used in the InSAR time series. In this study, threshold-determined interferogram pair correlations can be evaluated using the SBAS approach. The SBAS method creates many subsets of acquisition data; accordingly, they must be connected. In addition, the SBAS approach is described in subsection 2.7.1.

In general, the differences between InSAR, DInSAR, PS-InSAR, SBAS-InSAR are as follows following (Ferretti et al., 2007 ; Flores-Anderson et al., 2018; Berardino et al., 2002) :

1. InSAR

- InSAR (Interferometric Synthetic Aperture Radar) is a technique that use radar images to measure ground and structural movements by measuring the change in the phase of the signal between the two images obtained at the same area at different times.
- InSAR is mostly used for DEM (Digital Elevation Model) creation, to convert the phase difference between two images into relative heights. InSAR is also used to monitor subsidence/uplift or deformation.
- InSAR is a basic technique that uses radar interferometry to measure ground surface deformation.

2. DInSAR

- DInSAR (Differential InSAR) is the development of conventional InSAR which has eliminated topographical disturbances in InSAR.
- Using 2-4 SAR image data to observe the phase change between two images over a period.
- Considering changes in topography, DInSAR can provide more accurate estimates of ground surface deformation with sub-meter accuracy.
- The resulting interferogram is in the form of fringes. Every fringe on interferogram represents a quantitative change in the phase of the radar wave. The number and pattern of fringes can provide information about ground deformation.

3. PS-InSAR

- PS-INSAR is an InSAR method that has been developed to monitor smaller deformations using radar images that take over a longer time span and analyzes the interference patterns of permanent "scatterers" on the Earth's surface.
- Requires a lot of SAR image data (minimum 20-25 images)
- The final result is in the form of points which represent the mean LOS velocity with accuracy down to sub-millimeter.

- PS InSAR is more suitable for studies that focus on smaller, high-resolution areas such as urban areas.

4. SBAS-InSAR

- SBAS InSAR has better data capture for surface areas that experience small deformation over time, making it more reliable for applications involving smaller deformations in vegetation area.
- SBAS InSAR uses a more efficient because of automated processing approach to process interferometric data, while PS InSAR requires further analysis and more manual selection of measurement points (GCP).
- SBAS InSAR typically generates deformation maps using a lot of data, which allows monitoring of changes over a long period of time.
- SBAS-InSAR overcomes the limitations of the DInSAR technique caused by decorrelation and atmospheric noise (Flores-Anderson et al., 2018).

2.7.1 SBAS-InSAR Technique

The InSAR method is generally processed using several techniques, such as Differential Interferometry Synthetic Aperture Radar (DInSAR) and multi-temporal or time-series InSAR techniques consisting of Persistent Scatters (PS) InSAR and Small Baseline Subset (SBAS). The Differential Interferometry Synthetic Aperture Radar (DInSAR) technique is an interferometric observation that minimizes topographic effects on the measurement of surface deformation in the line of sight of the satellite to the target (scatterer) (Elias et al., 2018). While Time - series Synthetic Aperture Radar interferometry (InSAR) is one of the advanced types of techniques developed to overcome the limitations of the basic InSAR (DInSAR) method, such as temporal and geometric decorrelation and also to replace errors from atmospheric distortion, inaccurate earth surface models and uncertain satellite orbits. The primary objective of PS InSAR is to identify the motion of stationary objects, such as those seen in urban locations. SBAS InSAR is capable of detecting non-linear movement and makes use of a dispersed scatterer in conjunction with small spatial and short temporal baselines in order to achieve maximum coherence.

Small Baseline Subset (SBAS) is the formation of interferograms that can be applied to InSAR time series (Berardino et al., 2002). Multitemporal or time-series InSAR techniques usually involve processing multiple image acquisitions observed over a long period of Time. Setting the spatial and perpendicular baselines in SBAS, as shown in Figure 2.6, can minimize the phenomenon of spatial and temporal decorrelation. It can be seen if the interferogram network formation arrangement is based on a perpendicular baseline distribution of no more than 60 meters. The perpendicular baseline is a projection perpendicular to the oblique distance between satellites with two different orbits, see Figure 2.6. The technique can increase the sampling rate by using all the acquisitions in the smallest baseline subset and maintain the system's ability to provide spatially deformation maps.

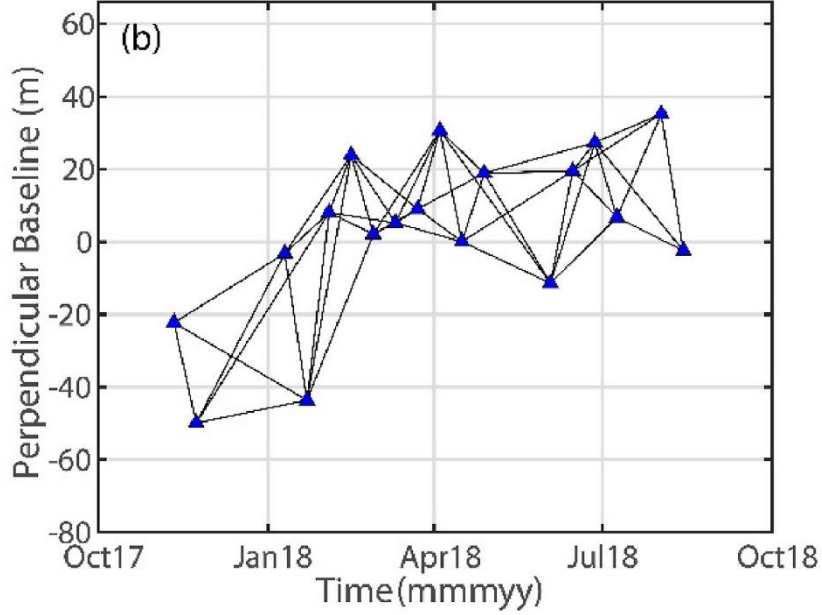


Figure 2.6 Illustration of baseline formation using the SBAS method.
(Li et al., 2022)

SBAS also serves to avoid phase errors propagating through the interferogram and storing an excessive number of interferograms in the data stack. SBAS can invert a small baseline interferogram stack containing the decomposition approach. The result is to exploit the spatial and temporal relationship of the redundant interferogram stack into multi-temporal interferogram processing. SBAS analysis, according to (Lanari et al., 2007) performs analyses based on stacked interferograms and multi-temporal data processing, from averaged data characterized by lower resolution. The monitoring is achieved by separating deformation contributions from residual topography and atmospheric artifacts of pixels on a sparse reliable grid and selected on spatial coherence analysis.

2.7.2 SBAS-InSAR Algorithm

The SBAS technique is a DInSAR approach allowing us to detect Earth's surface deformation and analyze its temporal. The SBAS technique is represented by the number of interferograms from the multi-master and slave that meet the requirements (M) and involves a set of $N + 1$ SAR acquisitions relative to the same area and obtained over the observation time range (t_0, \dots, t_N). It means the images are coregistered concerning a single one (referred to as master) in order to have a standard reference grid. The expression of the generic interferogram computed from the SAR acquisitions at times t_B and t_A is, according to the following (Berardino et al., 2002):

$$\begin{aligned} \delta\phi_j(x, r) &= \phi(t_B, x, r) - \phi(t_A, x, r) \\ &\approx \frac{4\pi}{\lambda} [d(t_B, x, r) - d(t_A, x, r)] \end{aligned} \quad 2.2$$

Where $\phi(t_B, x, r)$ and $\phi(t_A, x, r)$ represent as the phases of the two images involved in the interferogram generation and $d(t_B, x, r)$ and $d(t_A, x, r)$ are the radar line of sight projections of the cumulative deformation at times t_B and t_A . The expression 2.2 allows to

define a system of M equations by using a matrix formalism, as equation 2.3:

$$A\phi = \delta\phi \quad 2.3$$

Where A is an incidence-like matrix directly related to the set of interferograms generated from the available data, see (Berardino et al., 2002). The equation 2.3 can be replace the unknown $A\phi$ with the mean phase velocity between time adjacent acquisitions as in the equation 2.4

$$v = \left[v_1 = \frac{\phi(t_1, x, r)}{t_1 - t_0}, \dots, v_n = \frac{\phi(t_n, x, r) - \phi(t_{n-1}, x, r)}{t_n - t_{n-1}} \right] \quad 2.4$$

and, by substituting 2.4 in 2.3 the B as represent $M \times N$ matrix whose expression can be found in (Berardino et al., 2002).

$$Bv = \delta\phi \quad 2.5$$

According to the equation, the SBAS approach permits the prepared in advance is the script file "prep_SBAS.csh." has provide by GMTSAR. Before running script prep_sbass.csh, the prepared folder containing intf.tab, scene.tab, and unwrap.grd which is the result of the unwrapping phase, all three are stored in the /SBAS directory. Therefore, from prepare_sbass.csh the final results are in the form of mean LOS velocity and displacement time series.

2.7.3 Coherence

Coherence is an important factor affecting InSAR measurement. The wavelength of SAR data and terrain slope in the study area will affect the coherence of the interferogram. (Qiu, J., et al 2019). The value of coherence ranges from 0 which represents the interferogram phase which is formed only by noise to 1 which means there is no noise in the interferogram phase. These zero values can be an interferogram visualization of InSAR processing which has a black color, while coherence one is shown in white. However, for most practical applications of SAR interferometry, the approximated formula can be suitably exploited for coherence values higher than 0.2. (Ferretti et al., 2007). Therefore, a coherence of 0.1 was chosen between the master and slave images in order to show that both have a low noise level. As in Elias' research, SBAS processing with a minimum coherence threshold of 0.1 gives the large pixels that contain at least two small pixels from the original set. This coherence is good enough to provide accurate information in many areas in the rift of Corinth, Greece.

2.7.4 Phase Unwrapping

Information on the interferogram is still limited to $0 - 2\pi$, causing ambiguity problems. Therefore, the unwrapping phase is carried out to overcome this ambiguity. The contribution of the phase values due to topography and deformation contained in the interferogram can be known after processing through the phase unwrapping stage. The unwrapping phase is calculating changes in the phase value on the interferogram from one point to the next and integrating into a smoother phase. GMTSAR provides the SNAPHU (Statistical-Cost, Network Flow Algorithm for Phase Unwrapping) program based on the statistical cost network-flow

algorithm developed by (Zebker & Chen, 2002). The algorithm's solver routine is based on network optimization. By default, SNAPHU assumes that its input is a synthetic aperture radar (SAR) interferogram measuring surface topography. From the phase unwrapping process, the phase shift value in radian units will be obtained, which is then converted into the Line of Sight (LOS) Displacement value in metric units according to equation 2.5 (Yulfa et al., 2018).

$$\Delta r_{\text{disp}} = \frac{\lambda}{-4\pi} \delta\phi \quad 2.6$$

Description:

$\delta\phi$: Different Phase value.

λ : Radar Wavelength.

The problem statistics and resulting cost functions are based on the assumption that the actual unwrapped phase represents surface displacement rather than elevation. After this process is complete, an unwrapped interferogram pair is produced, showing the displacements along the LOS in metric units.

2.8 SAR Image Processing Software

2.8.1 GMTSAR

Generic Mapping Tools (GMT) is an open-source software with more than 70 specialized features for manipulating geographic and cartesian datasets, such as filtering, trend fitting, gridding, and projecting. The output of Gmt produces Encapsulated PostScript File (EPS) illustrations ranging from simple XY plots through contour maps to artificials to illuminated surfaces and 3-D perspective views. GMT can support more than 30 map projections and transformations and comes with supporting data such as coastlines, rivers, and political boundaries (Wessel et al., 2019). GMTSAR, on the other hand, is more of an InSAR processing system designed for users familiar with Generic Mapping Tools (GMT). The code is written in C, and the system has three main components of pre-processor, InSAR processor and post-processor. A pre-processor for each satellite data type (ERS-1/2, Envisat, ALOS-1, TerraSAR-X, Radarsat-2, Sentinel-1A/B, and ALOS-2) to convert the original format and orbital information into a standard format. InSAR processor to focus and align the image stack, map topography into phases, and form complex interferograms. A post-processor, based mainly on GMT, filters the interferograms and build interferometric products of phase, coherence, phase gradient, and line of sight in both radar and geographic coordinates. GMT displays all products as pdf files and KML images for Google Earth. A set of scripts has been developed for standard two-pass processing and geometric image alignment for arrays and time series (Sandwell et al., 2011).

2.8.2 LiCSBAS

LiCSBAS is an InSAR time series analysis and processing package using the COMET LiCSAR product written on the basis of Python and bash and developed by (Morishita et al., 2020). Interferograms derived from SLC (Single Look Complex) data are produced and processed automatically according to predetermined parameters and generally consist of 3 sub-swaths with Interferometric Wide (IW) covering an area of 250 km x 250 km. LiCSAR

performs the unwraps phase in the form of a 2-dimensional SNAPHU statistical cost approach. The area decorrelation in the interferogram is camouflaged where the filtered noise coherence estimates default to <0.5 in the unwrapping phase. The results of the interferogram and coherence that have gone through the process of wrapping (wrapped) and opening (unwrapped) have a pixel spacing of 100 m and the spacing is in GeoTIFF format. Perpendicular baseline and line-of-sight (LOS) vector metadata and quick view files and images published on the COMET-LiCS Sentinel-1 InSAR web portal are available for free download. LiCSAR products have been available primarily for the vicinity of the Himalayan Alpine Belt, Japan, the East African Rift, and global volcanoes, and coverage is still being expanded from November 2019 to date (Lazecký et al., 2020). In Indonesia, several studies have used LiCSAR products with LiCSBAS such as by (Hayati et al., 2022) in the Tanggulangin area, landslide earthquakes in Pacitan by (Ichsandya et al., 2022) and deformation spending around the Opak Fault area by (Dewanto et al., 2020)

The difference from InSAR processing using GMTSAR and LiCSBAS lies in that LiCBAS processing can only be used with LiCSAR imagery data collected at certain time intervals from the provider of the COMET LiCSAR website. The limitation of data availability and coverage is a key factor in InSAR processing using LiCSBAS. In addition, a fast internet connection is needed in processing data on LiCSBAS. This can be a problem for users who have a slow or unstable internet connection. Therefore, InSAR processing using GMTSAR as an open-source software allows users to access and modify the InSAR processing algorithm.

2.9 Validation

SBAS-InSAR processing produces a 1-dimensional deformation value that leads to the satellite or LOS. The final results of SBAS processing can be interpreted with deformation maps of the mean LOS velocity and cumulative time-series displacement. The result can be validated by comparing the surface deformation results from data processing using SBAS-InSAR at GMTSAR with the surface deformation values obtained from InSAR processing using LiCBAS. The results of the two processes will analyze the distribution result of surface deformation to calculate based on the RSME. In addition to validation, the interpretation of the SBAS-InSAR results also overlays with the geology formation in the research area, which is a clear indicator of the geomorphological processes involved, as well as historical earthquake records showing that there was tectonic movement.

The result from the data will be analyzed to better understand the situation represented by the data and inferring possible new results from certain phenomena. Descriptive statistics provide more concise, neat, and easy-to-understand information. This method usually provides information in the form of tables, charts, and graphs to make it easier and faster for readers to understand. At the same time, the statistical test using the Root Mean Square Error (RMSE) helps in determining the distribution of data errors (Chai & Draxler, 2014). RMSE states how well the performance of a calculation model. The smaller the RMSE value, the better the performance of the model (Willmott & Matsuura, 2005). In this study, RMSE is used to measure the difference between result of GMTSAR data variables and the result of the LiCSBAS variables. The accuracy test is utilized to determine the level of accuracy of the obtained Line of Sight (LOS) InSAR displacement results. The accuracy test employed is the Root Mean Square Error (RMSE). The equation used in the RMSE calculation is as follows (Ghilani, 2017).

$$\text{RMSE} = \sqrt{\frac{\sum_{i=1}^n [x_{\text{GMTSAR}} - x_{\text{LiCSBAS}}]^2}{n}} \quad 2.7$$

Description:

x_{GMTSAR} : Value on the GMTSAR

x_{LiCSBAS} : Value on the validation data

n : Number of data

The measure of distribution that is most commonly utilized is the standard deviation. When the difference between the spread and the average value is significant, the value of σ_x will be substantial. Conversely, when the spread of the data is relatively small compared to the average value, the value of σ_x will also be decreased. The calculation of standard deviation can be performed using the following formula.

$$\sigma_x = \sqrt{\frac{\sum_{i=1}^n [x_i - \bar{x}]^2}{n-1}} \quad 2.8$$

Description:

x_i : Value on data sample to i...

\bar{x} : Mean of the data sample

σ_x : Standard Deviation

CHAPTER 3 METHODOLOGY

This chapter provides an overview of the research site, Pacitan City in East Java, within the defined boundaries of the predetermined case study. Furthermore, a comprehensive explanation of the various stages of methodology involved in the research process will be provided, which includes a detailed description of the data utilized and the software used.

3.1 The Method

The location used as a case study in this research is the Pacitan City area, the southern part of East Java which is in the coastal area and is located at coordinates $07^{\circ}55'00'' - 08^{\circ}17'00''$ South Latitude and $110^{\circ}55'00'' - 111^{\circ}25'00''$ East Longitude.

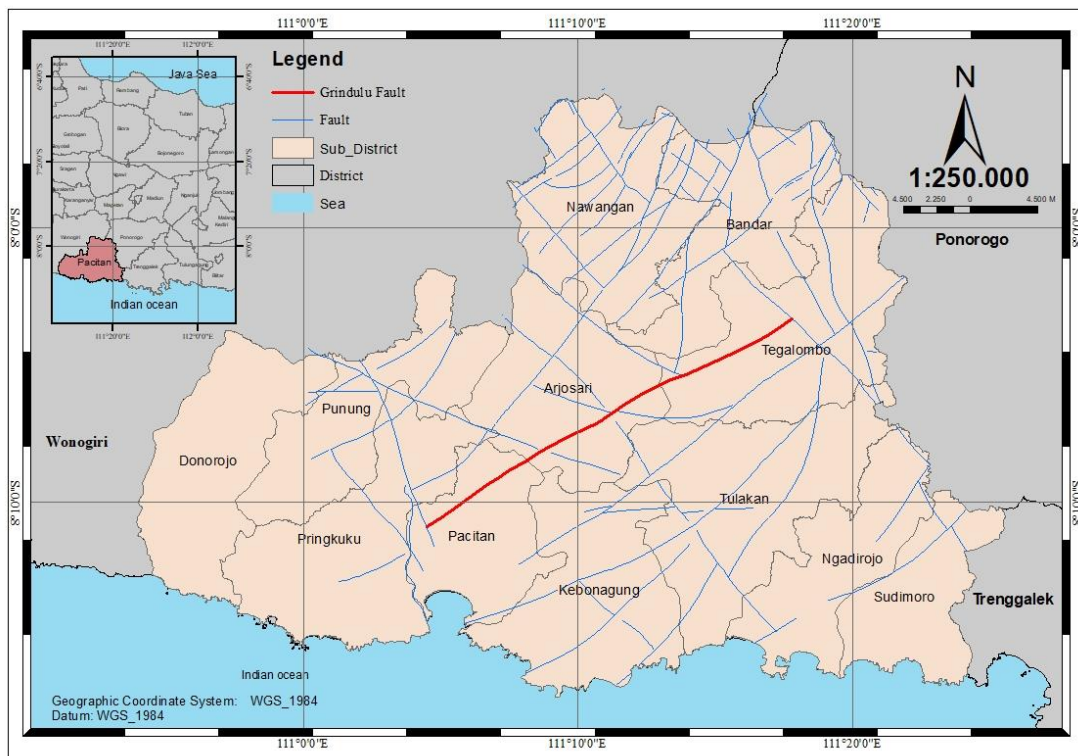


Figure 3.1 Research Location

Based on data from the Pacitan City Central Statistics Agency in 2019, the city of Pacitan has an area of 1,389.87 km² with a population of 596,570 people. The boundaries of Pacitan City are as follows:

- North Side : Ponorogo Regency
- East Side : Trenggalek Regency
- South side : Indian Ocean
- West side : Wonogiri Regency

In this study, Small Baseline Subset (SBAS) technique using sentinel 1B data will be used to get the deformation due to Grindulu fault activities located in Pacitan. The SBAS-InSAR processing will perform using GMTSAR. Then, the result will be analyzed due to natural phenomena are related to Grindulu Fault activities.

3.2 Data and Tools

This section describes the data and equipment that will be used in carrying out the research.

3.2.1 Data

The following are the data needed in this study:

1. The Sentinel-1B Satellite Image Data Set uses the Single Look Complex (SLC) level 1 type and Interferometric Wide (IW) Mode. The recording direction for all images used in ascending direction on the VV polarization path 127 frames 1151 with the recording time from April 21, 2019 to February 21, 2021. 23 SAR data can be downloaded free from the Alaska Satellite Facility website: <https://search.asf.alaska.edu/>

Table 3.1 Sentinel 1B Data

No	ID Scene	Orbit	Date	Level	Direction
1	S1B_IW_SLC__1SSV _20190421T105714_2 0190421T105744_015 903_01DE11_4A44	S1B_OPER_AUX_POEOR B_OPOD_20210302T04261 1_V20190420T225942_201 90422T005942.EOF	April 21, 2019	1.0 (Single Look Complex)	Ascending
2	S1B_IW_SLC__1SSV _20190515T105715_2 0190515T105745_016 253_01E975_8F5E	S1B_OPER_AUX_POEOR B_OPOD_20210302T13522 9_V20190514T225942_201 90516T005942.EOF	Mei 15, 2019	1.0 (Single Look Complex)	Ascending
3	S1B_IW_SLC__1SSV _20190620T105717_2 0190620T105747_016 778_01F942_7E7C	S1B_OPER_AUX_POEOR B_OPOD_20210330T17512 0_V20190619T225942_201 90621T005942.EOF	June 20, 2019	1.0 (Single Look Complex)	Ascending
4	S1B_IW_SLC__1SSV _20190714T105719_2 0190714T105749_017 128_020397_5637	S1B_OPER_AUX_POEOR B_OPOD_20210331T01282 1_V20190712T225942_201 90714T005942.EOF	July 14, 2019	1.0 (Single Look Complex)	Ascending
5	S1B_IW_SLC__1SSV _20190819T105721_2 0190819T105751_017 653_02136A_2893	S1B_OPER_AUX_POEOR B_OPOD_20210331T13462 2_V20190818T225942_201 90820T005942.EOF	August 19, 2019	1.0 (Single Look Complex)	Ascending
6	S1B_IW_SLC__1SSV _20190924T105723_2 0190924T105752_018 178_0223BD_0B66	S1B_OPER_AUX_POEOR B_OPOD_20210304T17532 6_V20190923T225942_201 90925T005942.EOF	September 24, 2019	1.0 (Single Look Complex)	Ascending
7	S1B_IW_SLC__1SSV _20191018T105723_2 0191018T105753_018 528_022E9C_4E05	S1B_OPER_AUX_POEOR B_OPOD_20210305T03303 0_V20191017T225942_201 91019T005942.EOF	October 18, 2019	1.0 (Single Look Complex)	Ascending
8	S1B_IW_SLC__1SSV _20191111T105723_2 0191111T105753_018 878_0239B8_74F4	S1B_OPER_AUX_POEOR B_OPOD_20210305T13283 4_V20191110T225942_201 91112T005942.EOF	November 11, 2019	1.0 (Single Look Complex)	Ascending
9	S1B_IW_SLC__1SSV _20191217T105722_2 0191217T105752_019 403_024A78_A3E8	S1B_OPER_AUX_POEOR B_OPOD_20210306T03522 4_V20191216T225942_201 91218T005942.EOF	December 17, 2019	1.0 (Single Look Complex)	Ascending
10	S1B_IW_SLC__1SSV _20200110T105721_2 0200110T105750_019 753_02559C_EC45	S1B_OPER_AUX_POEOR B_OPOD_20210316T21150 1_V20200109T225942_202 00111T005942.EOF	January 10, 2020	1.0 (Single Look Complex)	Ascending
11	S1B_IW_SLC__1SSV _20200215T105720_2	S1B_OPER_AUX_POEOR B_OPOD_20210317T07261	February 15, 2020	1.0 (Single Look Complex)	Ascending

No	ID Scene	Orbit	Date	Level	Direction
	0200215T105749_020 278_02667B_2769	0_V20200214T225942_202 00216T005942.EOF			
12	S1B_IW_SLC__1SSV _20200322T105720_2 0200322T105749_020 803_027737_8026	S1B_OPER_AUX_POEOR B_OPOD_20210317T17291 1_V20200321T225942_202 00323T005942.EOF	March 22, 2020	1.0 (Single Look Complex)	Ascending
13	S1B_IW_SLC__1SSV _20200415T105720_2 0200415T105750_021 153_028246_AA4D	S1B_OPER_AUX_POEOR B_OPOD_20210318T00084 9_V20200414T225942_202 00416T005942.EOF	April 15, 2020	1.0 (Single Look Complex)	Ascending
14	S1B_IW_SLC__1SSV _20200521T105722_2 0200521T105752_021 678_029276_CE3E	S1B_OPER_AUX_POEOR B_OPOD_20210318T10223 5_V20200520T225942_202 00522T005942.EOF	Mei 21, 2020	1.0 (Single Look Complex)	Ascending
15	S1B_IW_SLC__1SSV _20200614T105724_2 0200614T105753_022 028_029CEE_2BE0	S1B_OPER_AUX_POEOR B_OPOD_20210318T17024 1_V20200613T225942_202 00615T005942.EOF	June 14, 2020	1.0 (Single Look Complex)	Ascending
16	S1B_IW_SLC__1SSV _20200720T105726_2 0200720T105755_022 553_02ACEC_6092	S1B_OPER_AUX_POEOR B_OPOD_20210316T22035 6_V20200719T225942_202 00721T005942.EOF	July 20, 2020	1.0 (Single Look Complex)	Ascending
17	S1B_IW_SLC__1SSV _20200825T105728_2 0200825T105758_023 078_02BD22_CD49	S1B_OPER_AUX_POEOR B_OPOD_20210317T08114 1_V20200824T225942_202 00826T005942.EOF	August 25, 2020	1.0 (Single Look Complex)	Ascending
18	S1B_IW_SLC__1SSV _20200918T105729_2 0200918T105759_023 428_02C816_02F3	S1B_OPER_AUX_POEOR B_OPOD_20210317T14555 7_V20200917T225942_202 00919T005942.EOF	September 18, 2020	1.0 (Single Look Complex)	Ascending
19	S1B_IW_SLC__1SSV _20201012T105729_2 0201012T105759_023 778_02D2FB_AE81	S1B_OPER_AUX_POEOR B_OPOD_20210317T21341 2_V20201011T225942_202 01013T005942.EOF	October 12, 2020	1.0 (Single Look Complex)	Ascending
20	S1B_IW_SLC__1SSV _20201129T105729_2 0201129T105758_024 478_02E8E9_113D	S1B_OPER_AUX_POEOR B_OPOD_20210318T10584 2_V20201128T225942_202 01130T005942.EOF	November 29, 2020	1.0 (Single Look Complex)	Ascending
21	S1B_IW_SLC__1SSV _20201223T105727_2 0201223T105757_024 828_02F43E_23CF	S1B_OPER_AUX_POEOR B_OPOD_20210318T17391 1_V20201222T225942_202 01224T005942.EOF	December 23, 2020	1.0 (Single Look Complex)	Ascending
22	S1B_IW_SLC__1SSV _20210128T105726_2 0210128T105756_025 353_03050A_4308	S1B_OPER_AUX_POEOR B_OPOD_20210217T11175 1_V20210127T225942_202 10129T005942.EOF	January 28, 2021	1.0 (Single Look Complex)	Ascending
23	S1B_IW_SLC__1SSV _20210221T105725_2 0210221T105755_025 703_03106F_9DE3	S1B_OPER_AUX_POEOR B_OPOD_20210313T11233 3_V20210220T225942_202 10222T005942.EOF	February 21, 2021	1.0 (Single Look Complex)	Ascending

2. DEM SRTM (Shuttle Radar Topography Mission) 30 meters to reduce the effect of topography on InSAR processing which is downloaded from GMTSAR - Generate DEM (ucsd.edu) (Sandwell et al., 2011).

3. The COMET LiCSAR product. The ID interferogram Frame that used is 127A_09749_121312 with ascending format between April 2019 and February 2021

4. Supporting data include Precise Orbit Ephemeris (POE), geological data, records of tectonic earthquakes around the fault during the research observation period, and other supporting data, such as administrative boundary data sourced from the 1: 25,000 scale Indonesian Topographic Map (RBI) by the Geospatial Information Agency. Precise Orbit Ephemeris (POE) is a collection of orbital elements of a satellite or other celestial objects that are extremely precise.

3.2.2 Tools

The tools that used in this research consist of hardware and software. The following equipment is used.

1. Hardware

ASUS PC Intel core i7, 64 Gb memory, 1 Tb hard drive is used for all data processing and report writing.

2. Software

- GMTSAR (Sandwell et al., 2011) is used for SBASInSAR data processing.
- LiCSBAS (Morishita et al., 2020) is used for SBASInSAR data processing.
- Generic Mapping Tool (GMT) is used for plotting and coding the results of SAR data processing (Wessel et al., 2019).

3.3 Research Methodology

3.3.1 Research Stages

The stages of research implementation of this research are described on the flowchart as follows.

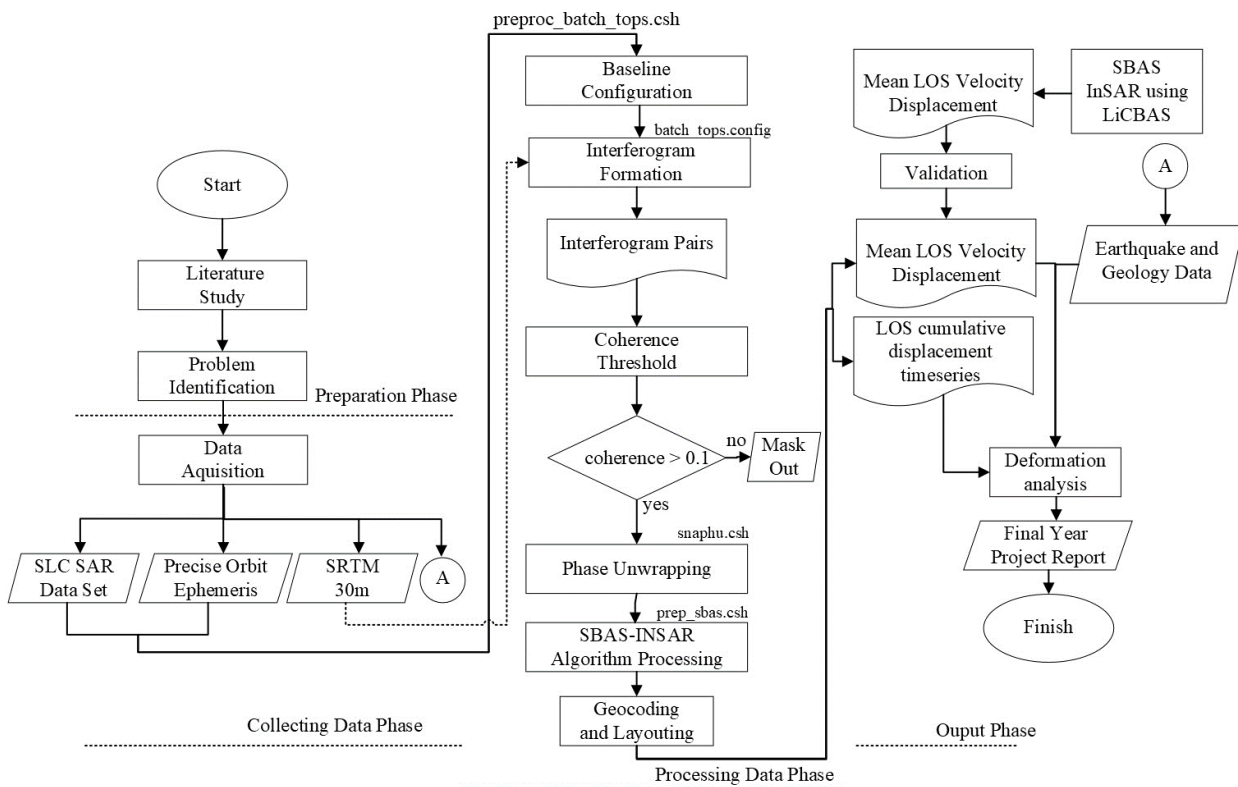


Figure 3.2 Research Flowchart

The following is an explanation of the stages of the research flow chart above.

1. Preparation phase

a. Problems Identification

The problem in this research is how to find out the deformation in Pacitan City as a result of Grindulu Fault activities. In this study, using Sentinel-1B image data with acquisition between April 2019 and February 2021 using the SBAS InSAR technique to get the deformation value.

b. Literature Study

The literature study aims to obtain references related to the study and get to know the concepts and materials associated with the research for the Final Project, including the discussion of the Grindulu Fault, SAR, SBAS-InSAR, GMTSAR, LiCSBAS, and other literature.

2. Collecting Data phase

In this activity, data collection is performed to support the research. The collected data includes:

a. The Sentinel-1B Satellite Image Data Set uses the Single Look Complex (SLC) level 1 type because it has provided at the full native resolution (single look) with both amplitude and phase information stored in each (complex) pixel.

b. Precise Orbit ephemeris, it is used to calculate the exact position of the body in space at any given moment. The Precise Orbit Ephemerides data span approximately 28 hours and contain orbit state vectors at fixed 10-second intervals. After data collection, one file is generated daily and given within 20 days (Flores-Anderson et al., 2018).

c. NASA SRTM Digital Elevation 30m data are utilized for this procedure. This is due to the fact that the SRTM data utilizes the Ellipsoid reference and the WGS84 vertical datum, whereas the DEMNAS data utilizes the MSL reference and the EGM2008 vertical datum.

d. Earthquake data from the Grindulu Fault and geological data from the Pacitan district are supporting data for deformation analysis due to Grindulu Fault activities.

e. COMET LiCSAR product with ID interferogram Frame that used is 127A_09749_121312 ascending format between April 2019 and February 2021.

3. Processing Data Stage

a. Baseline Configuration

In the SBAS-InSAR network configuration stage, the design of multi-master pairs with slave images is modified according to the spatial distance and temporal baseline threshold settings to cross-correlate the image pairs to the primary master image.

b. Interferogram Formation

The formation of an interferogram from each image will produce a phase difference where this phase difference can indicate the initial identification of changes on the earth's surface.

c. Coherence Threshold

To reduce the low coherence, it can be limited according to the desired coherence threshold. At this stage, pixels that have more coherence than the specified coherence threshold will be selected while those with less will be masked out. Practically, for the necessity for InSAR applications, the recommended coherence value must be greater of 0.2. According to Elias, SBAS processing with minimum coherence threshold of 0.1 give

the large pixels that contain at least two small pixels from the original set and this coherence is good enough to provide very accurate information in many areas in the rift of Corinth, Greece (Elias et al., 2018).

d. Phase Unwarping

The wrapped phase in each interferogram is modulo 2π ($-\pi, \pi$), where this value must go through an unwrapping process to get the actual phase value. This processing stage is carried out based on unwrapped phase calculations which are carried out using the SNAPHU program available at GMTSAR. The unwrapping phase process is carried out by running the command "snaphu.csh."

e. SBAS INSAR algorithm processing

This stage aims to obtain the mean LOS of displacement as well as the cumulative displacement along the LOS from April 2019 to February 2021. The algorithm that will use has been explained in equation 2.2 to 2.5.

f. Geocoding and Layouting

The geocoding process was carried out to ensure that all data with range and azimuth coordinates had been converted into a geographic coordinate system (latitude and longitude). While layouts are done using GMT software.

g. Validation

The validation process is based on the result of Mean LOS displacement from LiCBAS. The geological and geomorphological conditions to support the analysis with deformation maps. The geological map depicts the distribution and characteristics of rock formations, soil types, and other geomorphology features in Pacitan based on different color. Different colors represent different rock types, geological formation, and fault lines. While the deformation maps, on the other hand, show the mean LOS displacements that occur in Pacitan.

4. Output Stage

The deformation analyses presented in this study are in the form of tabular, graphical, and image, as follows:

- Analysis of mean LOS displacements in the area around the Grindulu Fault
- Analysis of Grindulu Fault activities based on deformation in relation to the geological conditions of the Pacitan region.
- Analysis of surface deformation concerning the presence of the Grindulu Fault activities related to the earthquake

3.3.2 SAR Data Processing Stages Using GMTSAR

The following are the stages of SBAS InSAR processing using GMTSAR described as follows.

1. Prepare the directory folder "raw" containing a file of scene sentinel 1B IW , POE, dem.grd dan data.in

*data.in is a file that contains a list of satellite images and POE

Open Terminal in the raw folder and run the following commands with mode = 1

```
preproc_batch_tops.csh data.in dem.grd 1
```

The command will produce file of baseline.ps, baseline_table.dat and gmt.history

- Copy the `baseline_table.dat` file in the F2 folder to the raw folder. Then open the `data.in` file and move the image selected as the Master image to the first row and save the file. Open the Terminal in the raw folder and run the following command.

```
preproc_batch_tops.csh data.in dem.grd 2
```

- Open the `baseline_table.dat` file in the F2 folder and replace the first column with the name of the images created with the SLC format images in the raw folder. A blank text file named `intf.in` in the F2 folder, then open the Terminal in the F2 folder and run the following commands.

```
select_pairs.csh baseline_table.dat 90 150
```

The number 90 is the temporal baseline (day), and 100 is the spatial baseline (m) and the output file `intf.in` contains a pair of interferograms with a temporal baseline of fewer than 90 days and the spatial baseline is less than 100 meters.

This command will produce `intf.in` a file that shows the list of interferograms, and the `baseline.ps` file shows the network of interferogram graphs.

- Download the `batch_tops.config` file from the following address and place it in the F2 folder. Open the `batch_tops.config` file and set the following parameters and finally save the file.

```
# filter_wavelength = 100
# threshold_snaphu = 0.1
# threshold_geocode = .1
For complete file in appendix
```

Create a text file called `one.in` and copy and save the Master image name as one of the Slave images and place it in the F2 folder. Then open the terminal in folder F2 and run the following commands.

```
intf_tops.csh one.in batch_tops.config
```

In this part, the value of the DEM or topography is converted to phase.

- After running the above command, open the `batch_tops.config` file again and set and save `proc_stage = 2`

Then open the Terminal in the F2 folder and run the following commands.

```
intf_tops.csh intf.in batch_tops.config
```

In this step, the filter is applied to the interferogram logs. The output of the above command includes the generated interferograms folder.

- Running Small Baseline Subset (SBAS) Analysis. First, create a folder called SBAS in folder F2. Prepare the Input Files : `scene.tab` and the `intf.tab`. Use a script called `prep_sbass.csh`, this script creates the `scene.tab` file, the `intf.tab` file, and outputs a default SBAS command structure for the user. Check and see if you have this in your distribution by typing “`prep_sbass.csh`” into your command line and see if the usage pops up. If you do not have it, feel free to check GitHub and download it there.

```
prep_sbas.csh intf.in baseline_table.dat ../intf_all
unwrap.grd corr.grd
```

Note: need to give it the list of interferograms (intf.in), the list of baselines (baseline_table.dat), the path to the merge directory where it will find the unwrapped interferogram grids and correlation grids, the name of the unwrapped file (unwrap.grd) file, and the name of the correlation grid file (corr.grd)

7. Type “sbas” into the command line to read about the usage and see example commands.

```
Usage: sbas intf.tab scene.tab N S xdim ydim [-atm ni] [-
smooth sf] [-wavelength wl] [-incidence inc] [-range -rng]
[-rms] [-dem]
```

+N means the number of interferograms being run,

+S means the number of scenes being included,

+xdim and ydim mean the dimension of the interferograms. To get (xdim, xmin, xmax) and (ydim, ymin, ymax) run the following commands in one of the interferogram folders.

“x n_columns” is the value for x dim

“y n_rows” is the value for y dim

+wavelength: wavelength of the radar wave in m. To find this out, look in supermaster.PRM for “radar_wavelength

+incidence: the default value is 37 degrees, though the value used here is largely relevant (the default is fine in most cases). Or to get the angle, you can use SNAP software or image information (Tie-Point Grids).

+range: range distance from the radar to the center of the interferogram. To get this number for Sentinel-1:

```
Range = ( { [(speed of light) / (rng_samp_rate) / 2] *
((x_min+x_max)/2)} / 2 ) + near_range
```

```
Range = ( { [(3x108) / (64345238.125714)/2] * ((0+24544)/2)} / 2 ) +
845000
Range = 859304.0888
```

Speed of light is $\sim 3 \times 10^8$ m/s

“rng_samp_rate” is in supermaster.PRM

X_min and x_max come from the gmt grdinfo command above

“near_range” is in supermaster.PRM

+rms tells the program we want it to output a grid of rms values (in mm)

+dem tells the program we want it to output the dem error (in m)

Open the Terminal in the SBAS folder and run the following commands.

```
sbas intf.tab scene.tab 50 23 3068 6762 -smooth 1.0 -wavelength
0.0554658 -incidence 38 -range 859304.0888 -rms -dem
```

8. After running SBAS, the output is a vel.grd file (in radar coordinates, and in mm/yr). To transform it into lat/long coordinates, do the following:

```
ln -s ../topo/trans.dat
ln -s ../intf_all/2019110_2019170/gauss_*
proj_ra2ll.csh trans.dat vel.grd vel_ll.grd
gmt grd2cpt vel_ll.grd -T= -Z -Cjet > vel_ll.cpt
grd2kml.csh vel_ll vel_ll.cpt
```

vel_ll.png and vel_ll.kml files of the SBAS time-series map

- Then running the following commands to create the time series of the Displacement value in the Terminal

# proj_ra2ll.csh trans.dat	# proj_ra2ll.csh trans.dat
disp_2019110.grd disp_2019110_ll.grd	disp_2020081.grd disp_2020081_ll.grd
# proj_ra2ll.csh trans.dat	# proj_ra2ll.csh trans.dat
disp_2019134.grd disp_2019134_ll.grd	disp_2020105.grd disp_2020105_ll.grd
# proj_ra2ll.csh trans.dat	# proj_ra2ll.csh trans.dat
disp_2019170.grd disp_2019170_ll.grd	disp_2020141.grd disp_2020141_ll.grd
# proj_ra2ll.csh trans.dat	# proj_ra2ll.csh trans.dat
disp_2019194.grd disp_2019194_ll.grd	disp_2020165.grd disp_2020165_ll.grd
# proj_ra2ll.csh trans.dat	# proj_ra2ll.csh trans.dat
disp_2019230.grd disp_2019230_ll.grd	disp_2020201.grd disp_2020201_ll.grd
# proj_ra2ll.csh trans.dat	# proj_ra2ll.csh trans.dat
disp_2019266.grd disp_2019266_ll.grd	disp_2020237.grd disp_2020237_ll.grd
# proj_ra2ll.csh trans.dat	# proj_ra2ll.csh trans.dat
disp_2019290.grd disp_2019290_ll.grd	disp_2020261.grd disp_2020261_ll.grd
# proj_ra2ll.csh trans.dat	# proj_ra2ll.csh trans.dat
disp_2019314.grd disp_2019314_ll.grd	disp_2020285.grd disp_2020285_ll.grd
# proj_ra2ll.csh trans.dat	# proj_ra2ll.csh trans.dat
disp_2019350.grd disp_2019350_ll.grd	disp_2020333.grd disp_2020333_ll.grd
# proj_ra2ll.csh trans.dat	# proj_ra2ll.csh trans.dat
disp_2020009.grd disp_2020009_ll.grd	disp_2020357.grd disp_2020357_ll.grd
# proj_ra2ll.csh trans.dat	# proj_ra2ll.csh trans.dat
disp_2020045.grd disp_2020045_ll.grd	disp_2021027.grd disp_2021027_ll.grd
	# proj_ra2ll.csh trans.dat
	disp_2021051.grd disp_2021051_ll.grd

3.3.3 SAR Data Processing Stages Using LiCSBAS

The following are the stages of SBAS InSAR processing using LiCSBAS described as follows.

- In this step, identify the frame id that will use in the process around area of interest. So the ID Frame that uses is 127A_09749_121312. Make the directory folder with ID frame "127A_09749_121312"

```
cd/home/labuser5/anis_TA
mkdir 127A_09749_121312
cd /127A_09749_121312
```

- Download Batch Processing from the Website
This step downloads the prepared batch script of LiCSBAS processing

```
wget
https://raw.githubusercontent.com/yumorishita/LiCSBAS/documents/batch\_LiCSBAS\_sample\_CF.sh
```

Change some parameter and run it:

In this step some parameters change such as:

```
start_step="01" # 01-05, 11-16
end_step="16"# 01-05, 11-16
do05op_clip="y" # y/n
p05_clip_range_geo="110.91/111.40/-8.27/-7.88" # e.g.
130.11/131.12/34.34/34.6 (in deg)
p01_start_date="20190420" # default: 20141001
p01_end_date="20210222" # default: today
p11_coh_thre="0.1" # default: 0.05
```

```
chmod 764 batch_LiCSBAS_sample_CF.sh
./batch_LiCSBAS_sample_CF.sh
```

7. Display the derived time series and velocity.

```
LiCSBAS_plot_ts.py -i TS_GEOCml1clip/cum_filt.h5 &
```

8. Convert outputs to a standard NetCDF4 file using LiCSBAS results.

```
LiCSBAS_out2nc.py [-i infile] [-o outfile] [-m yyymmdd] [--ref_geo
lon1/lon2/lat1/lat2] [--clip_geo lon1/lon2/lat1/lat2]
```

```
LiCSBAS_out2nc.py -i TS_GEOCml1clip/cum_filt.h5 -o pacitan.nc --
ref_geo 110.91/111.40/-8.27/-7.88 --clip_geo 110.91/111.40/-8.27/-
7.88
```

CHAPTER 4

RESULT AND DISCUSSION

Chapter 4 presents the results of processing the SBAS-InSAR time series technique using the GMTSAR software, which maps the ground surface deformation around the Grindulu Fault. These results explain the relationship between the phenomenon of ground deformation and the characteristics of the grindulu fault's tectonic motion, along with the geomorphology and geology of the area around the fault segment. In addition, it also analyzes the results of the statistical test of the SBAS-InSAR results with LiCSBAS processing data.

This study utilized 23 Sentinel-1B images (IW mode) which cover the area around the Grindulu fault, especially from April 2019 to February 2021. The choice of Ascending Sentinel-1B images is because ESA has provided precise orbit data; this information is needed in the processing stage to improve the geometric accuracy of the image, while the DEM SRTM1" (30 m resolution) was chosen to adjust the spatial resolution of the Sentinel-1B image, which is 20 m, it is hoped that it can also maximize the topography effect removal process.

4.1 Small Baseline Interferometric SAR

This sub-chapter describes the results of SBAS-InSAR processing based on an outline sequence of processing, including the formation of image baseline configurations, interferograms, and phase unwrapping to produce deformation maps that contain velocity SAR information in LOS and LOS in a time-series.

4.1.1 Baseline Configuration

Considering the temporal and perpendicular baselines, the baseline position distribution of the 23 SAR images is presented according to their respective roles, with one image as the master and the other as an enslaved person. Figure 4.1 shows the distribution of the position of the scene center in each SAR image based on the perpendicular and temporal baseline. The image recorded on April 21, 2019, was chosen as the master with a zero baseline, while the other 22 images acted as slaves. The 22 slave images have been aligned geometrically with the master image. The selection of data pairs involved in the design of the interferogram is essential to the Small Baseline technique because it minimizes the spatial and temporal baseline between acquisition orbits, thereby reducing decorrelation (Lanari et al., 2007). The strategy for interferogram formation was determined using a perpendicular baseline of 150 m and a temporal baseline of 90 days. The perpendicular baseline distance is less than 150 meters, assuming there are no isolated images in the baseline installation and that the number of images does not exceed the critical baseline image limit. In addition, it conforms to the perpendicular baseline threshold used for topographic mapping, which varies between 100 m and 500 m based on the topographic terrain's ruggedness. Figure 4.1 depicts the small baseline image configuration results, where the black line represents the result of installing the baseline between adjacent images to carry out the interferogram process.

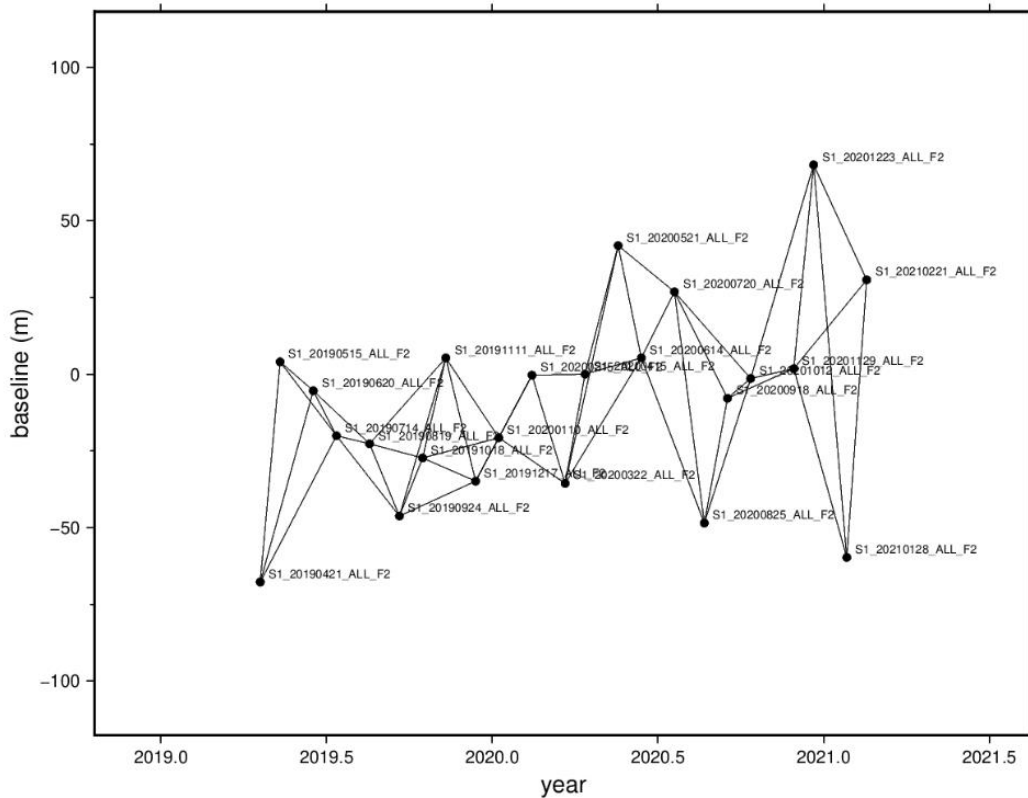


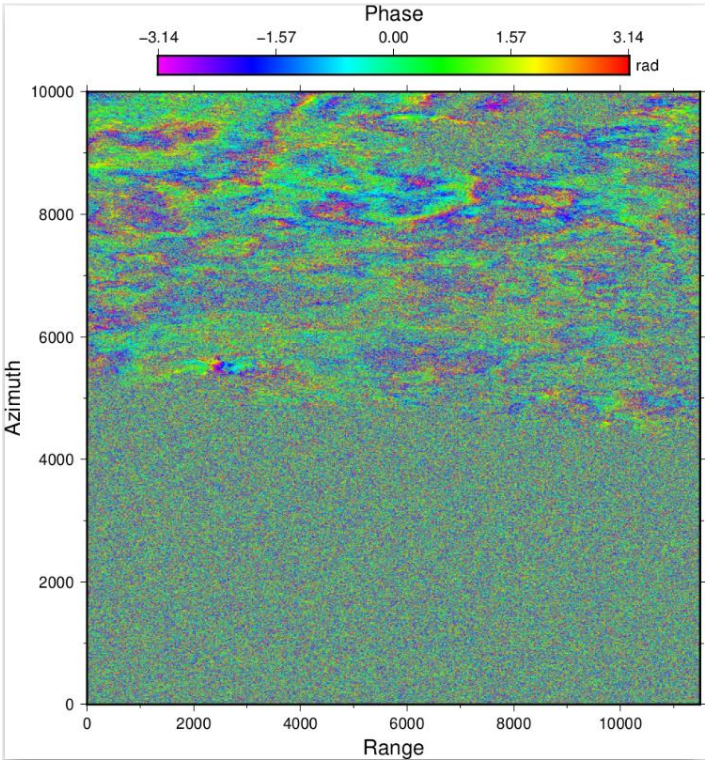
Figure 4.1 The Combination of 50 Interferogram Pairs base on Temporal and perpendicular baseline.

According to Ferretti et al. (2007), the perpendicular baseline refers to a projection perpendicular to the oblique distance between satellites in two distinct orbits. The baseline parameter indicates the degree of sensitivity to changes in topographical elevation, the extent of decorrelation present in the phase gradient, and the efficacy of the phase unwrapping procedure. The temporal baseline refers to the duration between image datasets, and the coherence formation between images is influenced by the time interval separating them. Where the smaller the baseline, the higher coherence is expected. The use of perpendicular and temporal baselines that are too large is one of the reasons for the increased decorrelation of the interferogram due to the weak coherence of the image pair (Çomut et al., 2012). If the image's coherence decreases, the interferogram's quality will decrease, but the quantity of pixels increases, and more and more images are isolated. Therefore, to get a good coherence value in the image pair, a perpendicular baseline of less than 150 m and a temporal baseline of less than 90 days. So, it can be seen that the image pair used in this study have good quality.

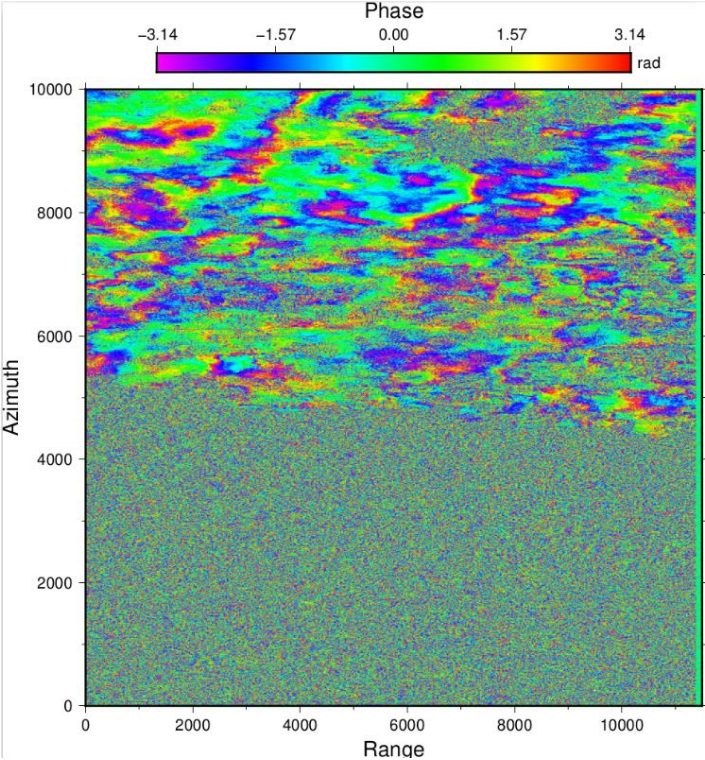
4.1.2 Interferometric Phase

At the interferogram generation stage, the InSAR method will produce interferogram imagery through complex multiplication of master imagery against slave imagery to obtain amplitude and phase information. The interferogram shows the phase difference between the two images depicted in the form of fringes. Fringes are the oscillations of an electromagnetic wave signal with a specific wavelength that repeats as far as 2π ($-\pi$ to π). One fringe, specifically on Sentinel-1, represented a displacement of 5.6 cm from the radar sensor. The figure below shows the phase interferogram, which still contains various phase value contributions due to

noise, deformation, signal delays in the atmosphere, orbit errors due to shifts, and topographical effects. The interferogram results show color transitions, specifically from red to blue and blue to red. These color transitions are interpreted as phase variation values ranging from 0 to 3.14 (π) radians and from 3.14 (π) to 6.28 (2π) radians, respectively. The interferogram image has been subtracted by topographical effects in the radar coordinate system to reduce topographical effects on interferogram images using DEM SRTM 30 meters.



(a)



(b)

Figure 4.2 Interferogram Phase (a) and Filtered Phase (b)

Filtering the interferogram is carried out in order to the amount of speckle noise it contains can be reduced. The goal of the interferogram filtering process is to reduce the amount of noise produced by temporal decorrelation and other sources of noise in order to improve the area's sharpness or visibility. In the current case, GMTSAR operates with its default setting of a Gaussian filter applied to the data. The results of this filtering procedure are presented in the top figure; compared to the unfiltered phase (Figure 4.2a), the results of the filtered phase display better pixel information (Figure 4.2b). After going through the filtering procedure, which makes the fringes more visible, one can observe this shift in the shape of the fringes.

4.1.3 Interferogram Coherence

Coherence shows how far each pixel is similar between the master and slave images with a value between 0 and 1. Missing or empty data at some pixels (zero coherence) is caused by temporal decorrelation, so the coherence value decreases.

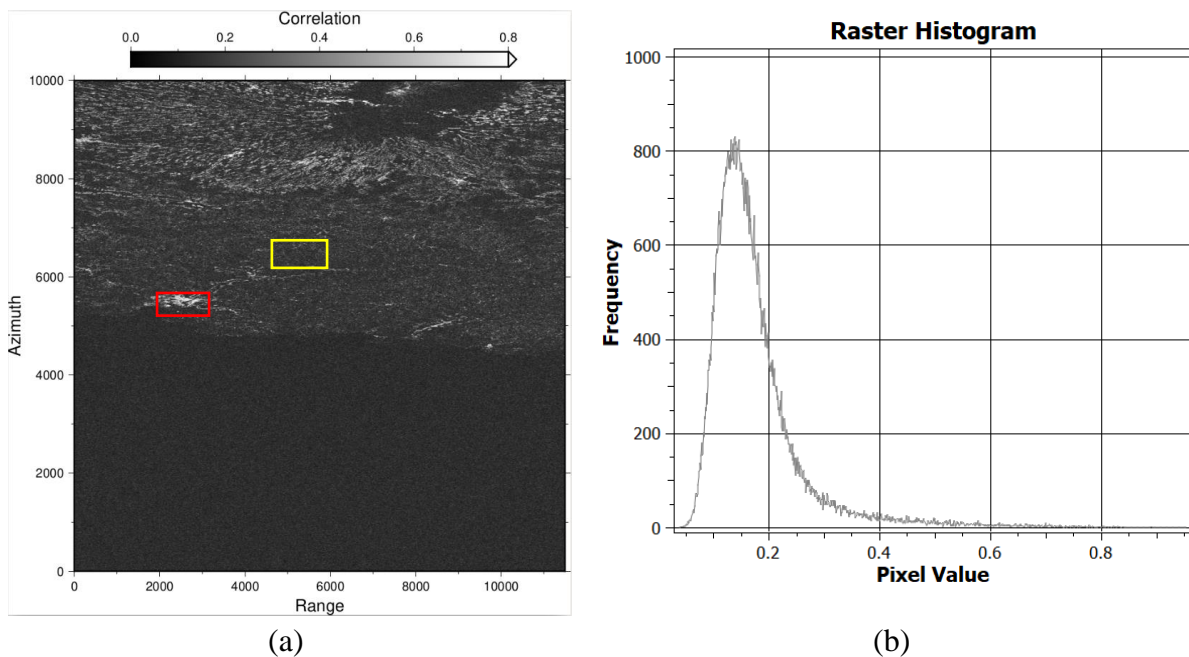


Figure 4.3 Coherence Image (a); Histogram of Coherence (b)

Figure 4.3 is an example of the coherence value of the image pair 20190421 and 20190515. Half of the image is the Sea or water body with close to 0 coherence and the area around Mountainous also vegetation is shown in dark grey (low coherence). In contrast, few of urban areas are shown in white or light grey (high coherence). The water area has a low coherence value even close to 0 with black because water bodies move constantly. Therefore, it can be seen that several regions do not have pixel information due to low coherence values and cause blanks or empty pixels after the unwrapping process.

Based on the processing, coherence values were obtained overall, whereas for the Ascending SAR image, the range of values is from 0.05 to 0.15. it can be concluded that the average coherence of the images is between 0.1 and 0.2. The red box in Figure 4.3a shows that the location in the city of Pacitan has pixels with a high average coherence value because the location is an urban area with dense settlements. Whereas the yellow box in Figure 4.3b for mountainous locations and dense vegetation shows that most of these areas have dark-colored

pixels indicating low coherence. This is because the area is a non-urban area where there are still many canopies of various vegetation with leaf movements, plant types, height and changes in vegetation that vary so that it can affect high and low coherence. According to (Ferretti et al., 2007) a good interferogram quality level is if 50% of the pixels have a coherence value above 0.8. Based on this criterion, it means that the interferogram produced in the interferometric image pair is included in the low coherence interferogram.

4.1.4 Phase Unwrapping

The resulting image from processing after filtering is still in radian units with a modulo of 2π , so the value is ambiguous. Therefore, to relate the interferometric phase to the topographical elevation, the phase must be calculated first. Altitude ambiguity is defined as the difference in altitude that results in an interferometric phase change of 2π . Phase unwrapping solves this ambiguity by integrating the phase differences between neighboring pixels. The result of the unwrapping phase is the absolute phase value of the deformation (displacement). The unwrapped phase is a deformation calculation from satellite observations. A negative value (-) indicates an uplift, meaning that the signal is going to the radar sensor, or the distance is decreasing. In contrast, a positive value (+) indicates subsidence, meaning the signal moves away from the signal or increases the distance.

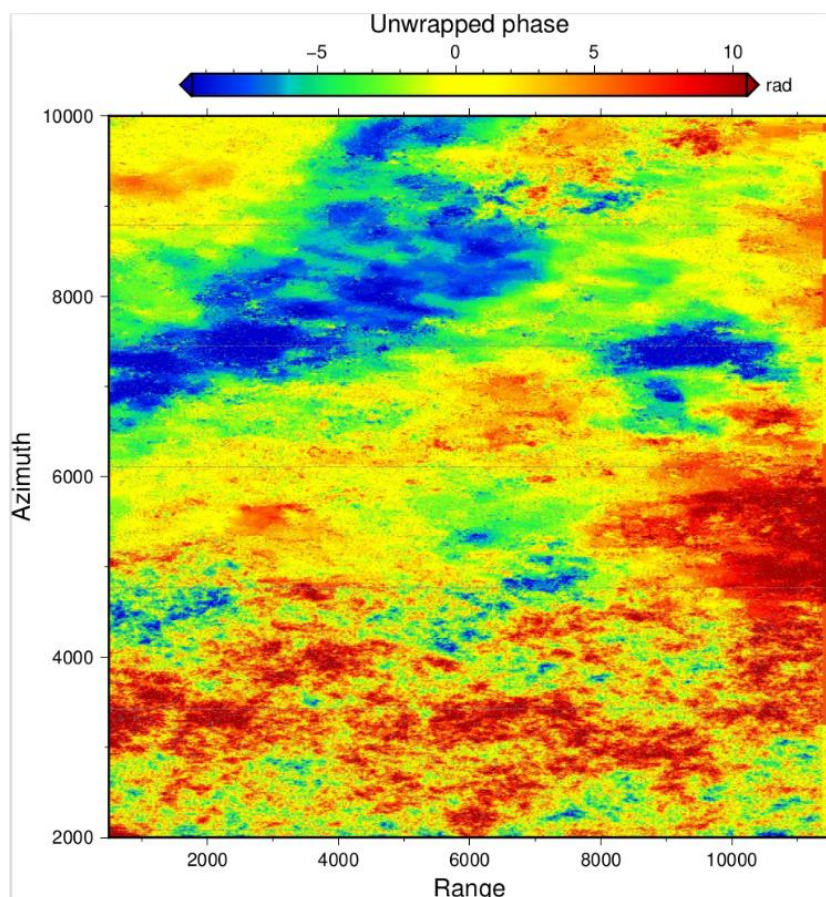


Figure 4.4 Unwrapped Phase

4.1.5 LOS Displacement

After the unwrapping phase process, the LOS displacement value is obtained. This value indicates the magnitude of one-dimensional vertical deformation along the Line-of-Sight Displacement (Ferretti et al., 2007 ; Sandwell et al., 2011). Displacement along LOS refers to a change in shape or a shift in the direction of the observer's line of sight (Line of Sight). This deformation occurs when there is a change in the position or shape of the observed object relative to the observer, where the InSAR results are obtained from the satellite's line of sight. In two SAR images taken at different times it is used to calculate the change in distance in the direction of the observer's line of sight. So, we can see the relative movement between the two sides of the fault; the deformation in the direction of LOS will indicate a shift in the fault.

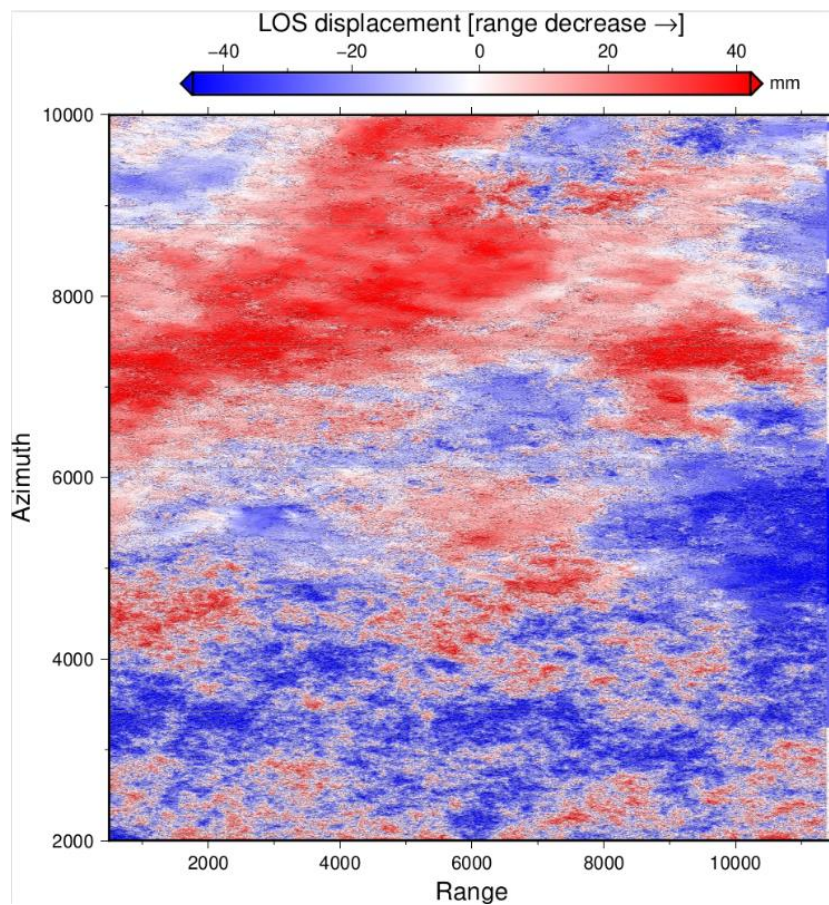


Figure 4.5 LOS Displacement

In the example above, the results of LOS Displacement can be seen that occurred in the southeast tended to move away from the satellite or subsidence to a few millimeters represented in blue color. At the same time, several other areas experienced an subsidence phenomenon described in blue color. The amount of deformation to the line of sight (LOS) with a value of -40 mm to 40 mm. By monitoring deformation in the LOS direction over time, we can understand changes in the shape or position of the object being observed and identify deformation patterns and trends that may be related to geological or geodynamic activity.

4.2 Results and Analysis of SBAS InSAR

In this sub-chapter, the result of SBAS-InSAR processing using GMTSAR is in the form of a deformation value in millimeters around the Grindulu fault (disp1, disp2, disp3).

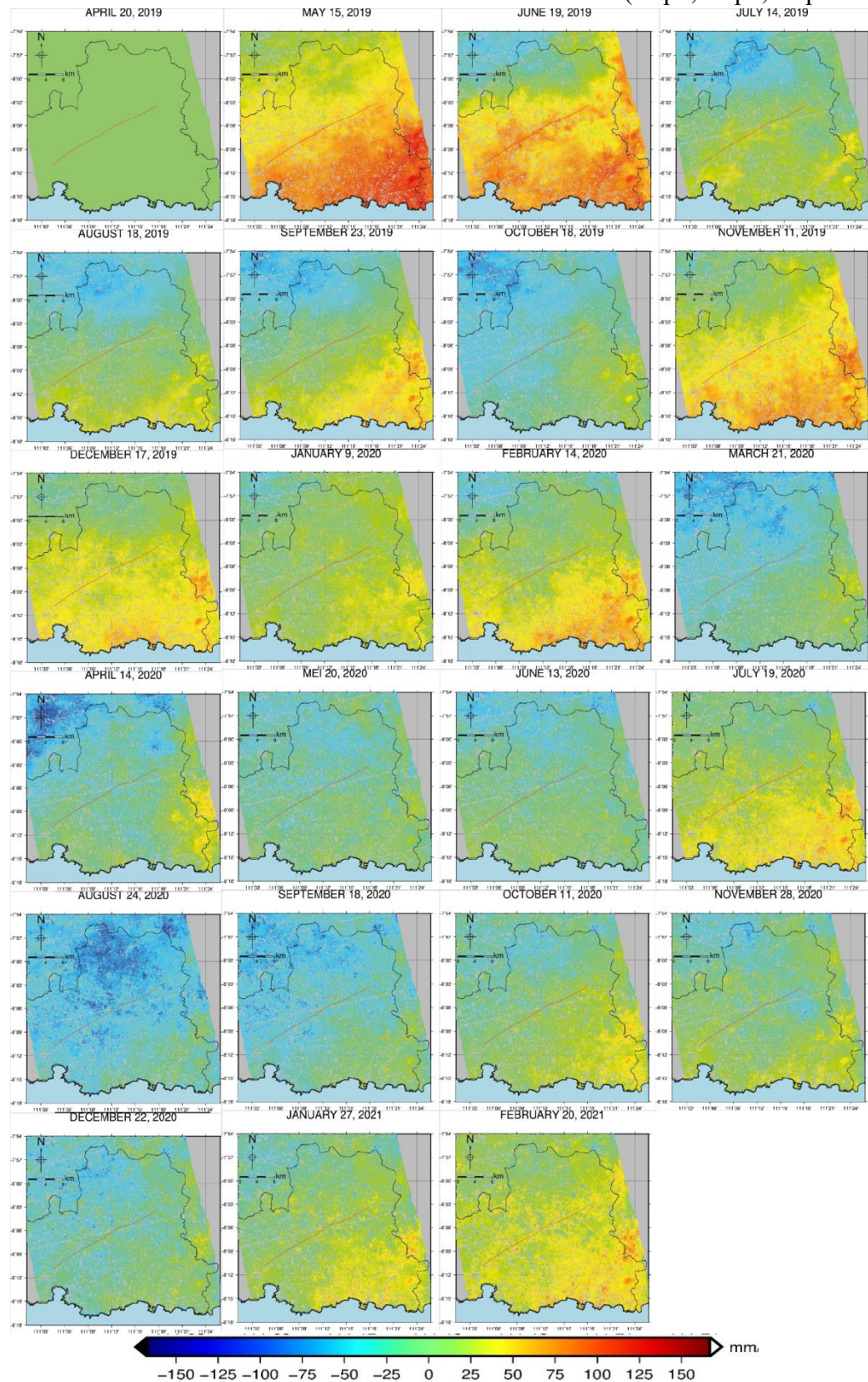


Figure 4.6 Displacement Time-Series between April 2019 and February 2021.

Analysis of the results of the displacement time-series shows deformation changes from 23 observations sequentially, the mean LOS velocity, where the Blue color indicates land subsidence (-), while Red is uplift (+). Based on the mean LOS velocity value from SBAS processing, we can understand the pattern of deformation of the Earth's surface, especially related to the movement of tectonic plates or fault activity. Mean LOS velocity refers to the average change in distance or shift of the Earth's surface in the direction of the line of sight from the satellite, which is calculated from a series of SAR images that have been processed using the SBAS method. Figure 4.6 presents the outcomes of the SBAS InSAR in the form of Displacement Time-Series values, with the reference image is April 20, 2019. At that date, the value of the displacement is either regarded as 0 or is utilized as a reference for determining the displacement. Based on the reference image, April 20, 2019, there tends to be an uplift phenomenon in the southeast fault zone, as seen in the images on May 15 and June 19, 2019. On the other hand, the results of SBAS InSAR in July–October 2019 and March–September 2020 show that the phenomena are dominated by subsidence to the northwest of the fault.

Atmospheric temperature and humidity can affect the propagation of radar waves in the atmosphere. Changes in temperature and humidity can cause refraction of radar waves when passing through the atmosphere, which in turn can cause interferometric distortion between two radar images taken at different times. This phenomenon is known as "atmospheric phase screen" and causes noise or inaccuracies in InSAR processing results (Syahputri et al., 2023). Observations show significant values (uplift reaches more than 15 cm), in May 2019 and June 2019, this is likely due to the large noise contribution contained in the three images. The contribution of noise to the Earth's atmosphere can reduce the accuracy of the LOS displacement results for that month, so it needs to be compared with the daily temperature, humidity and rainfall conditions obtained from BPS data.

- Data in May 2019, compared to Pacitan BPS data shows significant displacement occurred around the Ngadirojo and Sudimoro sub-districts because the maximum temperature on May 2019 reached 28°C with an average humidity of 27.26%. Meanwhile, the rainfall from April to May is quite high in that period, 271-1763 mm. Therefore, the results in Figure 4.6 show a significant increase in ground level compared to the other image pairs.
- The April and June 2019 image pairs compared to Pacitan BPS data show significant displacement occurring around the Ngadirojo sub-district adjacent to the Lorok fault. The uplift phenomenon occurs due to noise in the image which at that time indicates that the maximum temperature in June 2019 reached 30.2°C, the average humidity of 26.52% is quite high in 2019.

Apart from being due to atmospheric factors which cause noise in processing results, several phenomena such as landslides recorded by BNPB Pacitan cause land subsidence. For example, in December 2019 there was a landslide in the Bandar sub-district, so it can be seen in Figure 4.6 for November-December 2019 that it also shows a subsidence phenomenon in the northwest of Pacitan. In November 2020 there were landslides around the Bandar and Tegalombo sub-districts, this shows the phenomenon of subsidence due to landslides as shown in Figure 4.6 in December 2020.

To be able to understand the existence of ground deformation in 2019-2021 around the Grindulu Fault, sample point distribution was taken in the northern part, such as A1, B1 and C1, while in the southern part, are A2, B2, and C2. The sampling point is around 7 km from the

fault delineation. The selection of sample points with these distances is to detect the similarity of ground movement while it occurs due to the Grindulu Fault; if the change in the displacement time-series value at the six sample points experiences a LOS deformation direction at the same time, the deformation is indicated as a result of the movement of the Grindulu Fault.

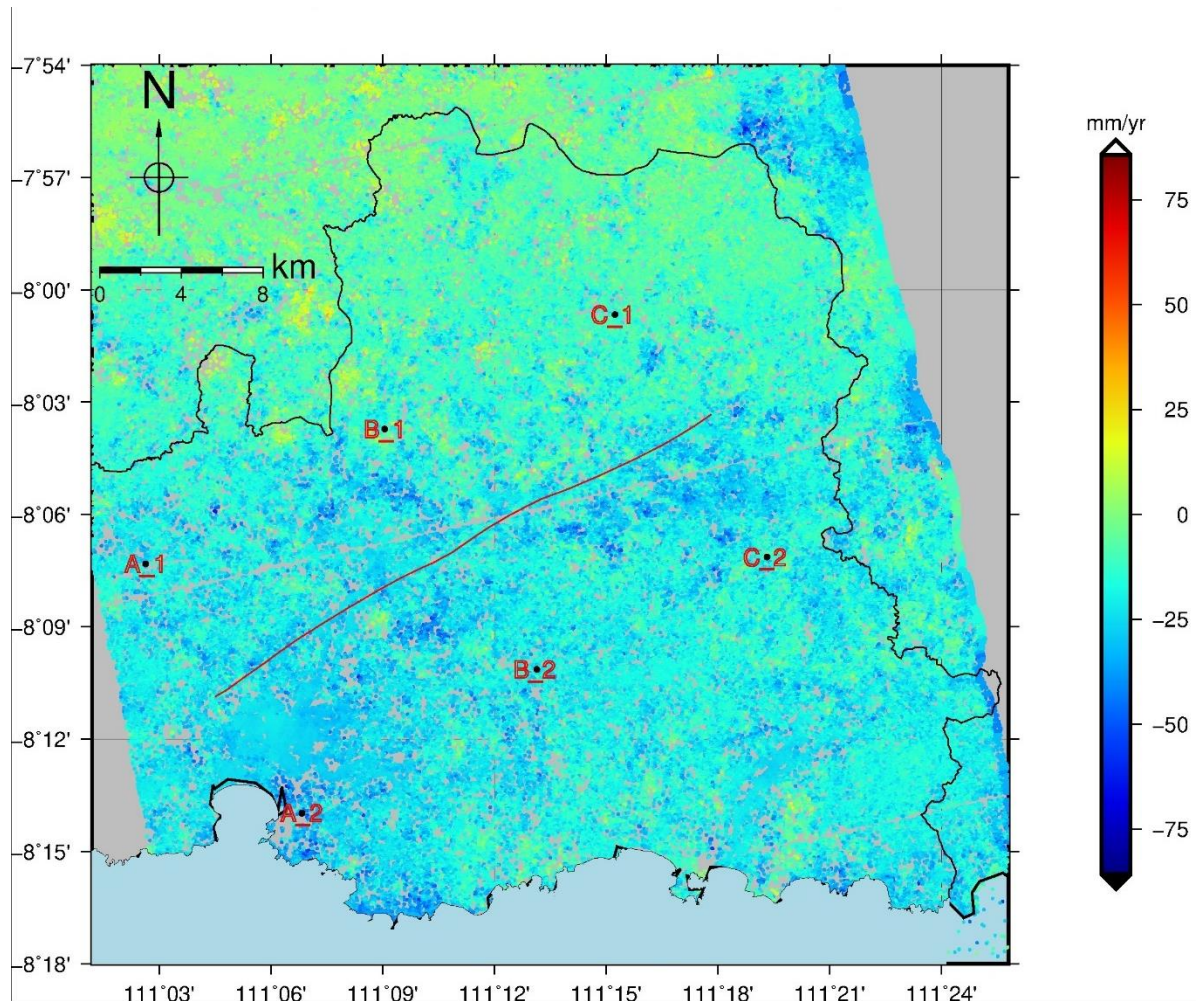


Figure 4.7 Distribution of 6 Sample Points

a. Point in A1 (111° 2'49.50"E – 8° 7'19.50"S)

Point A1 is located around the rice field in Punung Subdistrict. Based on observations from April 2019 to February 2021, the LOS Displacement at point A1 is from -60.5 mm to 79.1 mm and -70.8 mm in LOS cumulative displacement (Figure 4.8a). From the data of 23 displacement time series, a regression analysis was performed to obtain the mean LOS Velocity per year so that the regression equation $y = -3.6069x + 47.748$ was obtained. While the value of the coefficient of determination (R^2) is 0.4075 indicates that 40.75% of the data is represented by the regression model. So, the regression model is very good for describing the trend of land subsidence at point A1. The LOS velocity displacement at point A1 and the results obtained show a subsidence of -43.1 mm/yr (move away from satellite).

b. Point in A2 (111° 6'49.50"E - 8°13'58.50"S)

Point A2 is located around the forest close to the beach in Pacitan Subdistrict. Based on the LOS displacement time series data, at point A2 it shows a LOS displacement value between -53.3 mm and 47.7 mm. At the same time, the LOS velocity of land subsidence at that point is -12.9 mm/yr (Table 4.1). The rate of land subsidence in this region illustrates that the

region around the coast of Pacitan has the potential to experience land subsidence. This area is a tourist area and urban with dominated by alluvial geological formations, so human or fault activities in urban areas are a trigger for land subsidence.

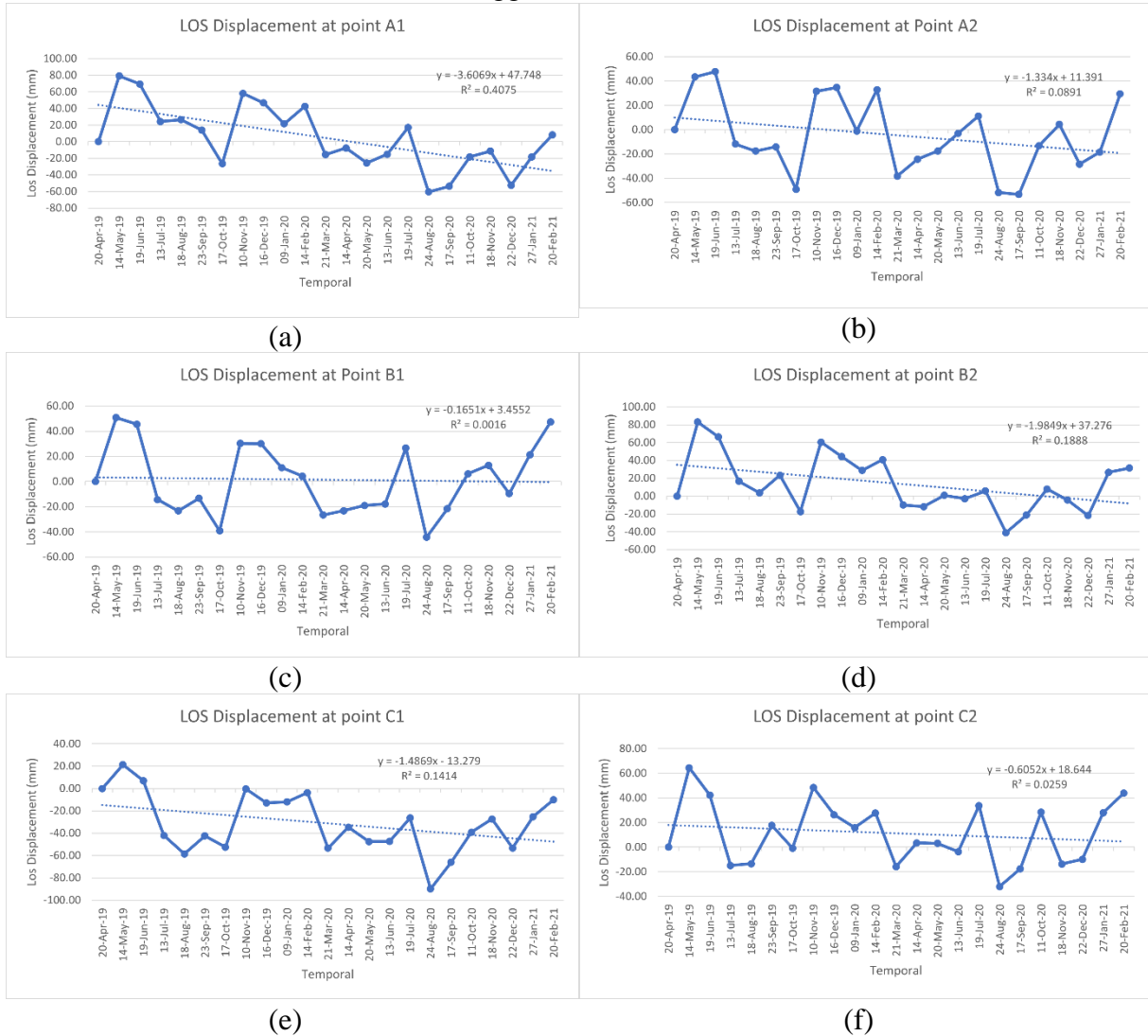


Figure 4.8 Graph LOS displacement

c. Point in B1 (111° 9'9.50"E- 8°3'43.50"S)

The area around the B1 has a high proportion of forest, resulting in a high vegetation density. Therefore, the regression equation is $y = -0.1651x + 3.4552$ and the coefficient of determination (R^2) is 0.0016 indicates that 0.16% of the data is not represented by regression model. The LOS displacement at point B1 is between -44.3 mm and 50.8 mm. Meanwhile, the mean LOS Velocity value at that point is 11.3 mm/yr with -3.3 mm of cumulative LOS displacement based on 23 observations sequentially.

d. Point at B2. (111°13'13.50"E- 8°10'8.50"S)

While At the point B2, the LOS displacement ranged from -41.0 mm to 83.1 mm (Figure 2.1d). The location of these points is near to the forest and rice fields, where the value of the mean LOS velocity in this point is -22.1 mm/yr. This indicates that land subsidence or the earth surface move away from the satellite occurs at that area.

e. Point in C1. (111°15'14.50"E-8° 0'40.50"S)

The range of deformation values at the point in the C1 located in the Bandar sub-district ranges from -89.9 mm to 21.4 mm. After doing the SBAS InSAR processing, the mean LOS

velocity displacement obtained is -16.4 mm/yr.

f. Point in C2. (111°19'18.50"E - 8° 7'8.50"S)

Point C2 is located around the rice field in Tulakan Subdistrict. Based on observations from April 2019 to February 2021, the LOS Displacement at point C2 is from -32.0 mm to 64.4 mm (Figure 4.8f) with a cumulative displacement is -20.4 mm. Based on the LOS displacement time series data from 23 observations, the land subsidence rate was -7.5 mm/yr.

Table 4.1 LOS Displacement in point sample

Acquisition Time	LOS Displacement (mm)					
	A1	A2	B1	B2	C1	C2
April 21, 2019	0.0	0.0	0.0	0.0	0.0	0.0
Mei 15, 2019	79.1	43.4	50.8	83.1	21.4	64.4
June 20, 2019	69.5	47.7	45.6	66.6	7.1	42.2
July 14, 2019	24.2	-11.8	-14.4	16.6	-41.9	-14.8
August 19, 2019	26.6	-17.6	-23.3	3.6	-58.5	-13.5
September 24, 2019	13.9	-14.1	-13.3	23.3	-42.4	17.7
October 18, 2019	-26.6	-49.0	-39.2	-17.5	-52.5	-0.8
November 11, 2019	58.2	31.6	30.3	60.6	-0.3	48.5
December 17, 2019	46.7	34.7	30.1	44.4	-12.9	26.3
January 10, 2020	21.6	-1.1	11.0	28.8	-12.0	15.9
February 15, 2020	42.6	32.9	4.3	40.8	-3.64	27.7
March 22, 2020	-15.5	-38.3	-26.6	-10.0	-53.4	-15.8
April 15, 2020	-7.7	-24.3	-23.3	-11.8	-34.7	3.5
Mei 21, 2020	-25.6	-17.4	-19.1	0.9	-47.6	3.1
June 14, 2020	-14.9	-2.9	-17.9	-2.9	-47.4	-3.7
July 20, 2020	16.9	11.2	26.7	5.8	-26.4	33.7
August 25, 2020	-60.5	-51.8	-44.3	-41.0	-89.9	-32.0
September 18, 2020	-53.7	-53.3	-21.7	-21.3	-65.9	-17.5
October 12, 2020	-18.3	-13.1	6.2	7.8	-39.2	28.4
November 29, 2020	-11.3	4.6	12.9	-4.5	-27.4	-13.7
December 23, 2020	-52.7	-28.3	-9.6	-21.8	-53.3	-9.9
January 28, 2021	-18.4	-18.4	21.2	26.6	-25.2	28.0
February 21, 2021	8.3	29.4	47.5	31.5	-9.9	44.0
Cumulative (mm)	-70.9	-13.9	-3.3	-51.7	-31.3	-20.4
Mean LOS Velocity (mm/yr)	-43.1	-12.9	-2.1	-22.1	-16.4	-7.5
Mean LOS Velocity of Regression Model (mm/yr)	-26.6	-9.8	-1.2	-14.6	-10.9	-4.4

Based on the mean LOS velocity at sample points A1 and C1 tend to experience more significant subsidence. This shows that the area in the northwest (NW) or above the Grindulu fault is moving away from the satellite along the Line of Sight. While points A2, B2, and C2 also experience subsidence but at a slower rate each year. Therefore, the results of SBAS InSAR are still ineffective in determining the direction of deformation due to Grindulu fault activities which is a combination of reserve and normal fault. This occurs because the normal fault mechanism tends to move away from each other, causing the subsidence of one of the fault planes or the formation of a valley, as happened in the Steens Mountains and Alvord Desert faults, Oregon, United States of America. However, based on the time-series pattern, it shows the same pattern at sample points A1-B1 with C1-A2, also in pattern of B2 and C2. This means that the cause of deformation in the area is the same thing, namely the presence of the Grindulu fault. This is supported by the occurrence of shallow earthquakes near the Grindulu fault, which will be discussed in sub chapter 4.4.

4.3 Validation of SBAS-InSAR between GMTSAR and LiCSBAS

Results of SBAS InSAR using GMTSAR will be analyzed and compare to SBAS results using LiCSBAS.

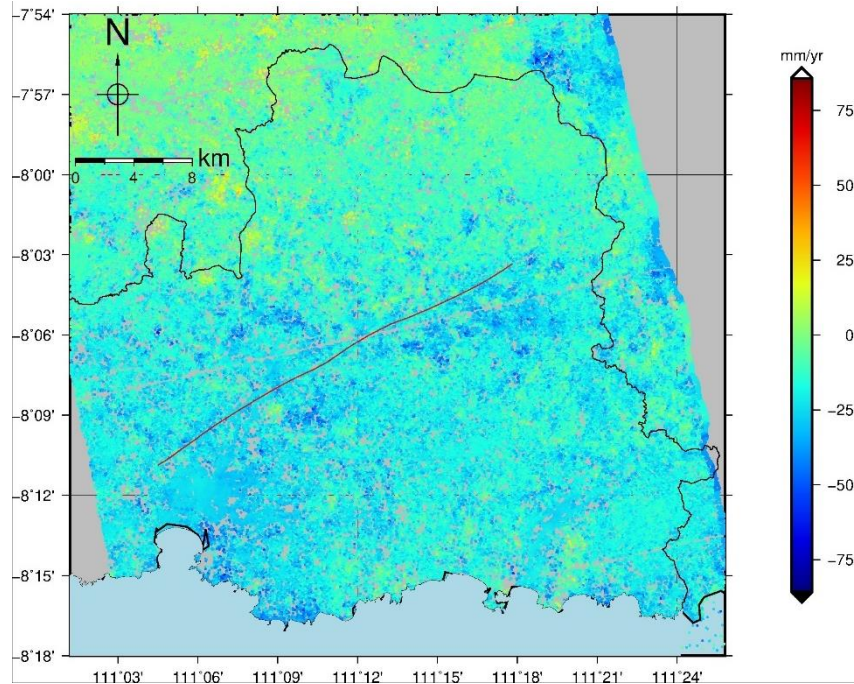


Figure 4.9 Result of SBAS InSAR using GMTSAR

The results using LiCSBAS can be used to map ground deformation along the Line of Sight (LOS) in areas around the Grindulu fault. To obtain the deformation value, Interferometric SAR processing was carried out with the acquisition of Ascending direction data starting in April 2019 to February 2021. Figure 4.10 is the result of LiCSBAS processing that produces the deformation in mean velocity along the Line of Sight (LOS) based on LiCSAR data.

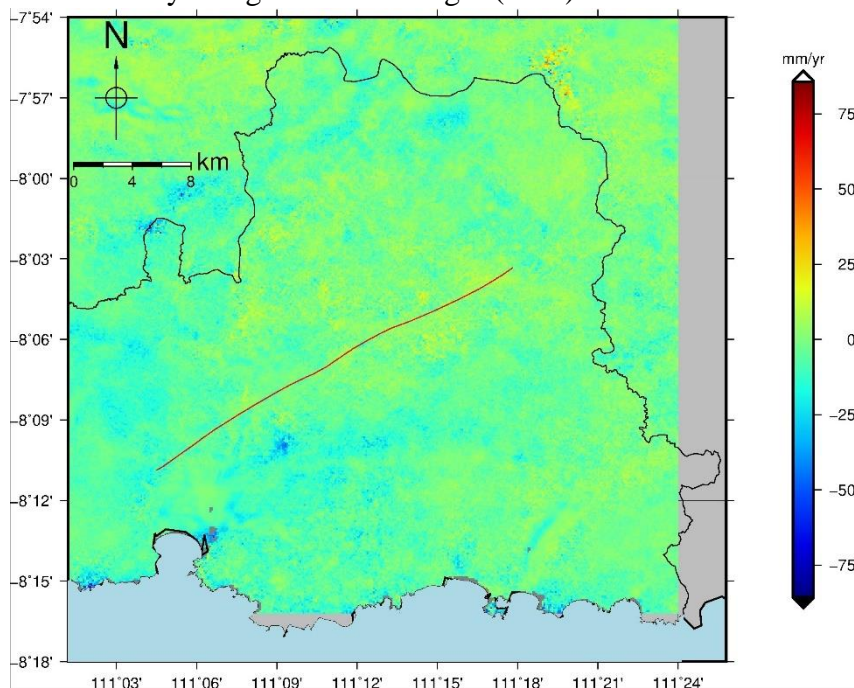


Figure 4.10 Result of SBAS InSAR using LiCSBAS

The GMTSAR result compares using LiCSBAS to see the consistency assessment of the deformation measurements. The standard deviation value at the six sample points processed using GMTSAR obtained a smaller value, 14.34 mm/year, compared to the LiCSBAS standard deviation value of 18.0 mm/year. It shows that the processing of SBAS InSAR using GMTSAR has better accuracy than the results produced using LiCSBAS. While based on the results of RMSE calculation generated from 6 sample points, a value of 13.7 mm/year is obtained. The value shows the mean LOS velocity displacement that generated from SBAS-InSAR using GMTSAR has a big enough difference from the value represented by the results of processing using LiCSBAS. However, visualization of LiCSBAS result also dominated with land subsidence near to the Grindulu fault. So, the LiCSBAS produce reasonable ground deformation results in regions with slow, low rates of displacement and lacking coherence. Comparing the results could represent similar and consistent ground deformation (Figure 4.11).

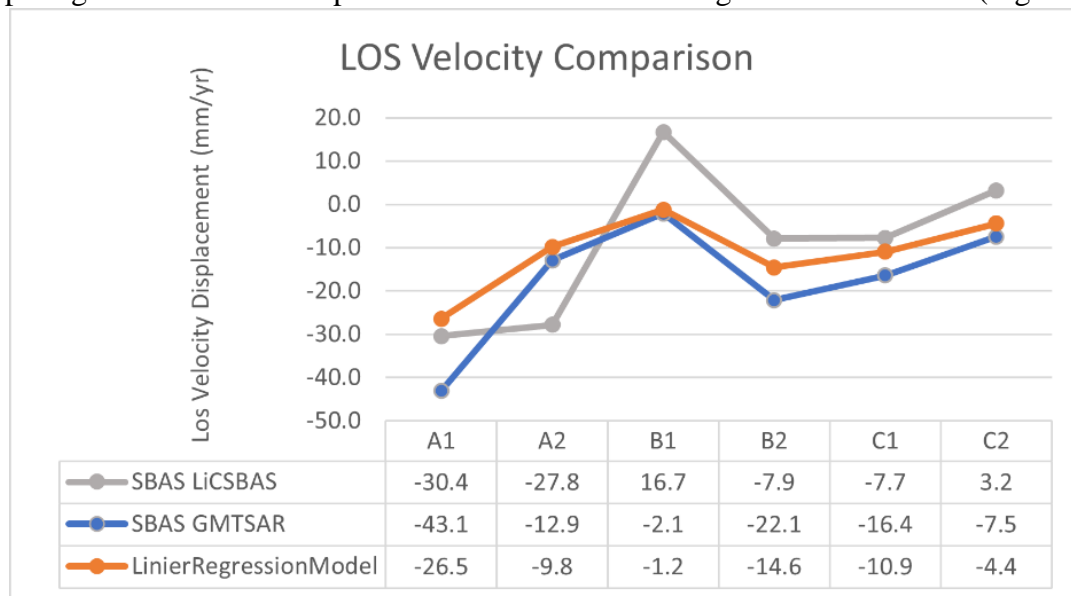


Figure 4.11 Comparison between SBAS InSAR using GMTSAR and LiCSBAS

Several factors can potentially contribute to the difference in the mean Line of Sight (LOS) velocity derived from the processing of Synthetic Aperture Radar (SAR) data using the GMTSAR and LiCSBAS software packages. One factor that has influence is the selection of parameter settings employed in the software, as it has the potential to generate variations in the outcomes of measurements. This encompasses factors such as the coherence threshold, the choice of correction type, and other parameters that impact the processing and analysis of Interferometric Synthetic Aperture Radar (InSAR) data. Moreover, it is essential to note that the two processes utilize different sources of image data. Specifically, GMTSAR relies on SLC Sentinel 1B data, whereas LiCSBAS makes use of images that are accessible on the COMETLiCS website. Variations in the quality and origin of input data can have an impact on the outcomes of data processing. The spatial resolution, quality of atmospheric correction, and cloud cover of SAR data utilized in SBAS InSAR can exhibit variations that have the potential to impact the accuracy of line-of-sight (LOS) velocity measurements. Hence, it is crucial to acknowledge that every InSAR processing software or tool possesses distinct attributes and operational approaches, potentially leading to disparities in measurement outcomes.

4.4 Analysis of Geological and Geomorphology around the Grindulu Fault

Seismic activity in the Pacitan region has been noted on several occasions, mostly because of a result of plate subduction occurring within the Java subduction zone below the Sunda block. The Java megathrust force largely accommodates the main convergence motion, with the minor parallel motion being accommodated along the active Kendeng and Baribis faults, as Santoso et al. (2018) noted. The veracity of this claim is supported by the seismic data that has been recorded in Figure 4.12. The present illustration is an outcome of seismic data visualization related to the close of the Grindulu Fault. The data has been recorded and provided by the Meteorological, Climatological, and Geophysical Agency of Indonesia (BMKG) and can be accessed through the website <https://repogempa.bmkg.go.id/eventcatalog>

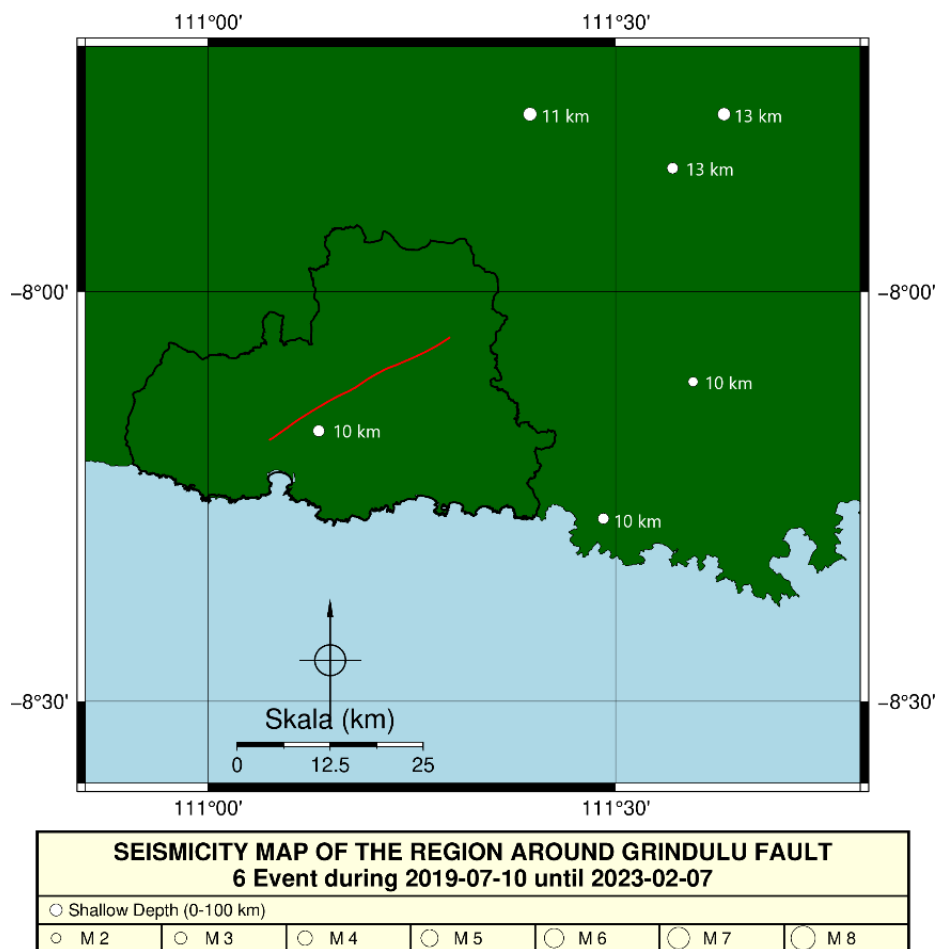


Figure 4.12 Seismicity Map in the research area

Based on recorded events from 2019 to 2021, have been 6 earthquakes located around the study area. As we can see there is one seismic activity near the Grindulu Fault was detected in the November 7, 2019, by Meteorology Climatology and Geophysics Council in Indonesia BMKG. 3.1 Mw earthquake with a depth of 10 kilometers and the epicenter located at 8.170° South Latitude and 111.136° East Longitude. This condition can be an illustration that the area around the Grindulu Fault in East Java is included in the category of areas that are quite active for seismic earthquakes, especially for the Pacitan region in the north and weakens in the south. This shows that the existence of the fault movement is still active in 2019-2021.

The cross profile was carried out with as many as three samples to represent the Eastern, Central and Western parts of the Grindulu Fault, in order to visualize the deformation pattern (Subsidence or uplift) in the area around the fault.

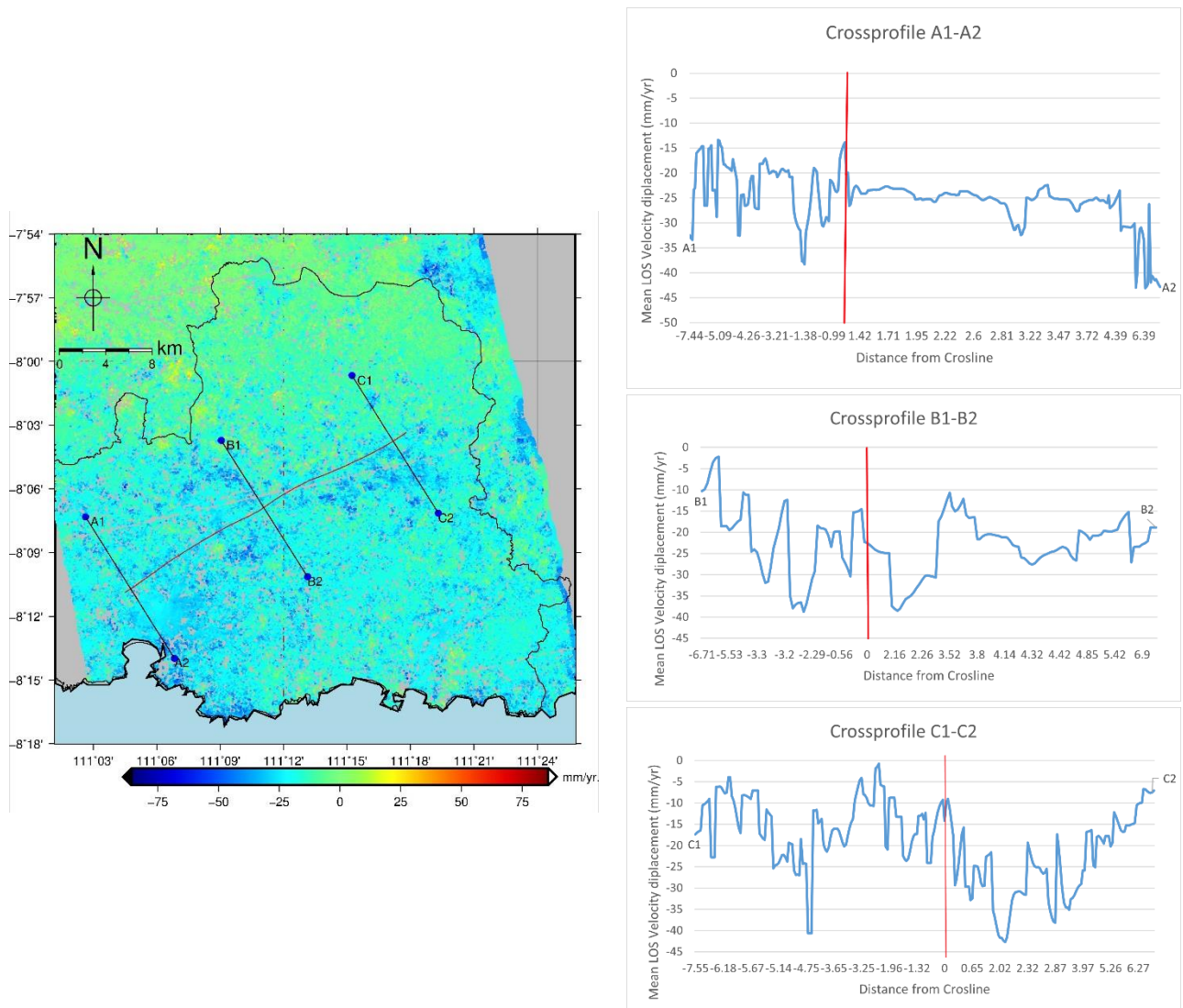


Figure 4.13 The results of the cross-sectional visualization based on the deformation value, (red line is Grindulu fault)

The explanation regarding the analysis of the phenomenon of ground deformation in the area around the fault base on the cross-sectional profile is in the Figure 4.13. The SBAS-InSAR results indicate less detectable ground deformation due to the movement of the Grindulu segment fault. This can be seen in Figure 4.13 that the profile A1-A1 and B1-B2 experience land subsidence. At the same time, C1-C2 profiles illustrate the uplift phenomenon, even close to the grindulu delineation. This various deformation patterns between profiles indicate the influence of other factors. Factors that can influent deformation in the region surrounding the segment, such as the phenomenon of floods and landslides near the Grindulu riverbanks.

The conditions are supported by the presence of Triangular facets or areas that have the potential for landslides as shown in the Figure 4.14. The feature of Triangular facets is the triangular shape which indicates the possibility of landslide activity along the hill valleys of the Grindulu River in the NNE direction (north east). The area is marked with dotted areas (Figure 4.14) which are located in the Arjosari and Tegalombo Subdistrict. It is supported by the topography of Pacitan Regency, which has a flat to mountainous topography, with the highest elevation of 1,200m above sea level, Bandar District and Mount Gembes. The mountainous topography is mainly located in the northern part of the Grindulu, covering Nawangan, Bandar, Tegalombo and Arjosari SubDistrict. Pacitan Regency is dominated by land with hilly topography with a slope of 31 – 50% covering an area of 722.73 km² (52%), with a slope of 11 – 30% covering an area of 333.57 km² (24%). The rest are mountainous areas with a slope of more than 51% (10%), wavy areas with a slope of 6-10% covering an area of 138.99 km² (10%) and plain areas with a slope of 0-5% covering an area of 55.59km² (4%) (Pekab Pacitan, n.d.).

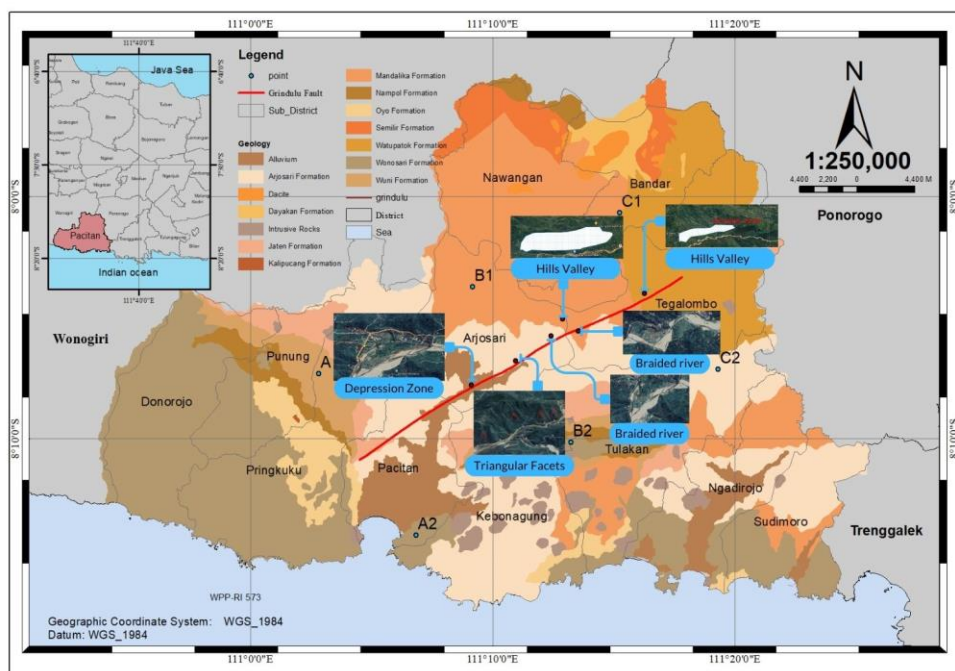


Figure 4.14 Modification of the regional geomorphology and geological map in the study area based on the Pacitan Sheet Regional Geological Map at a scale of 1:250,000

There were also some braided rivers near grindulu fault areas; it can be seen that the river has complex channel patterns with many river channels branching and joining, which indicates of an active fault. This happens because of tectonic movements that cause significant deformation and changes in river topography. The other geomorphologies that can be seen around the grindulu fault are the depression zone or the area that tends to have a lower topography compared to its surroundings, as can be seen in the Arjosari Subdistrict. This geomorphology is caused by a subsidence in the earth's crust that occurs due to fault activity. This is in line with the deformation phenomenon that occurs around grindulu faults, namely subsidence as indicated by the results of SBAS InSAR.

The majority of the research location area traversed by the Grindulu fault is in the Arjosari formation and alluvium sediment layer, where the forming rocks consist of sequences of sandstone, siltstone, limestone and claystone (Figure 4.14). The results of visual observations

show that the low rate of subsidence occurs in points B1 and C2, -2.1 and -7.5 mm/year located in the Mandalika formation. The Mandalika formation form from volcanogenic rock layer with characteristic tend to have a higher level of hardness compared to sedimentary rocks. At the same time, the areas that have high ground deformation values are generally areas close to grindulu riverbanks. Points A2 and B2 are located in the Wonosari formation and are dominated by limestone, which is soft rock and easily scratched. As a result, if an earthquake or other seismic activity occurs around the limestone rock, the deformation will be severe enough. Therefore, the Land Subsidence in points A2 and B2 have a large enough value of deformation, -12.90 and -22.11 mm/year. It is in line with the area around the river, which has a relatively soft rock structure and a thick layer of sediment (Sugianto, 2016). The experience of deformation is higher than in the areas that have relatively hard surface soil layers.

"This page was deliberately blanked."

CHAPTER 5

CONCLUSION AND SUGGESTION

5.1 Conclusion

Based on research about deformation analysis around Grindulu Fault using the SBAS InSAR technique, there are several conclusions, namely as follows:

1. Based on the results, The SBAS method utilized in this study is beneficial for detecting the ground deformation phenomenon around the Grindulu Fault. The results of SBAS InSAR show the greater subsidence occurs in northwest or above the Grindulu fault with mean LOS velocity displacement, -2.1 until -43.1 mm/yr. This occurs because the normal fault mechanism tends to move away from each other. However, the SBAS result detects that the subsidence occurs in almost areas around Grindulu.
2. The time-series pattern shows almost the same pattern at sample points A1- B1 -C1 and A2- B2- C2, which means that the cause of deformation in the area is the same thing, the existing Grindulu fault. It is supported by the shallow earthquakes that occur near the Grindulu fault and some geomorphology conditions such Triangular facets, braided rivers, and depression zone near Grindulu fault. The areas that have high ground deformation values are generally areas that have a relatively soft alluvial structure and a thick layer of sediment. In contrast, another ground deformation values are identified in the regions that have relatively hard surface soil layers. Moreover, the deformation value between SBASInSAR results generated using GMTSAR and LiCSBAS has close similar subsidence visualization, even the RMSE value obtained 13.7 mm/yr. It demonstrates that the SBASInSAR velocity generated by GMTSAR processing not enough corresponds to the LiCSBAS.

5.2 Suggestion

Based on research about deformation analysis Grindulu Fault the SBAS InSAR technique, there are several suggestions for further research, namely as follows:

1. It is recommended to use troposphere correction using GACOS data to reduce the effect of atmospheric phase screens on SBAS InSAR results.
2. For further research, other methods or techniques can be used in analyzing deformations such as GPS or gravity anomaly.

"This page was deliberately blanked."

REFERENCES

- Abidin, H. Z., Andreas, H., Meilano, I., Gamal, M., Gumilar, I., & Abdullah, C. I. (2009). *Deformasi Koseismik dan Pascaseismik Gempa Yogyakarta 2006 dari Hasil Survei GPS*.
- Ayani, R. H., Ching, K. E., Anjasmara, I. M., & Lin, Y. N. (2021). Crustal Deformation of the Kendeng Fault Branches Area from GNSS and InSAR Data in Surabaya City, Indonesia. *IOP Conference Series: Earth and Environmental Science*, 936(1). <https://doi.org/10.1088/1755-1315/936/1/012019>
- Berardino, P., Fornaro, G., Lanari, R., & Sansosti, E. (2002). A new algorithm for surface deformation monitoring based on small baseline differential SAR interferograms. *IEEE Transactions on Geoscience and Remote Sensing*, 40(11), 2375–2383. <https://doi.org/10.1109/TGRS.2002.803792>
- BMKG. (2023). *Earthquake Events Request*. Badan Meteorologi, Klimatologi Dan Geofisika. <https://repogempa.bmkg.go.id/eventcatalog>
- BPS. (2020). Kabupaten Pacitan Dalam Angka. In *Bps* (Issue 8).
- Burgmann, R., Rosen, P. A., & Fielding, E. J. (2000). Synthetic aperture radar interferometry to measure earth's surface topography and its deformation. *Annual Review of Earth and Planetary Sciences*, 28, 169–209. <https://doi.org/10.1146/annurev.earth.28.1.169>
- Caesardi, M. A. (2018). Estimasi Kecepatan Gelombang Geser (Vs) Melalui Inversi Kurva Horizontal to Vertical Spectrum Ratio Pada Jalur Sesar Grindulu. *Departemen Fisika ITS*.
- Chai, T., & Draxler, R. R. (2014). Root mean square error (RMSE) or mean absolute error (MAE)? -Arguments against avoiding RMSE in the literature. *Geoscientific Model Development*, 7(3). <https://doi.org/10.5194/gmd-7-1247-2014>
- Champenais, J., Fruneau, B., Pathier, E., Deffontaines, B., Lin, K. C., & Hu, J. C. (2012). Monitoring of active tectonic deformations in the Longitudinal Valley (Eastern Taiwan) using Persistent Scatterer InSAR method with ALOS PALSAR data. *Earth and Planetary Science Letters*, 337–338, 144–155. <https://doi.org/10.1016/j.epsl.2012.05.025>
- Cholifah, L., Mufidah, N., Lazuardi, E., Santosa, B. J., Sungkono, S., & Haryono, A. (2020). Identification of the Grindulu Fault in Pacitan, East Java using Magnetic Method. *Jurnal Penelitian Fisika Dan Aplikasinya (JPFA)*, 10(1), 22. <https://doi.org/10.26740/jpfa.v10n1.p22-33>
- Çomut, F. C., Üstün, A., Canaslan, F., & Ustun, A. (2012). *Impact of Perpendicular and Temporal Baseline Characteristics on InSAR Coherence Maps*. <https://www.researchgate.net/publication/277612439>
- Dewanto, B. G., Setiawan, M. B., & Nusantara, G. C. (2020). *Opak Fault Deformation Monitoring Using Sentinel-1 Insar Data From 2016-2019 In Yogyakarta Indonesia*.

- Elias, P., Briole, P., Elias, P., & Briole, P. (2018). *Through the Means of SAR Multitemporal Interferometry. Geochemistry, Geophysics, Geosystems*. 19(12), 4836–4857. <https://doi.org/10.1029/2018GFC007574>
- ESDM. (2023). *Peta Geologi Lembar Pacitan, Jawa*. GeoMap.
- Ferretti, A. , Monti-guarnieri, A. , Prati, C. , & Rocca, F. (2007). *InSAR Principles: Guidelines for SAR Interferometry Processing and Interpretation*. ESA Publications ESTEC.
- Flores-Anderson, A. I. , Herndon, K. E. , Thapa, R. B. , & Cherrington, E. (2018). *The Sar Handbook: Comprehensive Methodologies for Forest Monitoring and Biomass Estimation*. <https://doi.org/10.25966/nr2c-s697>
- Ghilani, C. D. (2017). Adjustment Computations. In *Adjustment Computations*. <https://doi.org/10.1002/9781119390664>
- Girty. (2009). Understanding Processes Behind Natural Disasters. *Department of Geological Sciences, San Diego State University*.
- Gultaf, H. (2014). Analisa Kinematika Sesar Grindulu di Daerah Pacitan dan Sekitarnya. *ITB*.
- Gümgümcü, H., Schindler, K., Dirk, J., Andrés, W., & Escallón, R. (2018). *Detecting deforestation using Sentinel-1 SAR data and deep learning Institute of Geodesy and Photogrammetry ETH Zurich*.
- Hamad, H., & Fadlil, Moh. (2021). Identifikasi Deformasi Pulau Bali Berdasarkan Rekaman Data GPS, Menggunakan Software GAMIT. *Jurnal Sains Dan Teknologi Tadulako*.
- Hayati, N., Widodo, A., Kurniawan, A., Sanjiwani, I. D. M. A., Darminto, M. R., Yudha, I. S., & Sumantyo, J. T. S. (2022). Small baselines techniques of time series InSAR to monitor and predict land subsidence causing flood vulnerability in Sidoarjo, Indonesia. *Geomatics, Natural Hazards and Risk*, 13(1), 2124–2150. <https://doi.org/10.1080/19475705.2022.2109518>
- Hidayat, E., Yugo, K., Puguh, D. R., & Eko, P. (2012). *Kajian Tektonik Aktif Pada Patahan Grindulu Untuk Mendukung Mitigasi Bencana Gempabumi dan Gerakan Tanah di Wilayah Pacitan*.
- Hu, L., Dai, K., Xing, C., Li, Z., Tomás, R., Clark, B., Shi, X., Chen, M., Zhang, R., Qiu, Q., & Lu, Y. (2019). Land subsidence in Beijing and its relationship with geological faults revealed by Sentinel-1 InSAR observations. *International Journal of Applied Earth Observation and Geoinformation*, 82. <https://doi.org/10.1016/j.jag.2019.05.019>
- Ichsandya, D. B., Dimyati, M., Shidiq, I. P. A., Zulkarnain, F., Rahatiningtyas, N. S., Syamsuddin, R. P., & Zein, F. M. (2022). Landslide assessment using interferometric synthetic aperture radar in Pacitan, East Java. *International Journal of Electrical and Computer Engineering*, 12(3), 2614–2625. <https://doi.org/10.11591/ijece.v12i3.pp2614-2625>

- Lanari, R., Casu, F., Manzo, M., & Lundgren, P. (2007). Application of the SBAS-DInSAR technique to fault creep: A case study of the Hayward fault, California. *Remote Sensing of Environment*, 109(1), 20–28. <https://doi.org/10.1016/j.rse.2006.12.003>
- Lazecký, M., Spaans, K., González, P. J., Maghsoudi, Y., Morishita, Y., Albino, F., Elliott, J., Greenall, N., Hatton, E., Hooper, A., Juncu, D., McDougall, A., Walters, R. J., Watson, C. S., Weiss, J. R., & Wright, T. J. (2020). LiCSAR: An automatic InSAR tool for measuring and monitoring tectonic and volcanic activity. *Remote Sensing*, 12(15). <https://doi.org/10.3390/RS12152430>
- Li, S., Xu, W., & Li, Z. (2022). Review of the SBAS InSAR Time-series algorithms, applications, and challenges. *Geodesy and Geodynamics*, 13(2), 114–126. <https://doi.org/10.1016/j.geog.2021.09.007>
- Morishita, Y., Lazecky, M., Wright, T. J., Weiss, J. R., Elliott, J. R., & Hooper, A. (2020). LiCSBAS: An open-source insar time series analysis package integrated with the LiCSAR automated sentinel-1 InSAR processor. *Remote Sensing*, 12(3). <https://doi.org/10.3390/rs12030424>
- Noor, D. (2009). Pengantar Geologi Edisi Pertama. In *Transformator*.
- Noor, D. (2014). *GEOMORFOLOGI*.
- Parera, A. F. T., Bunaga, I. G. K. S., & Yusuf, M. (2015). Pemodelan Tiga Dimensi Anomali Gravitasi Dan Identifikasi Sesar Lokal Dalam Pementuan Jenis Sesar Di Daerah Pacitan. *Prosiding Seminar Nasional Fisika*, 7.
- Pemkab Pacitan. (n.d.). *Geografis Pacitan*. Retrieved February 20, 2023, from <https://pacitankab.go.id/geografis/>
- Qiu, J., Liu, L., Wang, C., & Wang, Y. (2019). Present-day tectonic activity along the central section of the Altyn Tagh fault derived from time series InSAR. *Geodesy and Geodynamics*, 10(4), 307–314. <https://doi.org/10.1016/j.geog.2019.03.008>
- Rasimeng, S., Karyanto, K., Mulyatno, B. S., & Azhari, M. F. (2020). *Analisis Deformasi Permukaan Menggunakan Metode DInSAR (Differential Interferometry Synthetic Aperture Radar) Pada Studi Kasus Gempabumi Lombok Periode Agustus 2018*. <https://doi.org/https://doi.org/10.23960/jge.v6i2.68>
- Rusydy, I., Idris, Y., Mulkal, Muksin, U., Cummins, P., Akram, M. N., & Syamsidik. (2020). Shallow crustal earthquake models, damage, and loss predictions in Banda Aceh, Indonesia. *Geoenvironmental Disasters*, 7(1). <https://doi.org/10.1186/s40677-020-0145-5>
- Samodra, H., Gafoer, S., & Tjokrosapoetra, S. (1992). *Geologi Lembar Pacitan*.
- Sandwell, D., Mellors, R., Tong, X., Xu, X., Wei, M., & Wessel, P. (2011). *GMTSAR: An InSAR Processing System Based on Generic Mapping Tools (Second Edition)*.
- Sumantyo, S., Josaphat, T., Shimada, M., Mathieu, P. P., & Abidin, H. Z. (2012). Long-term consecutive DInSAR for volume change estimation of Land deformation. *IEEE*

Transactions on Geoscience and Remote Sensing, 50(1).
<https://doi.org/10.1109/TGRS.2011.2160455>

- Supendi, P., Nugraha, A. D., Puspito, N. T., Widiyantoro, S., & Daryono, D. (2018). Identification of active faults in West Java, Indonesia, based on earthquake hypocenter determination, relocation, and focal mechanism analysis. *Geoscience Letters*, 5(1). <https://doi.org/10.1186/s40562-018-0130-y>
- Syahputri, B. E. A., Anjasmara, I. M., & Hayati, N. (2023). Investigation of Ground Deformation around The Segments of Kendeng Fault in East Java 2017-2020 using Multi-Temporal InSAR Analysis with GACOS Correction Product. *IOP Conference Series: Earth and Environmental Science*, 1127(1). <https://doi.org/10.1088/1755-1315/1127/1/012007>
- Udías, A. , Vallina, A. U. , Madariaga, R. , & Buforn, E. (2014). *Source Mechanisms of Earthquakes Theory and Practice*.
- Ulma, T. (2020). Analisis Deformasi Kota Surabaya Tahun 2017-2019 Akibat Aktivitas Sesar Kendeng Dengan Metode Permanent Scatterers Interferometry Synthetic Aperture Radar (Ps-Insar) Dan Validasi Data Gps. *Repository ITS*. <https://repository.its.ac.id/87667/>
- Wallance, R., Allen, C., & Brown, L. (1986). Active Tectonics: Impact on Society (1986). In *Active Tectonics*. National Academies Press. <https://doi.org/10.17226/624>
- Wessel, P., Luis, J. F., Uieda, L., Scharroo, R., Wobbe, F., Smith, W. H. F., & Tian, D. (2019). The Generic Mapping Tools Version 6. *Geochemistry, Geophysics, Geosystems*, 20(11), 5556–5564. <https://doi.org/10.1029/2019GC008515>
- Willmott, C. J., & Matsuura, K. (2005). Advantages of the mean absolute error (MAE) over the root mean square error (RMSE) in assessing average model performance. *Climate Research*, 30(1). <https://doi.org/10.3354/cr030079>
- Yulta, S. A., Anjasmara, I., & Taufik, M. (2018). *Aplikasi Metode SBAS-DInSAR Menggunakan Data Sentinel-1A Untuk Pengamatan Penurunan Muka Tanah Di Kota Surabaya*.
- Yusvinda, M. N., Puspitasari, S. W., Wafi, N. M. P., Aziz, K. N., Darmawan, D., Katriani, L., Handayani, N. T., & Wibowo, N. B. (2021). *Structure Interpretation Using Gravity Spectral Analysis and Derivative Method in Grindulu Fault, Pacitan, East Java*.
- Zebker, H., & Chen, C. (2002). Phase Unwrapping for Large SAR Interferograms: Statistical Segmentation and Generalized Network Models. *IEEE Transactions on Geoscience and Remote Sensing*, 40(8), 1709–1719.
- Zikri, K. (2018). *Geologi Umum*. GEOGRAFI UNP.

APPENDIX

1. BATCH_TOPS.CONFIG

```
# This is an example configuration file for batch processing
# all the comments or explanations are marked by "#"
# The parameters in this configuration file is distinguished by their first word so
# user should follow the naming of each parameter.
# the parameter name, = sign, parameter value should be separated by space " ".
# leave the parameter value blank if using default value.
#
#####
# processing stage for intf_batch.csh #
#####
# 1 - start from make topo_ra
# 2 - start from make and filter interferograms, unwrap and geocode
proc_stage = 1
# the namestem of the master image - REQUIRED
master_image = S1_20190421_ALL_F2
#####
# parameters for preprocess      #
# - pre_proc_batch.csh          #
# following 4 parameters are OPTIONAL #
#####
# num of patches
num_patches =
# earth radius
earth_radius =
# near_range
near_range =
# Doppler centroid
fd1 =
#####
# parameters for make topo_ra  #
# - dem2topo_ra.csh           #
#####
# subtract topo_ra from the phase
# (1 -- yes; 0 -- no)
topo_phase = 1
# if above parameter = 1 then one should have put DEM.grd in topo/
# topo_ra shift (1 -- yes; 0 -- no)
shift_topo = 0
#####
# parameters for make and filter interferograms #
# - intf.csh                                  #
# - filter.csh                                 #
#####
# filters
# look at the filter/ folder to choose other filters
filter_wavelength = 100
```

```

# decimation of images
# decimation control the size of the amplitude and phase images. It is either 1 or 2.
# Set the decimation to be 1 if you want higher resolution images.
# Set the decimation to be 2 if you want images with smaller file size.
#
dec_factor = 2
# for tops processing, to force the decimation factor
# recommended range decimation to be 8, azimuth decimation to be 2
range_dec = 8
azimuth_dec = 2
#####
# parameters for unwrap phase      #
# - snaphu.csh                      #
#####
# correlation threshold for snaphu.csh (0~1)
# set it to be 0 to skip unwrapping.
threshold_snaphu = 0.2
# interpolate masked or low coherence pixels with their nearest neighbors, 1 means
interpolate,
# others or blank means using original phase, see snaphu.csh and snaphu_interp.csh for
details
# this could be very slow in case a large blank area exist
near_interp = 1
# region to unwrap in radar coordinates (leave it blank if unwrap the whole region)
# example format 500/10800/500/27200 - OPTIONAL
region_cut =
# use landmask (1 -- yes; else -- no)
switch_land = 0
#
# Allow phase discontinuity in unwrapped phase. This is needed for interferograms having
sharp phase jumps.
# defo_max = 0 - used for smooth unwrapped phase such as interseismic deformation
# defo_max = 65 - will allow a phase jump of 65 cycles or 1.82 m of deformation at C-band
#
defomax = 0
#####
# parameters for geocode          #
# - geocode.csh                   #
#####
# correlation threshold for geocode.csh (0~1)
threshold_geocode = .1

```


2. PREP_SBAS.CSH

```
#!/bin/csh -f
#   $Id$
# Prepare the input tables for sbas processing
# Xiaohua(Eric) Xu, Jan 25 2016
#
if ($#argv != 5) then
  echo ""
  echo "Usage: prep_sbas.csh intf.in baseline_table.dat file_path phase_name corr_name"
  echo ""
  echo " Example: prep_sbas.csh intf.in baseline_table.dat ../merge corrected/unwrap.grd
corr.grd"
  echo ""
  echo " outputs: "
  echo "  intf.tab scene.tab"
  echo ""
  echo " Command to run sbas will be echoed"
  echo ""
  exit 1
endif
set file = $1
set table = $2
set file_path = $3
set phase_file = $4
set corr_file = $5
rm intf.tab scene.tab
set ni = "0"
set ns = "0"
foreach line (`awk '{print $0}' $1`)
  set ref = `echo $line | awk -F: '{print $1}`
  set rep = `echo $line | awk -F: '{print $2}`
  set ref_id = `grep $ref $table | awk '{printf("%d",int($2))}`
  set rep_id = `grep $rep $table | awk '{printf("%d",int($2))}`
  echo $ref_id $rep_id
  set b1 = `grep $ref $table | awk '{print $5}`
  set b2 = `grep $rep $table | awk '{print $5}`
  set bp = `echo $b1 $b2 | awk '{print ($2-$1)}`
  echo
  echo $file_path"/"$ref_id"_"$rep_id"/"$phase_file
$file_path"/"$ref_id"_"$rep_id"/"$corr_file $ref_id $rep_id $bp >> intf.tab
  set ntmp = `echo $ni`
  set ni = `echo $ntmp | awk '{print ($1+1)}`
end
foreach line (`awk '{print $1":"$2":"$3":"$4":"$5}' < $table`)
  set sc = `echo $line | awk -F: '{print $1}`
  set sc_id = `echo $line | awk -F: '{printf "%d", int($2)}`
  set dy = `echo $line | awk -F: '{print $3}`
  echo "$sc_id $dy" >> scene.tab
  set ntmp = `echo $ns`
  set ns = `echo $ntmp | awk '{print ($1+1)}`
end
set xdim = `gmt grdinfo -C $file_path"/"$ref_id"_"$rep_id"/"$phase_file | awk '{print
$10}`
set ydim = `gmt grdinfo -C $file_path"/"$ref_id"_"$rep_id"/"$phase_file | awk '{print
$11}`
```

3. DATA.IN

```
s1b-iw2-slc-vv-20190421t105715-20190421t105743-015903-01de11-
002:S1B_OPER_AUX_POEORB_OPOD_20210302T042611_V20190420T225942_20190422
T005942.EOF
s1b-iw2-slc-vv-20190515t105716-20190515t105744-016253-01e975-
002:S1B_OPER_AUX_POEORB_OPOD_20210302T135229_V20190514T225942_20190516
T005942.EOF
.
.
.
.
.
.
s1b-iw2-slc-vv-20201223t105728-20201223t105756-024828-02f43e-
002:S1B_OPER_AUX_POEORB_OPOD_20210318T173911_V20201222T225942_20201224
T005942.EOF
s1b-iw2-slc-vv-20210128t105727-20210128t105755-025353-03050a-
002:S1B_OPER_AUX_POEORB_OPOD_20210217T111751_V20210127T225942_20210129
T005942.EOF
s1b-iw2-slc-vv-20210221t105726-20210221t105754-025703-03106f-
002:S1B_OPER_AUX_POEORB_OPOD_20210313T112333_V20210220T225942_20210222
T005942.EOF
```

4. BASELINE_TABLE.DAT

```
S1_20190421_ALL_F2 2019110.4564336562 1935 0.000000000000 0.000000000000
S1_20190515_ALL_F2 2019134.4564454891 1959 37.951368891067 71.776378092198
S1_20190620_ALL_F2 2019170.4564691186 1995 28.656873599283 62.342248749015
S1_20190714_ALL_F2 2019194.4564852782 2019 29.276314914062 47.683374667089
S1_20190819_ALL_F2 2019230.4565113566 2055 29.079864225790 45.044153069350
S1_20190924_ALL_F2 2019266.4565297349 2091 29.012604133862 21.504834544776
S1_20191018_ALL_F2 2019290.4565337389 2115 45.125745162440 40.417586720000
S1_20191111_ALL_F2 2019314.4565322122 2139 66.536579395313 73.036236425666
S1_20191217_ALL_F2 2019350.4565186065 2175 35.195432941696 32.882366598933
S1_20200110_ALL_F2 2020009.4565061852 2199 43.337951720864 47.018190671212
S1_20200215_ALL_F2 2020045.4564941211 2235 44.325241666509 67.449509144905
S1_20200322_ALL_F2 2020081.4564946082 2271 -15.434086042763 32.173146272179
S1_20200415_ALL_F2 2020105.4565031733 2295 43.428259986727 67.743877518492
S1_20200521_ALL_F2 2020141.4565219870 2331 83.754885241369 109.666857833252
S1_20200614_ALL_F2 2020165.4565406737 2355 49.293189814401 73.036718200093
S1_20200720_ALL_F2 2020201.4565634725 2391 64.645830609895 94.607449964469
S1_20200825_ALL_F2 2020237.4565899856 2427 -3.425257846595 19.225051705678
S1_20200918_ALL_F2 2020261.4566002993 2451 54.829855810258 59.907735296748
S1_20201012_ALL_F2 2020285.4566058384 2475 58.080824699345 66.352102044464
S1_20201129_ALL_F2 2020333.4565986083 2523 59.171982849362 69.559152557144
S1_20201223_ALL_F2 2020357.4565846366 2547 120.807345854182 135.975977452230
S1_20210128_ALL_F2 2021027.4565686577 2582 18.845083286596 8.014662033456
S1_20210221_ALL_F2 2021051.4565608962 2606 67.965116329957 98.501554263693
```

5. INTF.IN

S1_20200415_ALL_F2:S1_20200521_ALL_F2	S1_20200110_ALL_F2:S1_20200215_ALL_F2
S1_20200415_ALL_F2:S1_20200614_ALL_F2	S1_20200110_ALL_F2:S1_20200322_ALL_F2
S1_20190421_ALL_F2:S1_20190515_ALL_F2	S1_20200215_ALL_F2:S1_20200415_ALL_F2
S1_20190421_ALL_F2:S1_20190620_ALL_F2	S1_20200215_ALL_F2:S1_20200322_ALL_F2
S1_20190421_ALL_F2:S1_20190714_ALL_F2	S1_20200322_ALL_F2:S1_20200415_ALL_F2
S1_20190515_ALL_F2:S1_20190620_ALL_F2	S1_20200322_ALL_F2:S1_20200521_ALL_F2
S1_20190515_ALL_F2:S1_20190714_ALL_F2	S1_20200322_ALL_F2:S1_20200614_ALL_F2
S1_20190620_ALL_F2:S1_20190714_ALL_F2	S1_20200521_ALL_F2:S1_20200614_ALL_F2
S1_20190620_ALL_F2:S1_20190819_ALL_F2	S1_20200521_ALL_F2:S1_20200720_ALL_F2
S1_20190714_ALL_F2:S1_20190819_ALL_F2	S1_20200614_ALL_F2:S1_20200720_ALL_F2
S1_20190714_ALL_F2:S1_20190924_ALL_F2	S1_20200614_ALL_F2:S1_20200825_ALL_F2
S1_20190819_ALL_F2:S1_20190924_ALL_F2	S1_20200720_ALL_F2:S1_20200825_ALL_F2
S1_20190819_ALL_F2:S1_20191018_ALL_F2	S1_20200720_ALL_F2:S1_20200918_ALL_F2
S1_20190819_ALL_F2:S1_20191111_ALL_F2	S1_20200720_ALL_F2:S1_2021012_ALL_F2
S1_20190924_ALL_F2:S1_20191018_ALL_F2	S1_20200825_ALL_F2:S1_20200918_ALL_F2
S1_20190924_ALL_F2:S1_20191111_ALL_F2	S1_20200825_ALL_F2:S1_2021012_ALL_F2
S1_20190924_ALL_F2:S1_20191217_ALL_F2	S1_20200918_ALL_F2:S1_2021012_ALL_F2
S1_20191018_ALL_F2:S1_20191111_ALL_F2	S1_20200918_ALL_F2:S1_2021129_ALL_F2
S1_20191018_ALL_F2:S1_20191217_ALL_F2	S1_2021012_ALL_F2:S1_2021129_ALL_F2
S1_20191018_ALL_F2:S1_20200110_ALL_F2	S1_2021012_ALL_F2:S1_2021223_ALL_F2
S1_20191111_ALL_F2:S1_20191217_ALL_F2	S1_2021129_ALL_F2:S1_2021223_ALL_F2
S1_20191111_ALL_F2:S1_20200110_ALL_F2	S1_2021129_ALL_F2:S1_20210128_ALL_F2
S1_20191217_ALL_F2:S1_20200110_ALL_F2	S1_2021129_ALL_F2:S1_20210221_ALL_F2
S1_20191217_ALL_F2:S1_20200215_ALL_F2	S1_2021223_ALL_F2:S1_20210128_ALL_F2
	S1_2021223_ALL_F2:S1_20210221_ALL_F2
	S1_20210128_ALL_F2:S1_20210221_ALL_F2

6. SCENE.TAB

2020105 2295
2019110 1935
2019134 1959
2019170 1995
2019194 2019
2019230 2055
2019266 2091
2019290 2115
2019314 2139
2019350 2175
2020009 2199
2020045 2235
2020081 2271
2020141 2331
2020165 2355
2020201 2391
2020237 2427
2020261 2451
2020285 2475
2020333 2523
2020357 2547
2021027 2582
2021051 2606

7. INTF.TAB

```

../intf_all/2019110_2019134/unwrap.grd ../intf_all/2019110_2019134/corr.grd 2019110 2019134 71.7764
../intf_all/2019110_2019170/unwrap.grd ../intf_all/2019110_2019170/corr.grd 2019110 2019170 62.3422
../intf_all/2019110_2019194/unwrap.grd ../intf_all/2019110_2019194/corr.grd 2019110 2019194 47.6834
../intf_all/2019134_2019170/unwrap.grd ../intf_all/2019134_2019170/corr.grd 2019134 2019170 -9.43413
../intf_all/2019134_2019194/unwrap.grd ../intf_all/2019134_2019194/corr.grd 2019134 2019194 -24.093
../intf_all/2019170_2019194/unwrap.grd ../intf_all/2019170_2019194/corr.grd 2019170 2019194 -14.6589
../intf_all/2019170_2019230/unwrap.grd ../intf_all/2019170_2019230/corr.grd 2019170 2019230 -17.2981
../intf_all/2019194_2019230/unwrap.grd ../intf_all/2019194_2019230/corr.grd 2019194 2019230 -2.63922
../intf_all/2019194_2019266/unwrap.grd ../intf_all/2019194_2019266/corr.grd 2019194 2019266 -26.1785
../intf_all/2019230_2019266/unwrap.grd ../intf_all/2019230_2019266/corr.grd 2019230 2019266 -23.5393
../intf_all/2019230_2019290/unwrap.grd ../intf_all/2019230_2019290/corr.grd 2019230 2019290 -4.62657
../intf_all/2019230_2019314/unwrap.grd ../intf_all/2019230_2019314/corr.grd 2019230 2019314 27.9921
../intf_all/2019266_2019290/unwrap.grd ../intf_all/2019266_2019290/corr.grd 2019266 2019290 18.9128
../intf_all/2019266_2019314/unwrap.grd ../intf_all/2019266_2019314/corr.grd 2019266 2019314 51.5314
../intf_all/2019266_2019350/unwrap.grd ../intf_all/2019266_2019350/corr.grd 2019266 2019350 11.3775
../intf_all/2019290_2019314/unwrap.grd ../intf_all/2019290_2019314/corr.grd 2019290 2019314 32.6186
../intf_all/2019290_2019350/unwrap.grd ../intf_all/2019290_2019350/corr.grd 2019290 2019350 -7.53522
../intf_all/2019290_2020009/unwrap.grd ../intf_all/2019290_2020009/corr.grd 2019290 2020009 6.6006
../intf_all/2019314_2019350/unwrap.grd ../intf_all/2019314_2019350/corr.grd 2019314 2019350 -40.1539
../intf_all/2019314_2020009/unwrap.grd ../intf_all/2019314_2020009/corr.grd 2019314 2020009 -26.018
../intf_all/2019350_2020009/unwrap.grd ../intf_all/2019350_2020009/corr.grd 2019350 2020009 14.1358
../intf_all/2019350_2020045/unwrap.grd ../intf_all/2019350_2020045/corr.grd 2019350 2020045 34.5671
../intf_all/2020009_2020045/unwrap.grd ../intf_all/2020009_2020045/corr.grd 2020009 2020045 20.4313
../intf_all/2020009_2020081/unwrap.grd ../intf_all/2020009_2020081/corr.grd 2020009 2020081 -14.845
../intf_all/2020045_2020081/unwrap.grd ../intf_all/2020045_2020081/corr.grd 2020045 2020081 -35.2764
../intf_all/2020045_2020105/unwrap.grd ../intf_all/2020045_2020105/corr.grd 2020045 2020105 0.294368
../intf_all/2020081_2020105/unwrap.grd ../intf_all/2020081_2020105/corr.grd 2020081 2020105 35.5707
../intf_all/2020081_2020141/unwrap.grd ../intf_all/2020081_2020141/corr.grd 2020081 2020141 77.4937
../intf_all/2020081_2020165/unwrap.grd ../intf_all/2020081_2020165/corr.grd 2020081 2020165 40.8636
../intf_all/2020105_2020141/unwrap.grd ../intf_all/2020105_2020141/corr.grd 2020105 2020141 41.923
../intf_all/2020105_2020165/unwrap.grd ../intf_all/2020105_2020165/corr.grd 2020105 2020165 5.29284
../intf_all/2020141_2020165/unwrap.grd ../intf_all/2020141_2020165/corr.grd 2020141 2020165 -36.6301
../intf_all/2020141_2020201/unwrap.grd ../intf_all/2020141_2020201/corr.grd 2020141 2020201 -15.0594
../intf_all/2020165_2020201/unwrap.grd ../intf_all/2020165_2020201/corr.grd 2020165 2020201 21.5707
../intf_all/2020165_2020237/unwrap.grd ../intf_all/2020165_2020237/corr.grd 2020165 2020237 -53.8117
../intf_all/2020201_2020237/unwrap.grd ../intf_all/2020201_2020237/corr.grd 2020201 2020237 -75.3824
../intf_all/2020201_2020261/unwrap.grd ../intf_all/2020201_2020261/corr.grd 2020201 2020261 -34.6997
../intf_all/2020201_2020285/unwrap.grd ../intf_all/2020201_2020285/corr.grd 2020201 2020285 -28.2553
../intf_all/2020237_2020261/unwrap.grd ../intf_all/2020237_2020261/corr.grd 2020237 2020261 40.6827
../intf_all/2020237_2020285/unwrap.grd ../intf_all/2020237_2020285/corr.grd 2020237 2020285 47.1271
../intf_all/2020261_2020285/unwrap.grd ../intf_all/2020261_2020285/corr.grd 2020261 2020285 6.44437
../intf_all/2020261_2020333/unwrap.grd ../intf_all/2020261_2020333/corr.grd 2020261 2020333 9.65142
../intf_all/2020285_2020333/unwrap.grd ../intf_all/2020285_2020333/corr.grd 2020285 2020333 3.20705
../intf_all/2020285_2020357/unwrap.grd ../intf_all/2020285_2020357/corr.grd 2020285 2020357 69.6239
../intf_all/2020333_2020357/unwrap.grd ../intf_all/2020333_2020357/corr.grd 2020333 2020357 66.4168
../intf_all/2020333_2021027/unwrap.grd ../intf_all/2020333_2021027/corr.grd 2020333 2021027 -61.5445
../intf_all/2020333_2021051/unwrap.grd ../intf_all/2020333_2021051/corr.grd 2020333 2021051 28.9424
../intf_all/2020357_2021027/unwrap.grd ../intf_all/2020357_2021027/corr.grd 2020357 2021027 -127.961
../intf_all/2020357_2021051/unwrap.grd ../intf_all/2020357_2021051/corr.grd 2020357 2021051 -37.4744
../intf_all/2021027_2021051/unwrap.grd ../intf_all/2021027_2021051/corr.grd 2021027 2021051 90.4869

```

8. LiCSBAS SCRIPT

```
#!/bin/bash -eu
# LiCSBAS steps:
# 01: LiCSBAS01_get_geotiff.py
# 02: LiCSBAS02_ml_prep.py
# 03: LiCSBAS03op_GACOS.py (optional)
# 04: LiCSBAS04op_mask_unw.py (optional)
# 05: LiCSBAS05op_clip_unw.py (optional)
# 11: LiCSBAS11_check_unw.py
# 12: LiCSBAS12_loop_cLOSure.py
# 13: LiCSBAS13_sb_inv.py
# 14: LiCSBAS14_vel_std.py
# 15: LiCSBAS15_mask_ts.py
# 16: LiCSBAS16_filt_ts.py

#####
### Settings ###
#####
start_step="01" # 01-05, 11-16
end_step="16" # 01-05, 11-16

nlook="1" # multilook factor, used in step02
GEOCmldir="GEOCml${nlook}" # If start from 11 or
later after doing 03-05, use e.g.,
GEOCml${nlook}GACOSmaskclip
n_para="" # Number of paralell processing in step 02-
05,12,13,16. default: number of usable CPU
gpu="n" # y/n
check_only="n" # y/n. If y, not run scripts and just show
commands to be done

logdir="log"
log="$logdir/$(date +%Y%m%d%H%M)$(basename
$0 .sh)_${start_step}_${end_step}.log"

### Optional steps (03-05) ###
order_op03_05="03 04 05" # can change order e.g., 05 03
04
do03op_GACOS="n" # y/n
do04op_mask="n" # y/n
do05op_clip="y" # y/n
p04_mask_coh_thre="" # e.g. 0.2
p04_mask_range="" # e.g. 10:100/20:200 (ix start from
0)
p04_mask_range_file="" # Name of file containing range
list
p05_clip_range="" # e.g. 10:100/20:200 (ix start from 0)
p05_clip_range_geo="110.91/111.40/-8.27/-7.88" # e.g.
130.11/131.12/34.34/34.6 (in deg)

### Frequently used options. If blank, use default. ###
p01_start_date="20190420" # default: 20141001
p01_end_date="20210222" # default: today
p01_get_gacos="n" # y/n
p11_unw_thre=""
p11_coh_thre="0.1" # default: 0.05
p12_loop_thre="" # default: 1.5 rad
p12_multi_prime="y" # y/n. y recommended
p12_rm_ifg_list="" # List file containing ifgs to be
manually removed
p15_coh_thre="" # default: 0.05
p15_n_unw_r_thre="" # default: 1.5
```

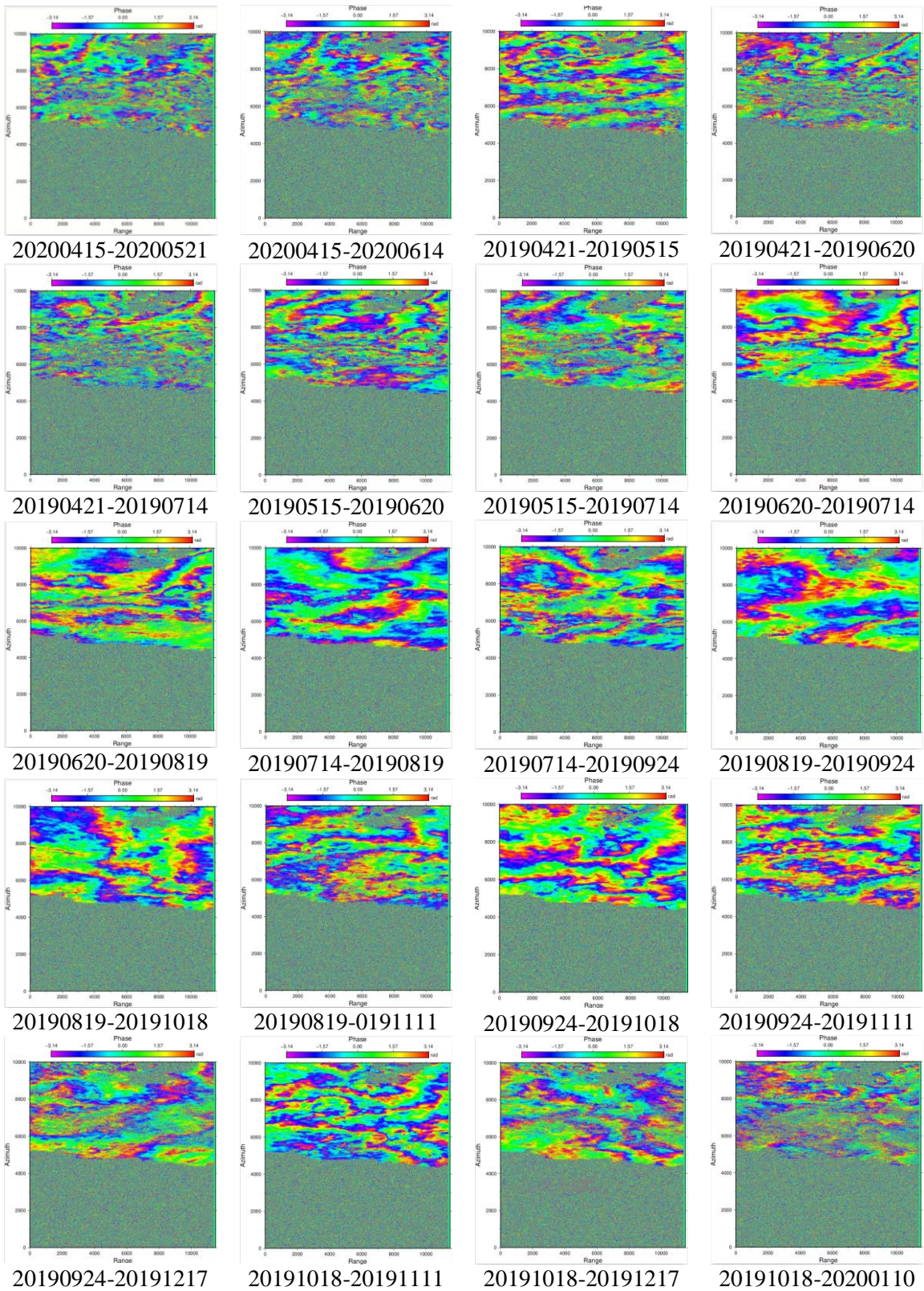
```
p15_vstd_thre="" # default: 100 mm/yr
p15_maxTlen_thre="" # default: 1 yr
p15_n_gap_thre="" # default: 10
p15_stc_thre="" # default: 5 mm
p15_n_ifg_noloop_thre="" # default: 50
p15_n_loop_err_thre="" # default: 5
p15_resid_rms_thre="" # default: 2 mm
p16_filtwidth_km="" # default: 2 km
p16_filtwidth_yr="" # default: avg_interval*3 yr
p16_deg_deramp="" # 1, bl, or 2. default: no deramp
p16_hgt_linear="n" # y/n. default: n
p16_hgt_min="" # default: 200 (m)
p16_hgt_max="" # default: 10000 (m)
p16_range="" # e.g. 10:100/20:200 (ix start from 0)
p16_range_geo="" # e.g. 130.11/131.12/34.34/34.6 (in
deg)
p16_ex_range="" # e.g. 10:100/20:200 (ix start from 0)
p16_ex_range_geo="" # e.g. 130.11/131.12/34.34/34.6
(in deg)

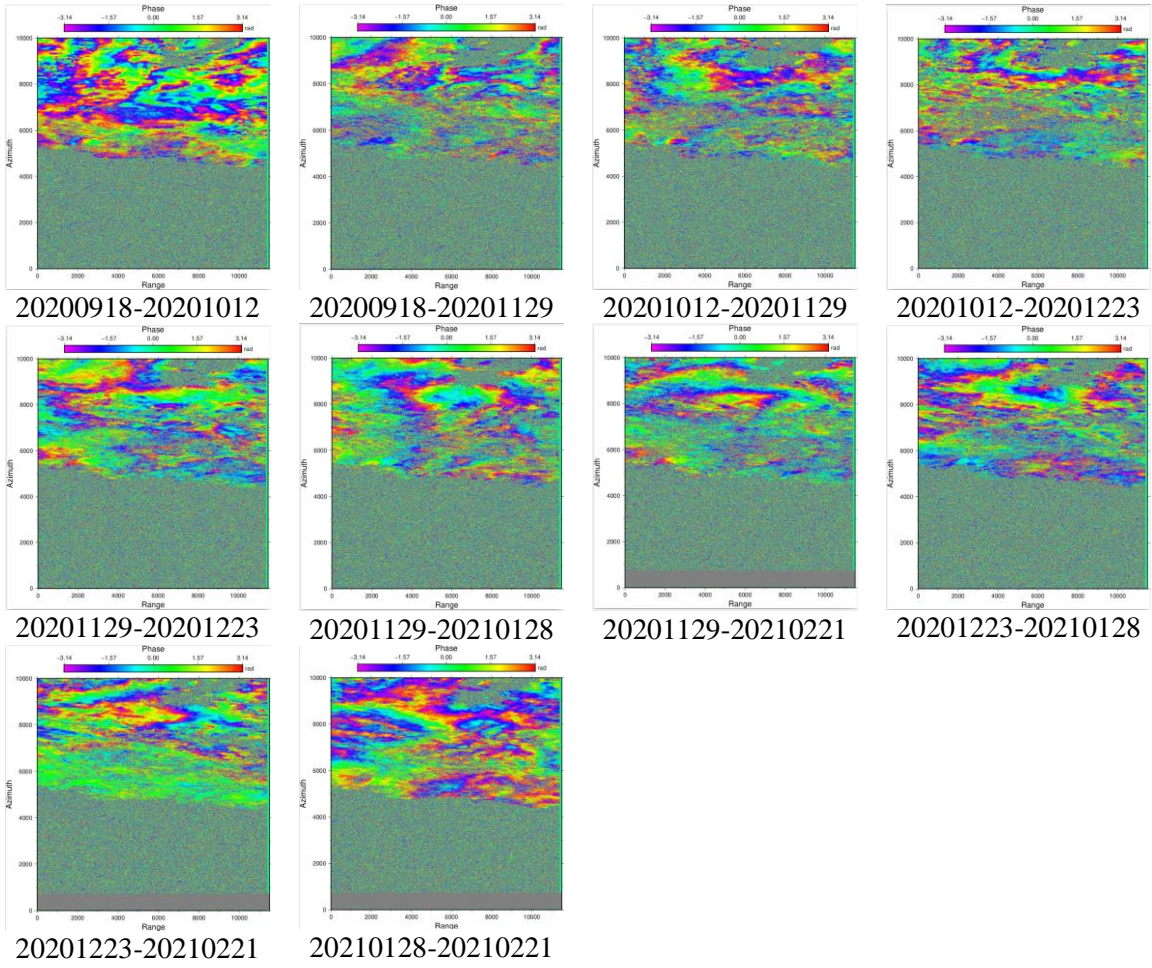
### Less frequently used options. If blank, use default. ###
p01_frame="" # e.g. 021D_04972_131213
p01_n_para="" # default: 4
p02_GEOCdir="" # default: GEOC
p02_GEOCmldir="" # default: GEOCml$nlook
p02_freq="" # default: 5.405e9 Hz
p02_n_para="" # default: # of usable CPU
p03_inGEOCmldir="" # default: $GEOCmldir
p03_outGEOCmldir_suffix="" # default: GACOS
p03_fillhole="y" # y/n. default: n
p03_gacosdir="" # default: GACOS
p03_n_para="" # default: # of usable CPU
p04_inGEOCmldir="" # default: $GEOCmldir
p04_outGEOCmldir_suffix="" # default: mask
p04_n_para="" # default: # of usable CPU
p05_inGEOCmldir="" # default: $GEOCmldir
p05_outGEOCmldir_suffix="" # default: clip
p05_n_para="" # default: # of usable CPU
p11_GEOCmldir="" # default: $GEOCmldir
p11_TSdir="" # default: TS_$GEOCmldir
p12_GEOCmldir="" # default: $GEOCmldir
p12_TSdir="" # default: TS_$GEOCmldir
p12_n_para="" # default: # of usable CPU
p13_GEOCmldir="" # default: $GEOCmldir
p13_TSdir="" # default: TS_$GEOCmldir
p13_inv_alg="" # LS (default) or WLS
p13_mem_size="" # default: 8000 (MB)
p13_gamma="" # default: 0.0001
p13_n_para="" # default: # of usable CPU
p13_n_unw_r_thre="" # default: 1
p13_keep_incfile="n" # y/n. default: n
p14_TSdir="" # default: TS_$GEOCmldir
p14_mem_size="" # default: 4000 (MB)
p15_TSdir="" # default: TS_$GEOCmldir
p15_vmin="" # default: auto (mm/yr)
p15_vmax="" # default: auto (mm/yr)
p15_keep_isolated="n" # y/n. default: n
p15_noautoadjust="n" # y/n. default: n
p16_TSdir="" # default: TS_$GEOCmldir
p16_nomask="n" # y/n. default: n
p16_n_para="" # default: # of usable CPU
```

9. LAYOUTING SCRIPT

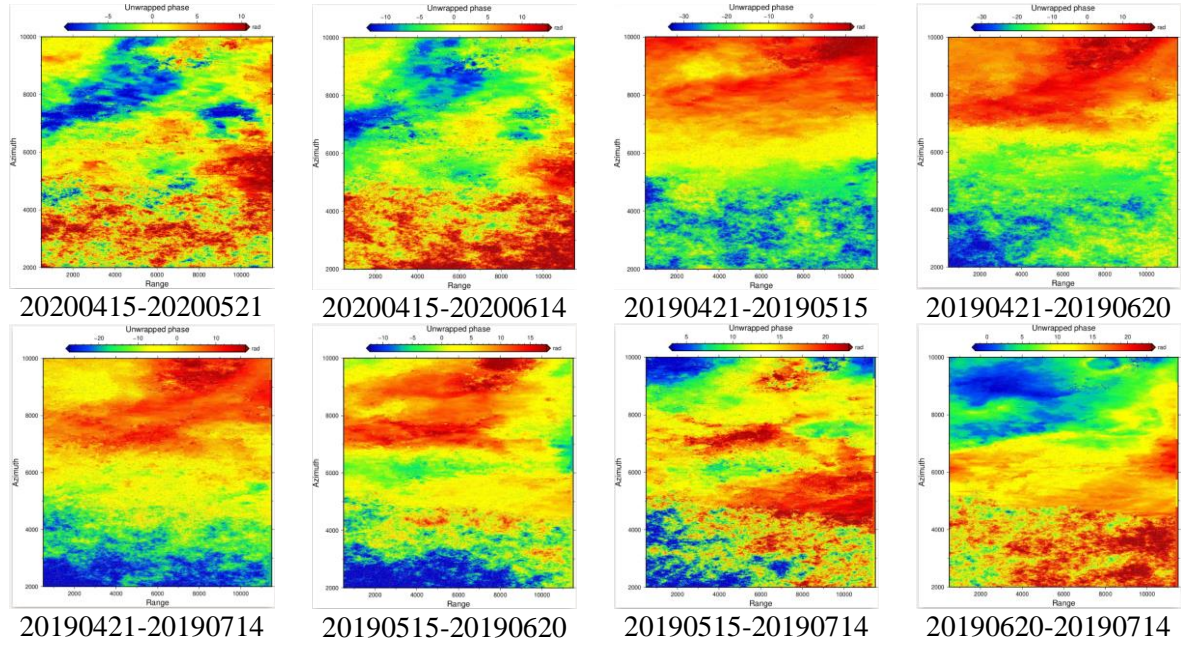
```
#!/bin/bash
# Set GMT parameters
gmt set MAP_FRAME_TYPE plain FONT_ANNOT_PRIMARY 10p
# Create PostScript file
gmt pscoast -JM15 -R111.02/111.43/-8.3/-7.9 -Ba0.05g0.2f0.5:."GMTSAR":WSne -Ggrey -Slightblue -Dh
-N1 -W1 -P -K > sbas.ps
# Plot LOS value
awk '{ print $1, $2, $3, $4*0.1 }' vel_ll_fix.xyz | gmt psxy -JM -R -Sc0.03 -Cvel_ll.cpt -O -K >> sbas.ps
#grdimage pacitan_ref.nc -R -JM -O -Ba2g2wsne -K >> sbas.ps
gmt pscoast -JM15 -R -Lf111.06/-7.99/10/8+l+jr -T111.05/-7.95/0.75i/2 -Slightblue -Dh -N1 -W1 -P -O -K
>> sbas.ps
# Add shapefile
gmt psxy Pacitan.gmt -R111.02/111.43/-8.3/-7.9 -JM -W0.5p -O -K >> sbas.ps
gmt psxy Grindulu.gmt -R111.02/111.43/-8.3/-7.9 -JM -Wred -W0.5p -O -K >> sbas.ps
# Add color scale
gmt psscale -Cvel_ll.cpt -DJRM+o0.6i/0+e+mc -R -J -Bx25+lGEOID -By+imm -O -K >> sbas.ps
# Add more points with labels as needed and Add text label for the region
gmt pstext -R -J -F+f10p,Helvetica+jTL -O -K << EOF >> sbas.ps
111.048 -8.122 A1
111.113904085 -8.23284795617 A2
111.155 -8.062 B1
111.219 -8.169 B2
111.258 -8.011 C1
111.322 -8.119 C2
EOF
# Generate point cross-profiles
gmt psxy -R -J -O -K -Sc0.2 -Gblue << EOF >> sbas.ps
111.044 -8.122 1
111.114 -8.233 1
111.151 -8.062 1
111.219 -8.169 1
111.254 -8.011 1
111.322 -8.119 1
EOF
# Generate cross-profiles
gmt psxy -R -J -O -K -W0.5p << EOF >> sbas.ps
111.044 -8.122 A1
111.114 -8.233 A2
EOF
gmt psxy -R -J -O -K -W0.5p << EOF >> sbas.ps
111.151 -8.062 B1
111.219 -8.169 B2
EOF
gmt psxy -R -J -O -K -W0.5p << EOF >> sbas.ps
111.254 -8.011 C1
111.322 -8.119 C2
EOF
# Finalize the PostScript
gmt psxy -R -JM -O -T >> sbas.ps
# Convert PostScript to JPEG
gmt psconvert sbas.ps -Tj -A+p -P -Fpetavel
# Display a success message
echo "Plotting completed successfully."
```

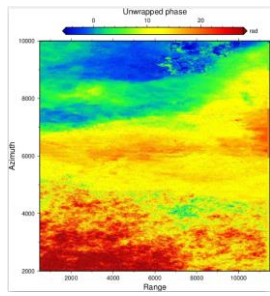
10. RESULT PHASE FILTER



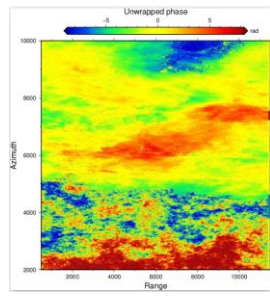


11. RESULT PHASE UNWRAPPING

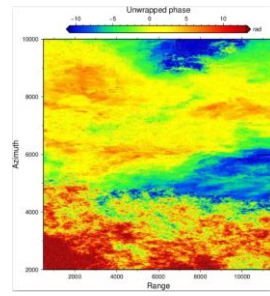




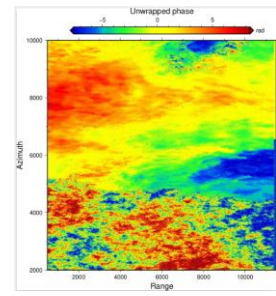
20190620-20190819



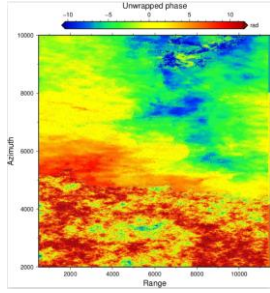
20190714-20190819



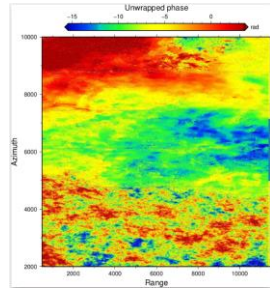
20190714-20190924



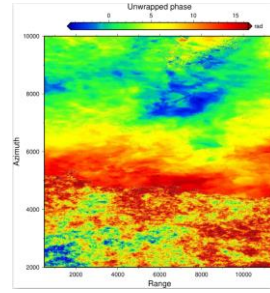
20190819-20190924



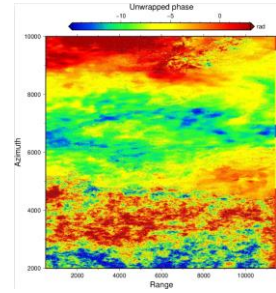
20190819-20191018



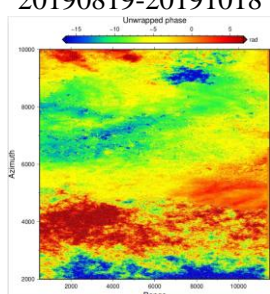
20190819-0191111



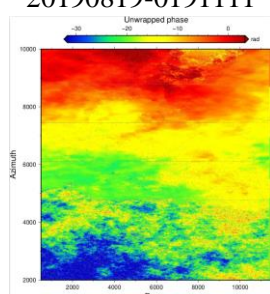
20190924-20191018



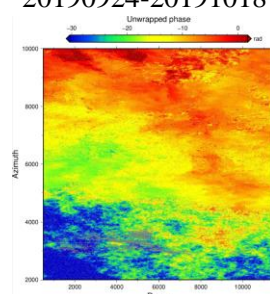
20190924-20191111



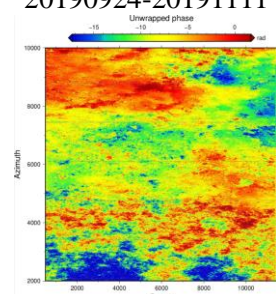
20190924-20191217



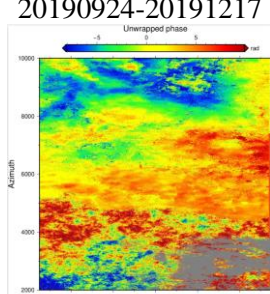
20191018-20191111



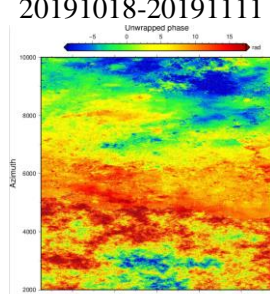
20191018-20191217



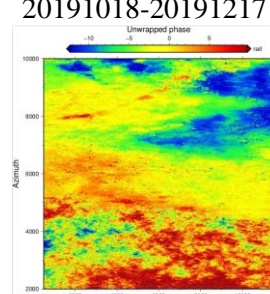
20191018-20200110



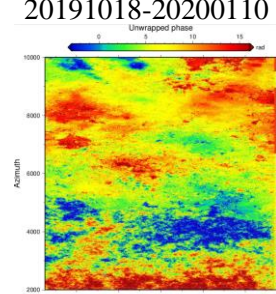
20191111-20191217



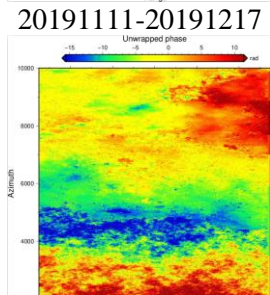
20191111-20200110



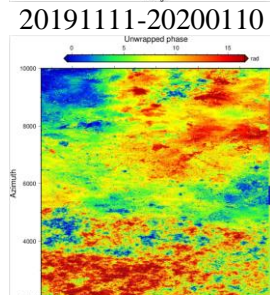
20191217-20200110



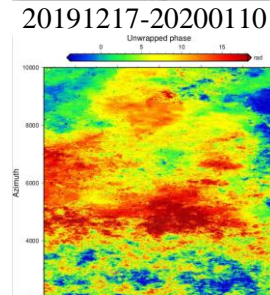
20191217-20200215



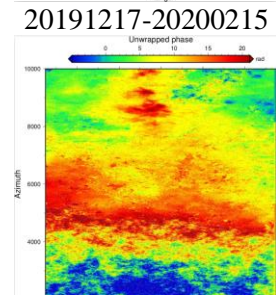
20200110-20200215



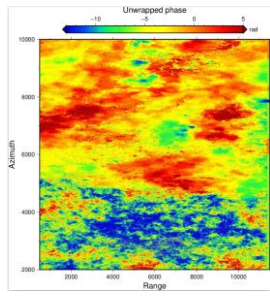
20200110-20200322



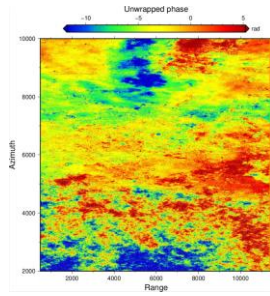
20200215-20200415



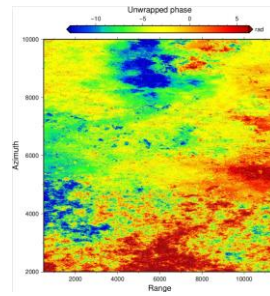
20200215-20200322



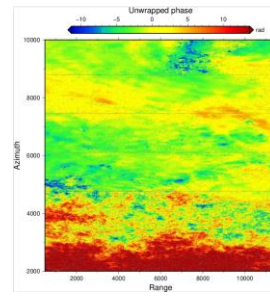
20200322-20200415



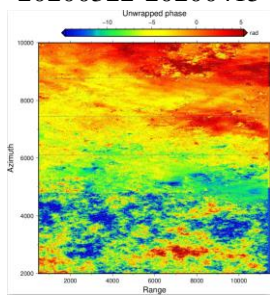
20200322-20200521



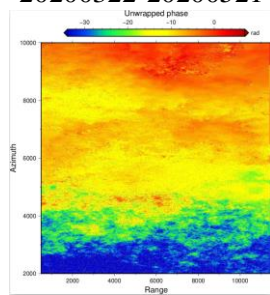
20200322-20200614



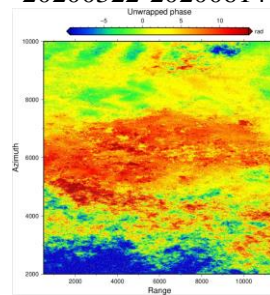
20200521-20200614



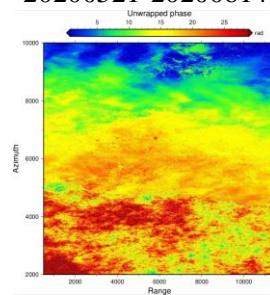
20200521-20200720



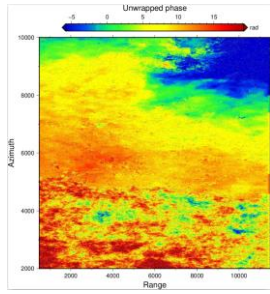
20200614-20200720



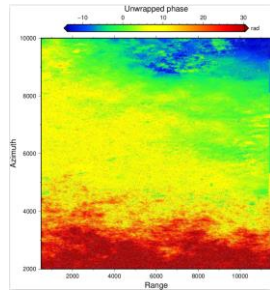
20200614-20200825



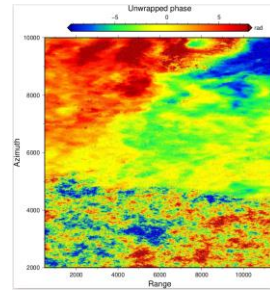
20200720-20200825



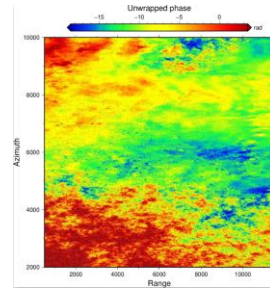
20200720-20200918



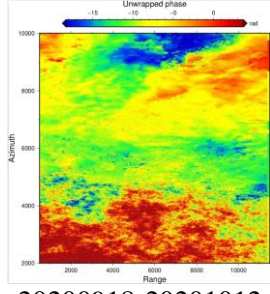
20200720-20201012



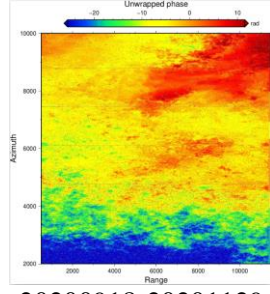
20200825-20200918



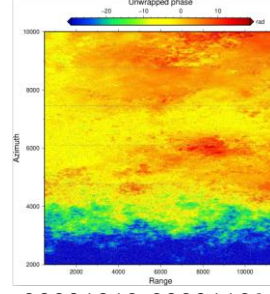
20200825-20201012



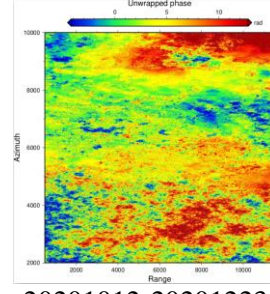
20200918-20201012



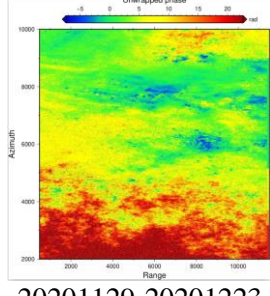
20200918-20201129



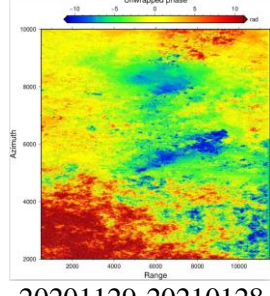
20201012-20201129



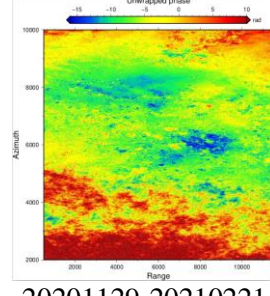
20201012-20201223



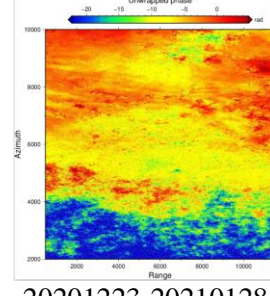
20201129-20201223



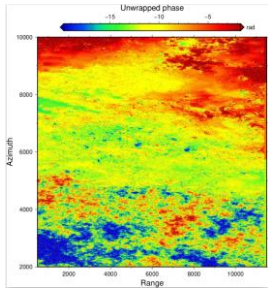
20201129-20210128



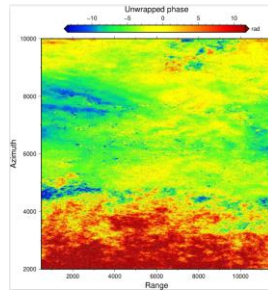
20201129-20210221



20201223-20210128

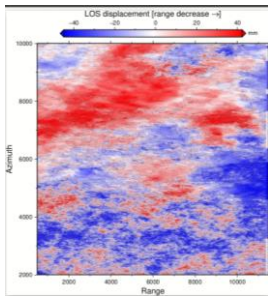


20210123-20210221

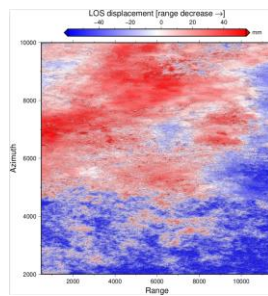


20210128-20210221

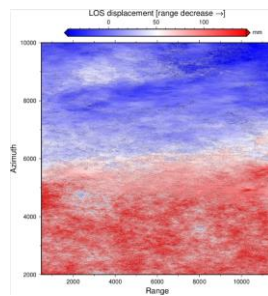
12. RESULT LOS DISPLACEMENT



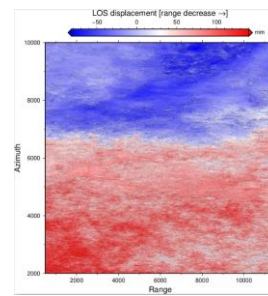
20200415-20200521



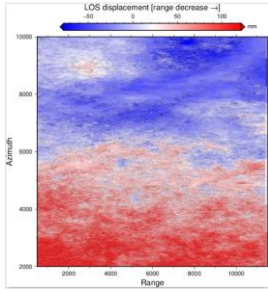
20200415-20200614



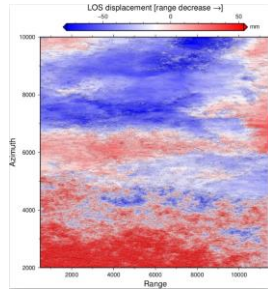
20190421-20190515



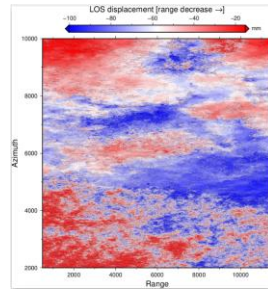
20190421-20190620



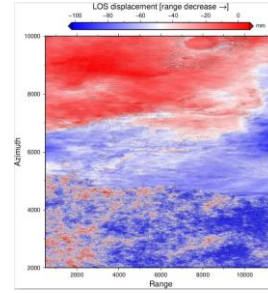
20190421-20190714



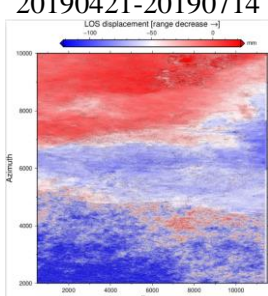
20190515-20190620



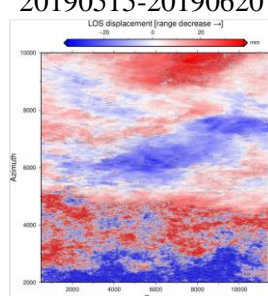
20190515-20190714



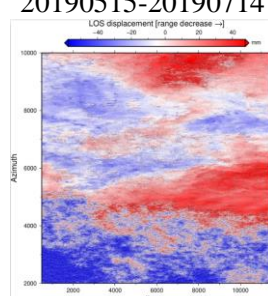
20190620-20190714



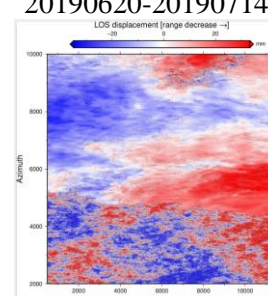
20190620-20190819



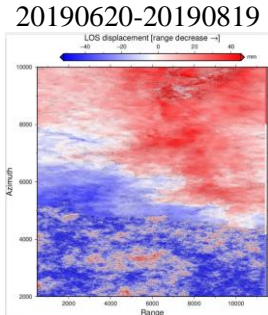
20190714-20190819



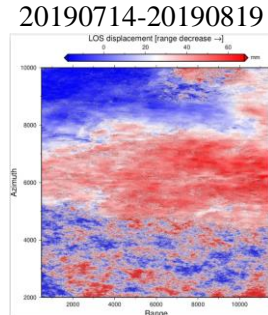
20190714-20190924



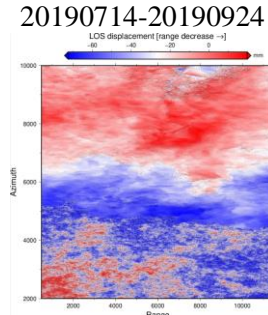
20190819-20190924



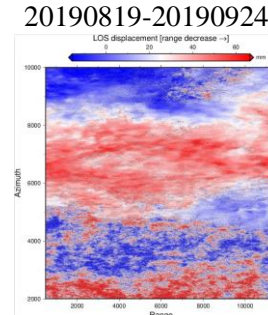
20190819-20191018



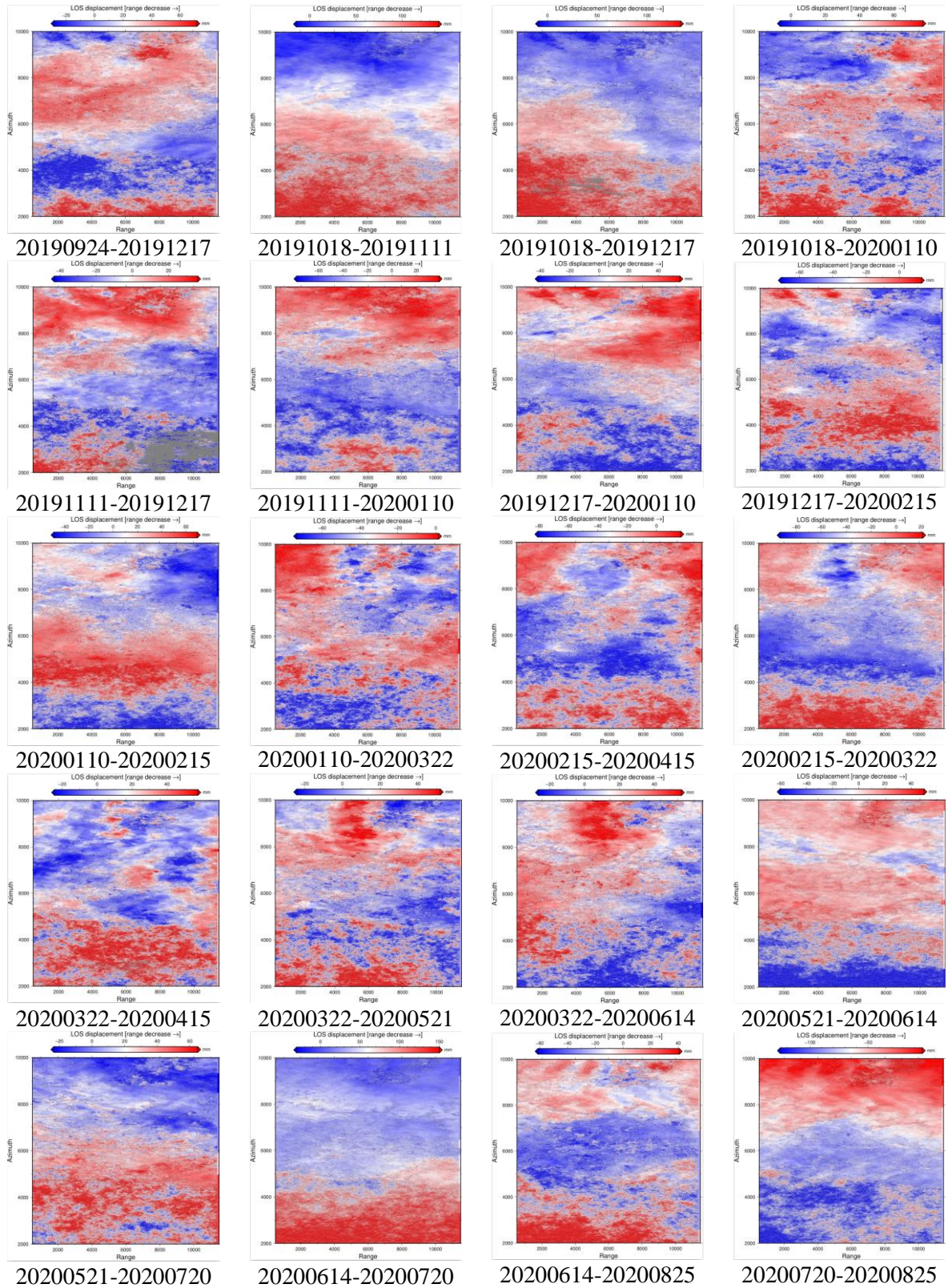
20190819-0191111

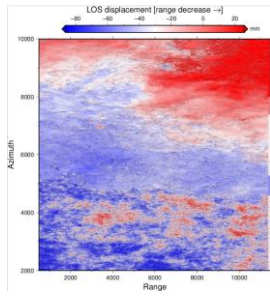


20190924-20191018

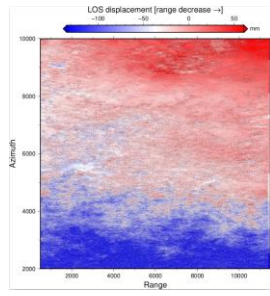


20190924-20191111

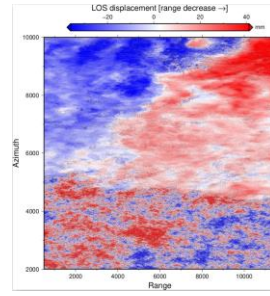




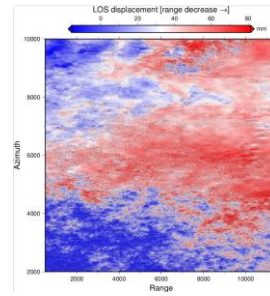
20200720-20200918



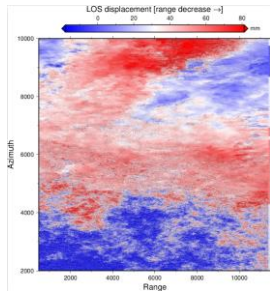
20200720-20201012



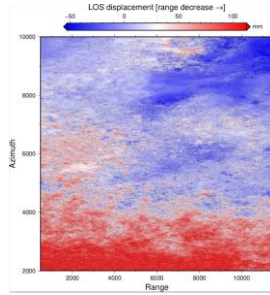
20200825-20200918



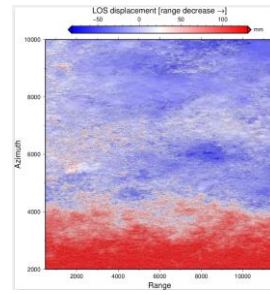
20200825-20201012



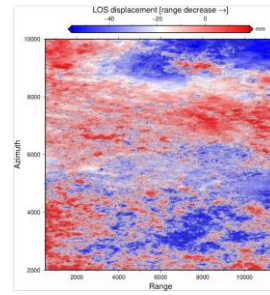
20200918-20201012



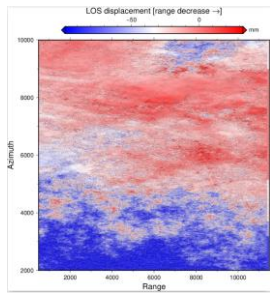
20200918-20201129



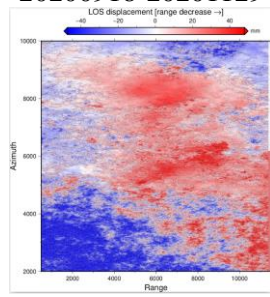
20201012-20201129



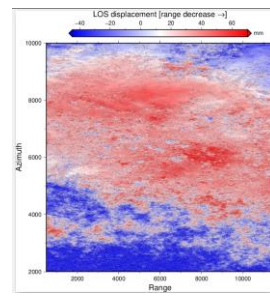
20201012-20201223



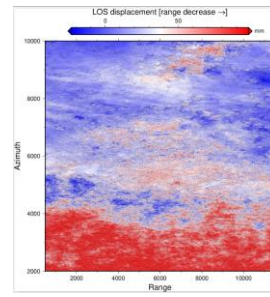
20201129-20201223



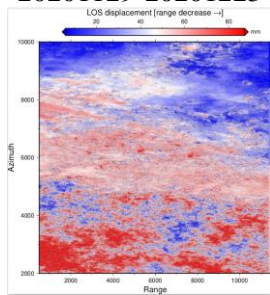
20201129-20210128



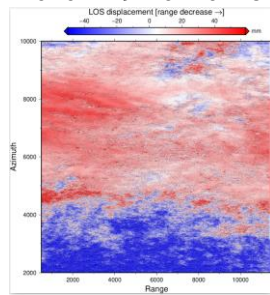
20201129-20210221



20201223-20210128

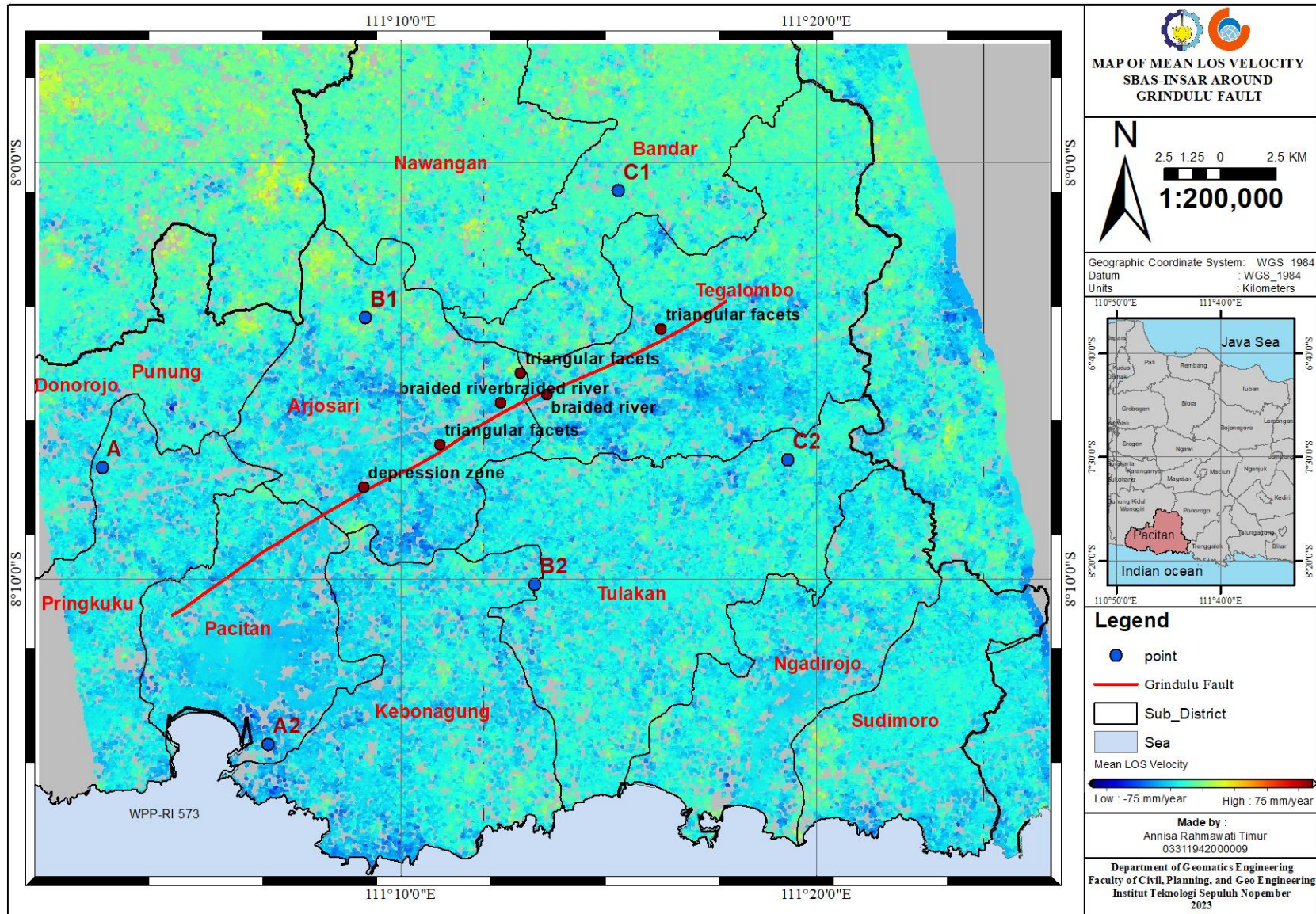


20201223-20210221



20210128-20210221

13. RESULT MEAN LOS DISPLACEMENT VELOCITY MAP



"This page was deliberately blanked."

AUTHOR'S BIOGRAPHY



The author was born in Nganjuk on September 18, 2000, and is the youngest of two siblings. The author has pursued formal education at Baitul Izzah Islamic Elementary School in Nganjuk, Baitul Izzah Islamic Junior High School in Malang, and MAN 3 Yogyakarta (an Islamic public high school). After graduating from MAN 3 Yogyakarta in 2019, the author was accepted into the Geomatics Engineering Department of FTSPK-ITS (Sepuluh Nopember Institute of Technology) in 2019 through the International Undergraduate Program (IUP) and registered with student ID 03311942000009.

The author has been actively involved in several organizational activities. They served as the Staff of the Professionalism and Competency Department in the Geomatics Student Association of ITS (HIMAGE-ITS) during their term. They also held the position of Treasurer in the Bridge Student Activity Unit of Sepuluh Nopember Institute of Technology (UKM BRIDGE-ITS), as well as being involved in treasurer roles in the Student Executive Faculty of Civil, Planning and Geo Engineering (BEM FTSPK ITS). The author actively participated in competitions in the field of Geomatics Engineering at both national and international levels and achieved a gold medal as part of a team in the Youth International Science Fair (YISF) Engineering Category at the international level. They also actively participated in student management training such as LKMM PRA-TD, as well as attending seminars at the institute, regional, national, and international levels organized by institutions or agencies related to Geodesy and Geomatics. In addition to that, the author actively engaged in voluntary activities, particularly in the humanitarian project "UMKM Development Using Marketing Technology, Networks and Business Processes for Porang Products" organized by the Sepuluh Nopember Institute of Technology in Nganjuk Regency in 2021. During the undergraduate studies in Geomatics Engineering, the author completed an internship at government institutions, Office of ATR/National Land Agency Surakarta City in 2020 and Pertamina Geothermal Energy in Garut. Author also participated in internationalization activities, such as a one-year student exchange program at Universiti Teknologi MARA (UiTM) Shah Alam, Malaysia. For their final research project, the author chose the field of Deformation with the title "Application Of Small Baseline Subset (SBAS)-InSAR Technique To Study Surface Deformation Due To The Grindulu Fault Activities Using Sentinel-1 Data" as a requirement for completing their undergraduate studies.